Optische Detektion von Rydbergpopulationen und Kohärenzen

Dissertation

der Mathematisch-Naturwissenschaftlichen Fakultät
der Eberhard Karls Universität Tübingen
zur Erlangung des Grades eines
Doktors der Naturwissenschaften
(Dr. rer. nat.)

vorgelegt von
Florian Karlewski
aus Mainz

Tübingen
2015

Gedruckt mit Genehmigung der Mathematisch-Naturwissenschaftlichen Fakultät der Eberhard Karls Universität Tübingen.

Tag der mündlichen Qualifikation:	19.06.2015
Dekan:	Prof. Dr. Wolfgang Rosenstiel
1. Berichterstatter:	Prof. Dr. József Fortágh
2. Berichterstatter:	Prof. Dr. Nils Schopohl

Inhaltsverzeichnis

Resümees

Zusammenfassung

Diese Arbeit präsentiert eine neue Technik zur optischen Detektion der Besetzungen von Rydbergzuständen, welche auf der zeitaufgelösten Messung der elektromagnetisch induzierten Transparenz beruht, und demonstriert diese experimentell. Sie erlaubt nicht nur die Messung von Rydbergpopulationen in atomaren Ensembles, sondern prinzipiell auch die Bestimmung der Kohärenzen zwischen Grund- und Rydbergzuständen. Im Gegensatz zu bisherigen Techniken, basierend auf selektiver Feldionisation, ermöglicht unser optisches Messschema den gleichzeitigen Nachweis von Besetzungen und Kohärenzen ohne das atomare Ensemble dabei zu zerstören. Damit öffnen sich neue Möglichkeiten im Bereich der kohärenten Manipulation und Detektion von Quantensystemen basierend auf Rydbergatomen. In unserem Experiment haben wir den Anteil der Atome im $|35S_{1/2}\rangle$-Zustand im Bereich von bis zu 50 % eines ultrakalten Ensembles von ^{87}Rb-Atomen mit einer Genauigkeit von ± 1 % gemessen.

Da für die präzise optische Präparation, Manipulation und Detektion von Rydbergzuständen die elektronische Struktur ausschlaggebend ist, wurde diese im Rahmen der Arbeit im Detail untersucht. Insbesondere wurden die Übergangsfrequenzen von ^{87}Rb durch optische Spektroskopie basierend auf elektromagnetisch induzierter Transparenz mit einer Präzision von ± 1 MHz gemessen und damit der Quantendefekt berechnet. Mit den verbesserten Daten zum Quantendefekt bestimmten wir die Ionisationsenergie von Rubidium um zwei Größenordnungen genauer als zuvor. Diese experimentellen Ergebnisse gaben Anlass für die Entwicklung eines optimierten theoretischen Modells für das Potential des Ionenrumpfs von ^{87}Rb. Es beschreibt die Feinstrukturaufspaltung von P- und D-Rydbergzuständen von ^{87}Rb mit einer Hauptquantenzahl $n > 30$ mit einer Genauigkeit von <10 MHz, zwei Größenordnung besser als bisherige Modelle.

Der Einfluss von elektrischen Feldern auf Rydbergzustände ist ebenfalls wichtig für das Verständnis von Ergebnissen unter realistischen experimentellen Bedingungen. Deswegen wurde die Stark-Aufspaltung von Rydbergzuständen in einem elektrischen Feldbereich von bis zu 500 V/cm mit einer Präzision von bis zu 2 MHz gemessen, wodurch einschlägige Theorien bis weit über die klassische Ionisationsgrenze hinaus verifiziert werden konnten. Eine Anwendung der Rydbergspektroskopie zur Charakterisierung von inhomogenen elektrischen Feldverteilungen in der Nähe von Oberflächen in Abständen zwischen 30 µm und 300 µm wurde demonstriert.

Abstract

This thesis introduces a novel technique for the all-optical detection of Rydberg atoms in ensembles of cold atoms. We show that time-resolved measurements of electromagnetically induced transparency can simultaneously provide information about both the population of atoms in a given Rydberg state, as well as the coherence between ground and Rydberg states. In contrast to existing techniques based on selective field ionisation our measurement scheme is non-destructive, thus opening up new possibilities in the field of coherent manipulation and detection of quantum systems based on Rydberg atoms. In our experiment we measured the fraction atoms excited to the $|35S_{1/2}\rangle$ state in an ultracold ensemble of ^{87}Rb atoms with an accuracy of $\pm 1\,\%$.

Precise knowledge of the electronic structure of the atom under investigation is crucial for the optical preparation, manipulation and detection of Rydberg atoms. We therefore measured the transition frequencies of Rydberg atoms of ^{87}Rb by means of spectroscopy based on electromagnetically induced transparency with an accuracy of $\pm 1\,\mathrm{MHz}$ and calculated the quantum defect. Improving the value of the quantum defect has lead to a two orders of magnitude increase in the accuracy of the knowledge of the ionisation energy of rubidium. These experimental results encouraged the development of an optimized theoretical model for the potential of the atomic core of ^{87}Rb. It describes the fine stucture splitting in P and D Rydberg states of ^{87}Rb with a principal quantum number $n > 30$ with an accuracy of $<10\,\mathrm{MHz}$, thus two orders of magnitude better than previous models.

Understanding the influence of electric fields on Rybderg states is critical to interpreting results under realistic experimental conditions. We have therefore measured the Stark splitting of Rydberg atoms in electric field strengths up to $500\,\mathrm{V/cm}$ at an accuracy of up to $2\,\mathrm{MHz}$. These measurements were used to verify established theories far beyond the ionisation threshold. An application of the Rydberg spectroscopy based on electromagnetically induced transparency has been demonstrated in characterising an inhomogeneous electric field in the vicinity of a surface with distances between $30\,\mu\mathrm{m}$ and $300\,\mu\mathrm{m}$.

Liste der Veröffentlichungen

Diese Dissertation ist kumulativ und basiert auf den nachfolgend in chronologischer Reihenfolge aufgeführten Veröffentlichungen. In Anhang A befinden sich die Publikationen in voller Länge.

Veröffentlichte Manuskripte

Publikation [1]

Measurement of absolute transition frequencies of ^{87}Rb *to nS and nD Rydberg states by means of electromagnetically induced transparency*
M. Mack, **F. Karlewski**, H. Hattermann, S. Höckh, F. Jessen, D. Cano, and J. Fortágh
Physical Review A **83**, 052515 (2011).

Publikation [2]

Detrimental adsorbate fields in experiments with cold Rydberg gases near surfaces
H. Hattermann, M. Mack, **F. Karlewski**, F. Jessen, D. Cano, and J. Fortágh
Physical Review A **86**, 022511 (2012).

Publikation [3]

Quasiclassical quantum defect theory and the spectrum of highly excited rubidium atoms
A. Sanayei, and N. Schopohl,
J.Grimmel, M. Mack, **F. Karlewski**, and J. Fortágh
Physical Review A **91**, 032509 (2015).

Publikation [4]

Measurement and numerical calculation of Rubidium Rydberg Stark spectra
J. Grimmel, M. Mack, **F. Karlewski**, F. Jessen, M. Reinschmidt, N. Sándor, and J. Fortágh
New Journal of Physics **17**, 053005 (2015).

Publikation [5]

State-selective all-optical detection of Rydberg atoms
F. Karlewski, M. Mack, J. Grimmel, N. Sándor, and J. Fortágh
Physical Review A **91**, 043422 (2015).

Eigenanteil

Publikation [1]

Ich beteiligte mich an der Entwicklung des Konzepts und dem Aufbau des Experiments. Dazu gehörte die Einrichtung eines neuen Labors inklusive eines Frequenzkamms und die Stabilisierung der Laserfrequenzen mit diesem Frequenzkamm und einem Fizeau-basierten Wellenlängenmessgerät. Außerdem trug ich zur Erfassung, zur Analyse und zur Interpretation der Daten bei.

Publikation [2]

Ich beteiligte mich an der Entwicklung des Konzepts und dem Aufbau des Experiments. Insbesondere die Anwendung der in Publikation [1] verwendeten Stabilisierung der Laserfrequenzen mit einem Frequenzkamm und einem Fizeau-basierten Wellenlängenmessgerät in einem anderen Labor lag in meiner Verantwortung. Außerdem trug ich zur Erfassung, zur Analyse und zur Interpretation der Daten bei.

Publikation [3]

Ich beteiligte mich an den Diskussionen während der Entwicklung der Idee und bei der Erstellung des Manuskripts durch die Zusammenstellung von experimentellen Daten für den Vergleich mit den Ergebnissen der theoretischen Berechnungen.

Publikation [4]

Ich beteiligte mich an der Entwicklung des Konzepts, dem Aufbau des Experiments und der Analyse und Interpretation der Daten.

Publikation [5]

Für diese Veröffentlichung übernahm ich in allen Bereichen die Hauptverantwortung und Federführung. Dies umfasste unter anderem die Entwicklung des Konzepts, den Aufbau des Experiments, die Datenerfassung, die Entwicklung des theoretischen Modells, die Analyse und Interpretation der Daten und das Erstellen des Manuskripts. Ich beteiligte mich maßgeblich bei dem Aufbau eines neuen Labors mit einer Apparatur zur Erzeugung ultrakalter Gase aus Rubidiumatomen für diese Veröffentlichung.

1 Einleitung

1.1 Quantensimulation mit Rydbergatomen

Seit mehreren Jahrzehnten ist die Simulation quantenmechanischer Prozesse mit kontrollierten quantenmechanischen Systemen, die Quantensimulation, ein wichtiges Forschungsgebiet der Physik [6]. Mit ihr sollen Problemstellungen gelöst werden, die auf klassischen Computern nicht in endlicher Zeit lösbar sind, wie beispielsweise die Simulation quantenmechanischer Vielteilchensysteme. Die experimentellen und theoretischen Arbeiten befassen sich unter anderem mit Ionen [7], Quantenpunkten in Halbleitern [8], supraleitenden Schaltkreisen [9], Kernspins [10] und linearer Optik [11], sowie mit hochangeregten Atomen, sogenannten Rydbergatomen [12]. Als vielversprechend gelten auch hybride Ansätze, die diese Teilsysteme wie zum Beispiel supraleitende Schaltkreise, Atome und Photonen miteinander kombinieren, um eine schnelle Bearbeitung, lange Speicherung und effiziente Übertragung von Quanteninformationen zu erreichen [13, 14]. In supraleitenden Schaltkreisen können schnelle und zuverlässige Quantengatter realisiert werden [9]. Allerdings liegt die maximale Kohärenzzeit, also die mögliche Speicherzeit eines quantenmechanischen Zustands, des Qubits, aktuell nur im Mikrosekunden-Bereich. Die Kohärenz wird durch Effekte wie die thermische Ankopplung an die Umwelt, selbst in einer Millikelvin-Umgebung, die Kopplung an Auslesegeräte oder elektromagnetische Strahlung die Kohärenz zerstört. Ultrakalte Atome im Vakuum in konservativen Fallenpotentialen hingegen sind thermisch gut isoliert und können sogar in Abständen von wenigen Mikrometern zur Oberfläche Kohärenzzeiten von mehreren Sekunden erreichen [15]. Daher eignen sie sich sehr gut als Quantenspeicher. Gleichzeitig macht ihre gute Isolation eine starke Kopplung an Festkörpersysteme schwierig, was zur Übertragung der Quanteninformation aber notwendig ist. Als Schnittstelle wurden Mikrowellenresonatoren vorgeschlagen, die supraleitende Festkörper-Qubits stark an Rydbergatome koppeln [13, 14]. Dabei werden die große Polarisierbarkeit der Rydbergatome, die mit der Hauptquantenzahl zu n^7 skaliert [16], sowie kollektive Effekte durch die Rydbergblockade ausgenutzt [17, 18]. Für die Übertragung der Kohärenz in Grundzustandsatome als Quantenspeicher oder auf weit entfernte Quantensysteme sind optische Methoden notwendig. An diesen Punkt knüpft die vorliegende Arbeit an, indem sie neue Erkenntnisse über die Struktur von Rydbergatomen liefert, sowie neue optische Techniken zur Detektion von Besetzungen und Kohärenzen von Rydbergatomen präsentiert.

1.2 Elektronische Struktur von Rydbergatomen

Die Energieniveaus hochangeregter Atome, sogenannter Rydbergatome, lassen sich für Wasserstoff analytisch berechnen, da der Atomrumpf nur aus einer positiven Ladung, dem Proton, besteht. Für Alkalimetalle ist diese Rechnung aufgrund der komplizierten Rumpfstruktur aus Elektronen und dem Atomkern nicht möglich und die Energieniveaus müssen gemessen werden. Dabei zeigt sich, dass für hohe Hauptquantenzahlen n ein wasserstoffähnliches Verhalten zu beobachten ist. Die Abweichung der Energieniveaus von denjenigen des Wasserstoffs wird durch den Quantendefekt $\Delta_{l,j}$ beschrieben und die Energieniveaus der Alkalimetalle in atomaren Einheiten im Verhältnis zur Ionisationsgrenze ergeben sich aus

$$E_{n,l} = -\frac{1}{(n - \Delta_{l,j})^2} \tag{1.1}$$

mit dem Bahndrehimpuls l und dem Gesamtdrehimpuls j [16]. Um die Ionisationsenergie des Grundzustands zu bestimmen, muss zusätzlich die Übergangsfrequenz zwischen dem Grund- und einem Rydbergzustand bekannt sein. Im Rahmen dieser Arbeit wurde vor allem mit Rubidium gearbeitet. Für die zwei häufigsten Isotope mit den Massenzahlen $m_1 = 85$ und $m_2 = 87$ ist der Unterschied der Quantendefekte nicht messbar, der Unterschied der Ionisationsenergien der jeweiligen Grundzustände ist jedoch signifikant. Dies wird als Isotopieverschiebung bezeichnet.

Der Quantendefekt $\Delta_{l,j}$ wird durch die Wechselwirkung zwischen dem Valenzelektron und dem Potential des Atomrumpfs verursacht. Die genaue Kenntnis dieses Potentials ist für die Modellierung von Rydbergzuständen ausschlaggebend, da sich hieraus die Wellenfunktionen für das Valenzelektron berechnen lassen, die für numerische Simulationen grundlegend sind. Zur Beschreibung des Systems eignet sich der Breit-Pauli-Hamilton-Operator [19]

$$\hat{\mathcal{H}}_{BP} = \hat{\mathcal{H}}_{NR} + \hat{\mathcal{H}}_{RS} + \hat{\mathcal{H}}_{FS}, \tag{1.2}$$

mit dem nicht-relativistischen Hamilton-Operator $\hat{\mathcal{H}}_{NR}$, dem Hamilton-Operator für relativistische Verschiebungen $\hat{\mathcal{H}}_{RS}$ und dem Hamilton-Operator der Feinstruktur $\hat{\mathcal{H}}_{FS}$. Er ist dabei bis zur quadratischen Ordnung der Feinstrukturkonstante α^2 genau. $\hat{\mathcal{H}}_{RS}$ kommutiert mit dem Bahndrehimpuls-Operator $\hat{L}$ und dem Spin-Operator $\hat{S}$, $\hat{\mathcal{H}}_{FS}$ nur mit dem Gesamtdrehimpuls-Operator $\hat{J} = \hat{L} + \hat{S}$. $\hat{\mathcal{H}}_{RS}$ und $\hat{\mathcal{H}}_{FS}$ enthalten relativistische Korrekturterme zu $\hat{\mathcal{H}}_{NR}$. $\hat{\mathcal{H}}_{BP}$ kann zwar für Rubidium aufgestellt werden, allerdings lässt sich die zugehörige Breit-Gleichung aufgrund der Wechselwirkungen der 37 Elektronen nicht lösen. Um Energiewerte und Wellenfunktionen berechnen zu können, wird deswegen ein effektives Einelektronenpotential angenommen, das die relativistischen Effekte für den radialen Anteil der Gleichung annähert. Ein solches Potential wurde von Marinescu u. a. [20] 1994 vorgeschlagen und parametrisch an Messungen der Energieniveaus angepasst. Pawlak u. a. [21] berechneten mit diesem Potential die Energieniveaus mit großer Genauigkeit, allerdings

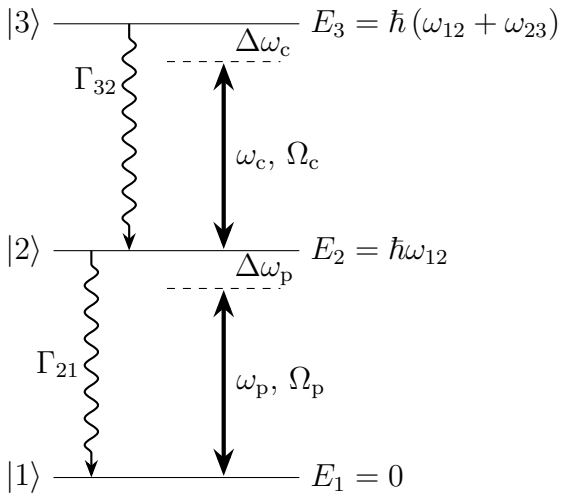

Abbildung 1.1: EIT im Drei-Niveau-System
Die drei Energieniveaus $|1\rangle$, $|2\rangle$ und $|3\rangle$ mit den atomare Übergangsfrequenzen ω_{21} und ω_{32} zerfallen mit den spontanen Zerfallsraten Γ_{21} und Γ_{32}. Die Laser mit den Frequenzen ω_p bzw. ω_c haben, auf den jeweiligen Übergang bezogen, eine Rabi-Frequenz von Ω_p bzw. Ω_c. $\Delta\omega_p = \omega_{21} - \omega_p$ und $\Delta\omega_c = \omega_{32} - \omega_c$ bezeichnen die Verstimmung des jeweiligen Lasers von der atomaren Resonanz.

zeigten sich deutliche Abweichungen gegenüber neueren Messungen, insbesondere auch bei Betrachtung der Feinstrukturaufspaltung. Dieses Problem wurde im Zusammenhang mit der Analyse unserer Messdaten erkannt [1] und von Prof. Dr. Schopohl wurde dazu eine theoretische Lösung erarbeitet [3].

1.3 Spektroskopie an Rydbergatomen

Für die Spektroskopie an Rydbergatomen hat sich eine Methode auf Grundlage der elektromagnetisch induzierten Transparenz (EIT) im stationären Fall etabliert [22, 23]. Sie eignet sich besonders für die präzise Messung der atomaren Energieniveaus von Rydbergatomen. Das für die EIT-Spektroskopie zugrundeliegende Drei-Niveau-System ist in Abbildung 1.1 dargestellt. Ein Laser testet dabei den Übergang zwischen $|1\rangle \rightarrow |2\rangle$, für ^{87}Rb entspricht dies beispielsweise $|5S_{1/2}\rangle \rightarrow |5P_{3/2}\rangle$ mit einer Wellenlänge von ≈780,24 nm und einer möglichst kleinen Intensität. Ein weiterer Laser koppelt die atomaren Zustände $|2\rangle \rightarrow |3\rangle$, in unserem Fall $|5P_{3/2}\rangle$ und $|nS_{1/2}\rangle$, $|nD_{3/2}\rangle$ oder $|nD_{5/2}\rangle$ mit einer Wellenlänge von ≈480 nm und möglichst starker Intensität. Die Rabifrequenz des Kopplungslasers Ω_c muss dabei deutlich größer als die Rabifrequenz des Testlasers Ω_p sein, damit sich eine hohe Transparenz ergibt. Durch die geringe Intensität des Testlasers werden der Zustand $|2\rangle$ und der Rydbergzustand $|3\rangle$ quasi nicht besetzt. Falls es doch eine Besetzung der Zustände gibt, zerfällt sie mit den Raten Γ_{32} und Γ_{21}. Mit der Wellenlänge des Kopplungslasers kann die Hauptquantenzahl n des adressierten Rydbergzustands bestimmt werden. Der Hamilton-Operator des Systems lässt sich in semiklassischer Näherung als

$$\hat{\mathcal{H}} = \hat{\mathcal{H}}_0 + \hat{\mathcal{H}}_{WW} \tag{1.3}$$

beschreiben. Dabei ist $\hat{\mathcal{H}}_0$ der Hamilton-Operator des ungestörten Systems und $\hat{\mathcal{H}}_{WW} = \vec{d}\cdot\vec{E}$ der Hamilton-Operator der Wechselwirkung zwischen dem elektrischen Dipol-Operator $\vec{d}$ des Atoms und dem elektrischem Feldvektor $\vec{E}$ des Lichts. Die Mastergleichung in Lindblad-Form des Systems ergibt sich nun zusammen mit der Dichtematrix ρ zu

$$i\hbar\dot{\rho} = [\hat{\mathcal{H}}, \rho] + \hat{\mathcal{U}}(\rho). \tag{1.4}$$

Der Kommutator beschreibt hierbei die kohärente Zeitentwicklung des Systems unter Einfluss von $\mathcal{H}$, während $\hat{\mathcal{U}}$ den strahlenden Zerfall der Besetzungen und den nicht-strahlenden Zerfall der Kohärenzen der beteiligten Zustände mit einbezieht. $\hat{\mathcal{U}}$ ist nicht hamiltonsch und verursacht dadurch eine nicht-unitäre Entwicklung des Systems.

Die Mastergleichung 1.4 ist mithilfe der *rotating wave approximation* im stationären Fall $\dot{\rho} = 0$ analytisch lösbar [24]. Bedingungen für die *rotating wave approximation* sind, dass die optischen Frequenzen in der Nähe der atomaren Resonanzen liegen und das System nur schwach gestört wird. Aus den Lösungen für ρ lässt sich die Suszeptibilität $\chi(\omega_p)$ des atomaren Gases für den Testlaser ableiten. Der Imaginärteil $\Im(\chi(\omega_p))$ beschreibt die Absorption des Testlasers durch die Atome. Ist der Testlaser resonant mit der atomaren Übergangsfrequenz ω_{21} unter Abwesenheit oder Verstimmung des Kopplungslasers wird er maximal absorbiert. Ist der Kopplungslaser resonant mit der Übergangsfrequenz ω_{32} erscheinen die Atome für den Testlaser transparent. Für die Messung der Energieniveaus von Rydbergatomen im Rahmen dieser Arbeit ist EIT im stationären Fall die Grundlage [1, 2, 4] .

Für dynamische Systeme mit $\dot{\rho} \neq 0$ lässt sich die Mastergleichung numerisch lösen. Aus den Lösungen für die zeitabhängige Dichtematrix ρ können die Absorption des Testlasers durch die Atome und die Besetzungen der atomaren Zustände bestimmt werden. Diesen Aspekt der Mastergleichung haben wir für unser Schema für die Detektion von Rydbergatomen ausgenutzt [5].

1.4 Rydbergpopulationen und Kohärenzen

Die Population von Rydbergzuständen wird experimentell durch *selektive Feldionisation* (SFI) der Rydbergatome mit anschließender Ionendetektion gemessen [25]. Dazu werden Elektroden genutzt, die zu einem bestimmten Zeitpunkt ein ausreichend hohes elektrisches Feld zur Ionisation aller vorhandenen Rydbergatome oder aber auch eine Feldrampe zur Ionisation der einzelnen Rydbergzustände mit zeitlichem Abstand anlegen. Mit einer Ionenoptik werden die Ionen oder die Elektronen anschließend zur Multi-Channel-Plate oder dem Channeltron geleitet. Die Detektionseffizienz erreicht dabei bis zu 90 %. Zustandsselektivität und die Messung kohärenter Superpositionen atomarer Zustände mit Ramsey-Interferometrie sind mit dieser Methode möglich [26–29].

Nachdem der EIT-Effekt sich für die Messung der Energieniveaus von Rydbergatomen als erfolgreiches Konzept erwiesen hat, stellten wir uns die Frage, ob es auch zur Messung

der Besetzung eines Rydbergzustands verwendet werden kann. Im Allgemeinen wird davon ausgegangen, dass der EIT-Effekt für diese Anwendung nicht geeignet ist, da meistens nur der stationäre Fall betrachtet wird [30]. In diesem ist die Information über den Ausgangszustand allerdings bereits verloren. Unsere Untersuchung zu diesem Thema im Rahmen dieser Arbeit zeigt hier neue Detektionsmöglichkeiten auf [5].

2 Zielsetzung

Das Ziel der Arbeit war die Untersuchung von Rydbergatomen in Hinblick auf ihre Anwendung für Quantensimulationen in Atom/Festkörper-Hybridsystemen. Zum Erreichen dieses Ziels sollten die experimentellen Grundlagen, wie ein frequenzstabilisiertes Lasersystem für die Anregung, Manipulation und Detektion, Spektroskopiezellen sowie eine Apparatur zur Erzeugung von ultrakalten Gasen, realisiert werden. Insbesondere war ein Ziel die Entwicklung einer Technik zur zustandsselektiven Detektion der Besetzung von Rydbergzuständen unter Ausnutzung des EIT-Effekts. Weatherill u. a. [30] benutzten den EIT-Effekt, um ultrakalte Rydbergatome zu spektroskopieren. Sie konnten die Besetzung des Rydbergzustands im stationären Fall bestimmen. Ziel unserer Untersuchungen war es eine Technik zu entwickeln, die als Alternative zur SFI-Methode genutzt werden kann. Dazu ist es entscheidend die Besetzung der Energieniveaus vor Beginn der Messung zu bestimmen, was im stationären Fall nicht möglich ist.

Für die optische Manipulation von Rydbergatomen ist eine genaue Kenntnis der Übergangsfrequenzen zwischen Grundzustand und Rydbergzuständen erforderlich. Ziel im Rahmen der Arbeit war es, dies für ^{87}Rb mithilfe aktueller Spektroskopietechniken und hoher spektraler Auflösung zu erreichen. Li u. a. [8] untersuchten den Quantendefekt für die nS- und nD-Linien von ^{85}Rb mit einer relativen Frequenzauflösung von ≈10 kHz. Aufgrund der Isotopieverschiebung lassen sich aus diesen Daten die absoluten Übergangsfrequenzen für ^{87}Rb nicht berechnen. Die genauesten absoluten Messungen dieser Übergangsfrequenzen für ^{87}Rb waren vor Beginn unserer Untersuchungen die Arbeiten von Stoicheff und Weinberger [31] aus dem Jahr 1979 mit einer Genauigkeit von ≈100 MHz. Aus den Übergangsfrequenzen lässt sich auch das Potential des Atomrumpfs berechnen. Das von Marinescu u. a. [20] entwickelte parametrische Potential für Alkalimetalle hat sich hierfür als Standard etabliert. Eine genaue Berechnung der zugehörigen Übergangsfrequenzen ergab jedoch eine Abweichung von den experimentellen Werten von bis zu 200 GHz [21].

Darüber hinaus sollte das Verhalten von Rydbergatomen in ultrakalten Rubidiumwolken in der Nähe einer Oberfläche untersucht werden. Energieverschiebungen der Rydbergzustände wurden durch Casimir-Polder-Wechselwirkungen zwischen der Oberfläche und den Atomen [32, 33] und durch inhomogene elektrische Felder von Adsorbaten erwartet [34, 35]. Tauschinsky u. a. [36] verwendeten im Jahr 2010 den EIT-Effekt zur Untersuchung von Rydbergatomen an einer Goldoberfläche und stellten fest, dass das elektrische Feld der Adsorbate die Messergebnisse dominiert und Casimir-Polder-Wechselwirkungen überlagert. Ihr Artikel war zum Zeitpunkt unserer Untersuchungen noch nicht veröffentlicht.

Der Stark-Effekt spielt bei Experimenten mit ultrakalten Rydbergatomen an Oberflächen eine wichtige Rolle. Deswegen war die präzise Charakterisierung dieses Effekts für ^{87}Rb ein weiteres Ziel. Die Aufspaltung der spektralen Linien von Natrium, Lithium und Cäsium in Rydbergzuständen mit der Hauptquantenzahl $n \leq 20$ im elektrischen Feld bis zur Ionisationsgrenze wurde bereits in den 1970er Jahren in der Gruppe von Daniel Kleppner untersucht [37, 38]. Aus diesen Studien stammt das auch heute noch verwendete Modell zur numerischen Simulation des Stark-Effekts. Die Aufspaltung von ^{85}Rb für niedrige elektrische Feldstärken und Hauptquantenzahlen bis $n = 55$ wurde in den 1980er Jahren untersucht [39]. Neuere Experimente zum Stark-Effekt von Rubidium nutzten EIT oder SFI mit hoher spektraler Auflösung, allerdings nur in niedrigen Bereichen der elektrischen Feldstärke [40–43].

3 Ergebnisse

3.1 Quantendefekt von ^{87}Rb

Im Rahmen dieser Arbeit untersuchten wir die Übergangsfrequenzen zu nS und nD Linien von ^{87}Rb [1]. Mithilfe des EIT-Effekts konnten sie an einer beheizten Rubidium-Dampfzelle mit einer Genauigkeit von 1 MHz gemessen werden(Abb. 3.1). Dies erreichten wir durch eine Frequenzstabilisierung der verwendeten Laser mit einem Frequenzkamm und einem Wellenlängenmessgerät (Abb. 3.2). Die Frequenz des Testlasers wurde mit dem Frequenzkamm auf Resonanz mit dem $|5S_{1/2}\rangle \rightarrow |5P_{3/2}\rangle$ Übergang von ^{87}Rb geregelt. Die Frequenz des Kopplungslasers wurde mit einem Wellenlängenmessgerät (HighFinesse WSU/2) stabilisiert, um mit hoher Frequenzgenauigkeit einen großen Bereich scannen und nach den Übergangsfrequenzen suchen zu können. Die Kalibrierung des Wellenlängenmessgeräts wurde anhand der Schwebung des Kopplungslasers mit dem Frequenzkamm überprüft und gegebenenfalls wiederholt. Die Intensität des Kopplungslasers modulierten wir mit einem Chopper, um durch eine Lock-In-Messung das Signal-Rausch-Verhältnis zu verbessern. Elektrische Felder spielten in diesem Aufbau keine Rolle, da durch die Autoionisation von Rydbergatomen freie Ladungsträger in der Dampfzelle vorhanden waren, die die zu messenden Atome wirkungsvoll abschirmten. Aus den gemessenen Daten berechneten wir den Quantendefekt und die Ionisationsenergie des Grundzustands für ^{87}Rb. Während die Genauigkeit der Werte für den Quantendefekt mit der Genauigkeit bereits vorhandener Daten von ^{85}Rb vergleichbar war [8], konnte die Ionisationsenergie des Grundzustands um zwei Größenordnungen genauer bestimmt werden als bei Stoicheff und Weinberger [31]. Aldridge u. a. [44] errechneten aus diesen und weiteren Daten die Isotopieverschiebung von ^{85}Rb und ^{87}Rb mit verbesserter Genauigkeit. Die Daten für die Energieniveaus von ^{87}Rb waren zudem der Ausgangspunkt in weiteren Untersuchungen dieser Arbeit für die theoretische Modellierung des Stark-Effekts [4], die Entwicklung des Rumpfpotentials [3] und für die Berechnung von Dipol-Dipol-Wechselwirkungen zwischen Rydbergatomen [5].

Aus der Kenntnis der Energieniveaus der Rydbergzustände von Rubidium lassen sich auch Rückschlüsse auf das Potential des Atomrumpfs ziehen. Mit dem bisher verwendeten parametrischen Potential von Marinescu u. a. [20] von 1994 wurden Abweichungen zwischen numerischen Simulationen und aktuelleren experimentellen Daten von bis zu 200 GHz festgestellt [21]. Da das Potential an die damals aktuellen Messdaten angepasst wurde, konnte durch eine Korrektur des Parameters a_3 eine deutlich bessere Übereinstimmung mit den neuesten Messungen erreicht werden ($a_3\,(l=0) \rightarrow 0.814 \times a_3\,(l=0)$ und

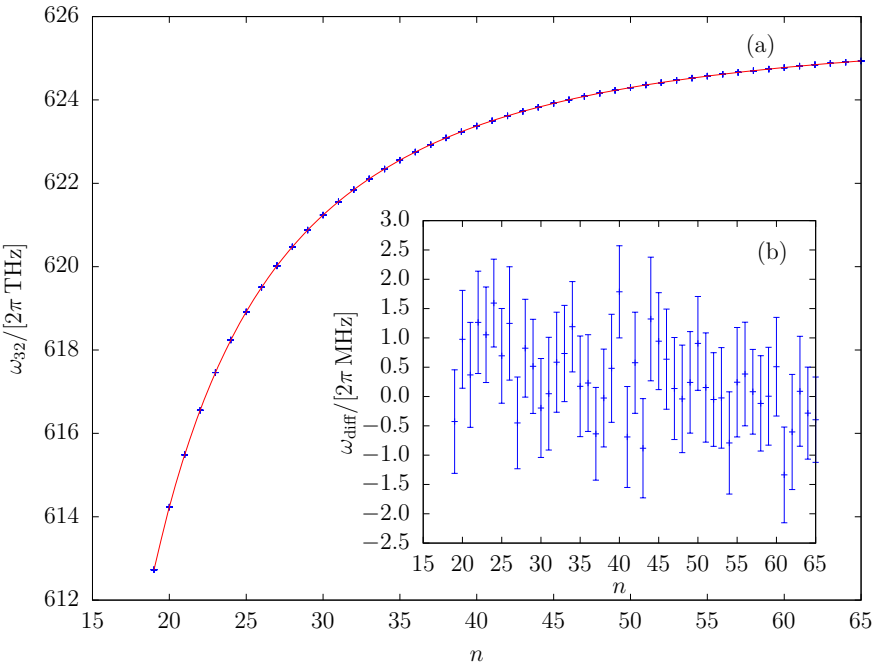

Abbildung 3.1: Übergangsfrequenzen ω_{32} zwischen $|5\mathrm{P}_{3/2}, F = 3\rangle$ und nS-Zuständen von ^{87}Rb
Die Hauptquantenzahl n wurde für die Messungen zwischen 19 und 64 variiert. Die durchgezogene, rote Kurve in (a) zeigt den Fit an ein theoretisches Modell für den Verlauf an. In (b) sind die Abweichungen ω_{diff} zwischen den Messdaten und der Theorie-Kurve dargestellt.

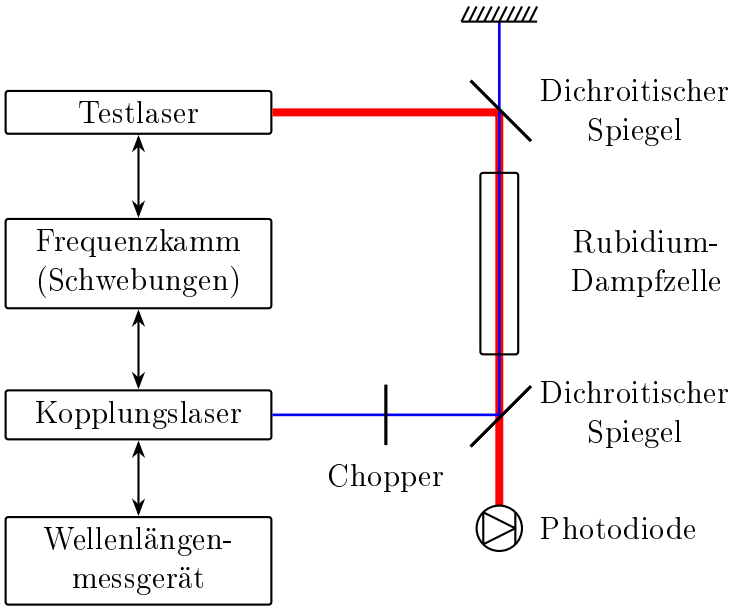

Abbildung 3.2: Schematischer Aufbau für die Messung des Quantendefekts von ^{87}Rb
Die Frequenz des Testlasers (rot) wurde mit dem Frequenzkamm, die des Kopplungslasers (blau) mit dem Wellenlängenmessgerät geregelt. Die Kalibrierung des Wellenlängenmessgeräts erfolgte durch die Schwebung des Kopplungslasers mit dem Frequenzkamm. Die dichroitischen Spiegel überlagerten die beiden Laserstrahlen. Der Chopper modulierte den Kopplungsstrahl für eine Lock-In-Messung. Mit der Photodiode wurde die Leistung des Testlaser gemessen. Wenn die Frequenz des Kopplungslasers kleiner oder größer als die Übergangsfrequenzen der Atome in der Rubidium-Dampfzelle war, wurde der Teststrahl absorbiert. Auf Resonanz bildete sich die elektromagnetisch induzierte Transparenz aus.

Tabelle 3.1: Feinstruktur $\Delta E_{n,l=2}$ der D-Zustände in [MHz], Vergleich zwischen theoretischen und experimentellen Ergebnissen.

Die Tabelle wurde der Veröffentlichung [3] entnommen und angepasst.

Zustand $\|n, l = 2\rangle$	**Exp. [45]**	**Exp. [8]**	**Exp. [1]**	**Theorie [21]**	**Theorie [3]**
8D	$30.4(4) \times 10^3$	N/A	N/A	113.17×10^3	36.42×10^3
10D	$14.9(2) \times 10^3$	N/A	N/A	52.05×10^3	16.56×10^3
30D	N/A	452.42(18)	452.5(11)	1447.53	456.13
35D	N/A	279.65(10)	280.4(11)	894.84	281.52
45D	N/A	128.33(4)	127.8(11)	407.64	128.98
55D	N/A	69.17(2)	69.4(11)	223.71	69.47
57D	N/A	61.98(2)	62.2(11)	197.39	62.24

$a_3\,(l = 2) \rightarrow 0.914 \times a_3\,(l = 2)$). Außer den Abweichungen beim Quantendefekt bzw. den Übergangsfrequenzen fiel auch eine Diskrepanz bei der Feinstrukturaufspaltung auf. Um diese richtig wiederzugeben, musste das Potential modifiziert werden. Da es keine mikroskopische Theorie für den Bereich des Atomrumpfs gibt, wurde das Potential in Kernnähe *a posteriori* verändert. Das modifizierte Potential stellt sich dann folgendermaßen dar:

$$V_{\text{mod}}\,(r; j, l) = \begin{cases} V_{\text{eff}}\,(r; l) & \text{für } 0 \leq r \leq r_{\text{so}}\,(l)\,, \\ \\ V_{\text{eff}}\,(r; l) + V_{\text{so}}\,(r; j, l) & \text{für } r > r_{\text{so}}\,(l)\,. \end{cases} \tag{3.1}$$

Dabei ist l der Bahndrehimpuls, j der Gesamtdrehimpuls, r der radiale Abstand zum Kern und V_{eff} das Potential ohne Feinstrukturaufspaltung. V_{so} beschreibt die Spin-Bahn-Kopplung. Entscheidend für den Vergleich mit den experimentellen Daten ist die Wahl der Größe r_{so}. Eine sehr gute Übereinstimmung von Theorie und Experiment für alle n besteht für (Beispiele in Tabelle 3.1):

$$r_{\text{so}}(l = 1) = 0{,}044\,282\,5, \tag{3.2}$$

$$r_{\text{so}}(l = 2) = 0{,}249\,572\,0. \tag{3.3}$$

Unsere Studie zeigt, dass moderne Spektroskopie-Techniken im Zusammenspiel mit den Energieniveaus von Rydbergatomen einen Zugang zu dem Problem der Multi-Elektronen-Korrelationen in Atomrümpfen von Alkalimetallen ermöglichen.

3.2 Stark-Effekt von Rydbergatomen

Für die präzise Charakterisierung des Stark-Effekts fertigten wir eine Rubidium-Dampfzelle mit integriertem Kondensator an. In dieser konnten elektrische Felder von bis zu 500 V/cm erzeugt werden. In unserer Studie haben wir den Stark-Effekt mithilfe der EIT für die Hauptquantenzahlen $n = 35$ und $n = 70$ gemessen. Das Experiment diente zur Verifizierung der

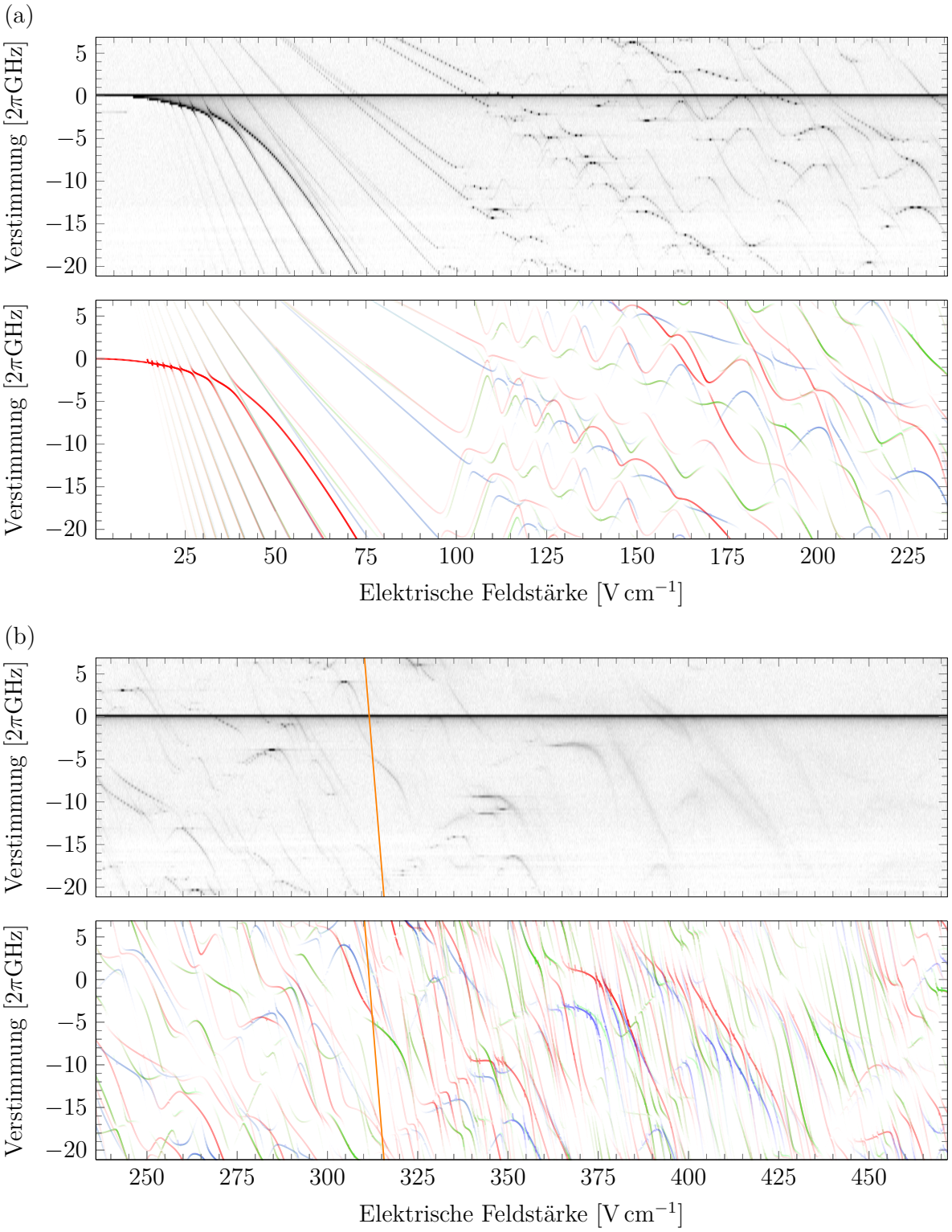

Abbildung 3.3: Stark-Effekt in Experiment und Theorie
In den Diagrammen sind Messungen (jeweils oberes Bild) und numerische Simulationen (jeweils unteres Bild) des Stark-Effekts im Frequenzbereich um den unverschobenen $35S_{1/2}$-Zustand dargestellt. Die elektrische Feldstärke beträgt in (a) 0 V/cm – 235 V/cm und in (b) 235 V/cm – 470 V/cm. Die Stärke des EIT-Effekts ist in den Messungen durch Graustufen und in der numerischen Simulation durch die Farbintensität von rot, grün bzw. blau für $|m_j| = 1/2$, $|m_j| = 3/2$ bzw. $|m_j| = 5/2$ abgebildet. Die Ionisationsgrenze ist in orange eingezeichnet. Die Abbildungen wurden der Veröffentlichung [4] entnommen und angepasst.

Theorie zum Stark-Effekt von Zimmerman u. a. [38] für Bereiche der Hauptquantenzahl n und der angelegten elektrischen Feldstärke, die deutlich über die bisher veröffentlichten Daten hinausgehen. Die Frequenzauflösung war dabei bis zu 2 MHz und die Auflösung des elektrischen Felds bis zu 10 mV/cm. Außerdem wurden EIT-Signale jenseits der klassischen Ionisationsgrenze gemessen. Für diesen Feldbereich war ein sehr gutes Signal-Rausch-Verhältnis wichtig, da die Signalstärke im Vergleich zu feldfreien Messungen stark abnimmt. Wir benutzten eine frequenzmodulierte Lock-In-Technik, um eine ausreichend gute Signalqualität zu erreichen. Dabei wurde nicht nur die Intensität des Kopplungslasers moduliert, sondern auch zusätzlich die Frequenz dieser Modulation. Das Messrauschen wurde dadurch noch effektiver als bei der klassischen Lock-In-Technik mit reiner Intensitätsmodulation unterdrückt.

Die für die theoretische Beschreibung des Stark-Effekts benötigten Wellenfunktionen von ^{87}Rb wurden aus den in der Rubidium-Dampfzelle gemessenen Energieniveaus mithilfe zweier Methoden berechnet. Zum einen wurde die von Zimmerman u. a. [38] beschriebene Methode mit dem Numerov-Verfahren und dem dort verwendeten Coulomb-Potential mit Rumpfpolarisierbarkeit genutzt. Zum anderen wurde das parametrische Potential von Marinescu u. a. [20] zusammen mit der ODE45-Implementierung von MATLAB 2014a verwendet. Die Wellenfunktionen wiesen leichte Unterschiede in Kernnähe auf, waren aber in weiter entfernten Bereichen nicht unterscheidbar. Die auf den Wellenfunktionen basierenden Beschreibungen des Stark-Effekts zeigten keine signifikanten Unterschiede in den Bereichen, in denen experimentelle Daten vorliegen. Zusätzlich konnte mithilfe der berechneten Dipolmatrixelemente die Stärke des EIT-Signals abgeschätzt und mit den Messergebnissen verglichen werden. Die Übereinstimmung zwischen Experiment und numerischen Simulationen war für fast den gesamten Bereich sehr gut (Abb. 3.3). Nur im Bereich hoher elektrischer Feldstärken ließen sich größere Abweichungen für die Übergangsstärken finden. Diese waren am stärksten für Zustände mit $|m_j| = \frac{1}{2}$ und weniger ausgeprägt für Zustände mit $|m_j| = \frac{3}{2}$ oder $|m_j| = \frac{5}{2}$. In die beiden letzteren mischen keine S-Wellenfunktionen. Dies lässt den Rückschluss zu, dass die Wellenfunktionen der S-Zustände stärker fehlerbehaftet waren, als diejenigen für Zustände mit $l > 0$. Da S-Wellenfunktionen eine höhere Aufenthaltswahrscheinlichkeit in Kernnähe haben und stärker an Kontinuumszustände koppeln, erscheint dieser Sachverhalt plausibel. Offen für zukünftige Untersuchungen ist die Frage, ob sich mit genaueren S-Wellenfunktionen durch ein verbessertes Potential wie in der Studie von Sanayei u. a. [3] eine präzisere Vorhersage der Signalstärken der EIT erreichen lässt.

Eine Anwendung des Stark-Effekts der Rydbergatome liegt in der Möglichkeit elektrische Felder präzise zu vermessen. In diesem Zusammenhang haben wir ein inhomogenes elektrisches Feld in der Nähe einer Oberfläche untersucht. Dazu wurde eine ultrakalte Atomwolke aus ^{87}Rb-Atomen auf eine Kupferoberfläche fallen gelassen und durch eine Absorptionsabbildung zu einem Zeitpunkt abgebildet, zu dem sich die Atome in einem Abstand von 30 µm – 300 µm von der Oberfläche befanden. Zeitgleich mit der Absorptionsabbildung wurde ein Laser mit einer Wellenlänge von ≈480 nm eingestrahlt. Im Sinne des EIT-Schemas

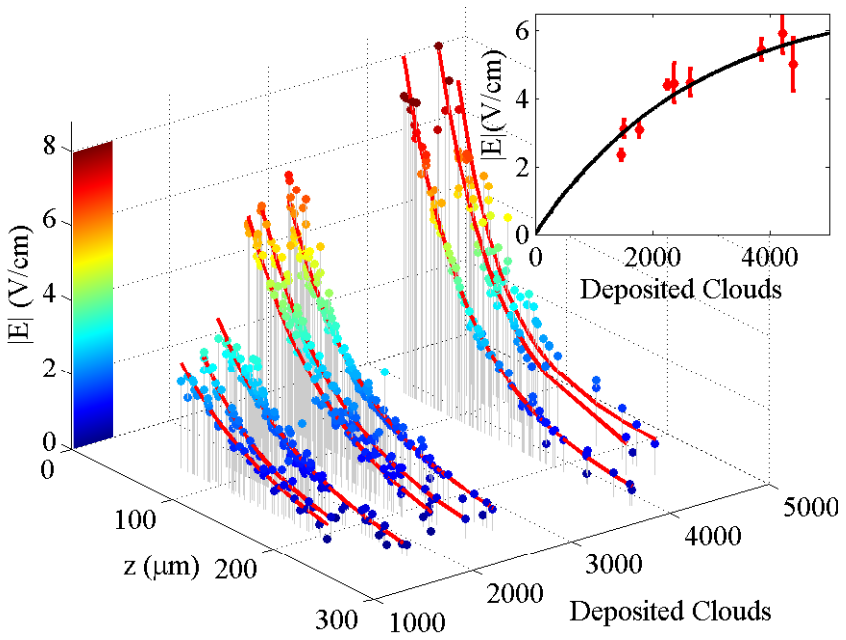

Abbildung 3.4: Elektrostatischer Feldverlauf über der Oberfläche
Die Zunahme der adsorbierten Rubidiumatome an der Oberfläche lässt sich an der Zunahme des elektrischen Feldes in Abhängigkeit der Anzahl an ausgeführten experimentellen Zyklen ablesen. Die kleinere Grafik zeigt das elektrostatische Feld in einem Abstand von 80 µm. Nach einigen Tausend Zyklen tritt eine Sättigung ein. Die Abbildung wurde der Veröffentlichung [2] entnommen und angepasst.

stellt der Laser der Absorptionsabbildung den Testlaser und der zweite Laser den Kopplungslaser dar. Die Frequenz des Kopplungslasers wurde im Verlauf der Messung um die atomare Resonanz gescannt. Durch die Adsorbate auf der Oberfläche wurde ein inhomogenes elektrisches Feld erzeugt, das Atome in einem bestimmten Abstand aufgrund des Stark-Effekts in Resonanz brachte und damit transparent für die Abbildung werden ließ. Auf diese Art und Weise benutzten wir Rydbergatome als empfindliche Sensoren für elektrische Felder. Das durch die adsorbierten Atome verursachte elektrische Dipolfeld konnte präzise charakterisiert und ein Zusammenhang zwischen der zunehmenden Beschichtung der Kupferoberfläche mit Rubidium und der Anzahl der dort fallen gelassenen ultrakalten Wolken nachgewiesen werden (Abb. 3.4). Dieses veränderliche Feld muss beachtet werden, wenn Atome mit Festkörpersystemen gekoppelt werden sollen [2].

3.3 Optische Detektion von Rydbergpopulationen und Kohärenzen

Der EIT-Effekt im stationären Fall bietet, wie in den vorangegangenen Abschnitten dargestellt, einen sehr präzisen Zugang zu den Energieniveaus der Rydbergatome. Darüber hinaus sind in beinahe jedem Labor, in dem mit Rydbergatomen experimentiert wird, die für seine Anwendung benötigten Laser vorhanden, da sie auch zur Anregung eingesetzt werden. Unter anderem aus diesen beiden Gründen haben wir untersucht, wie EIT für die Detekti-

on der Besetzung von Rydbergzuständen genutzt werden kann. Dazu muss der EIT-Effekt zeitaufgelöst betrachtet und die Dynamik verstanden werden. Durch die Wahl geeigneter Laserpulse und der zeitaufgelösten Messung der Absorption des Testlasers durch die Atome lässt sich die Population des Rydbergzustands vor Beginn der Pulssequenz mit einer Genauigkeit von $\pm 1\,\%$ berechnen [5].

Für diese Studie richteten wir ein Labor inklusive eines Vakuum- und eines Lasersystems für die Erzeugung ultrakalter Rubidium-Gase ein. Die Atome wurden in einer magnetooptischen Falle gefangen und gekühlt. Anschließend wurden sie in eine Magnetfalle umgeladen und am Ende aus dieser fallen gelassen. Zur Charakterisierung der Atomzahl, der Temperatur und der Dichte der ultrakalten Wolke verwendeten wir eine Absorptionsabbildung. Alle diese Komponenten entsprachen den Standard-Konfigurationen für Experimente mit ultrakalten Atomen. Eine Besonderheit in dieser Untersuchung war die Stabilisierung der Frequenzen aller verwendeten Laser mit Schwebungstabilisierungen auf einen Frequenzkamm. Die Linienbreiten der Laser, die Rydbergatome anregen, manipulieren oder detektieren, wurden zusätzlich reduziert. Durch Regelungen mit hoher Bandbreite von bis zu 2 MHz auf optische Resonatoren konnten die Linienbreiten von $\approx$100 kHz auf $<$10 kHz im Verhältnis zu diesen Resonatoren verkleinert werden. Durch dieses Vorgehen erreichten wir eine absolute Präzision im Bereich von 10 kHz für die optischen Frequenzen. Die zeitaufgelösten Messungen des EIT-Effekts wurde durch ein System aus Radiofrequenz-Synthesizern, akustooptischen Modulatoren und schnellen Photodetektoren ermöglicht, das eine Bandbreite von $>$10 MHz besaß.

In den Experimenten, die in der Veröffentlichung [5] dargestellt werden, hatte die Atomwolke eine Temperatur von 150 µK. Um Störungen durch magnetische und elektrische Felder zu vermeiden, startete die Pulssequenz 3 ms nach Ausschalten der Magnetfalle. Da sie innerhalb von weniger als 100 µs wieder endete, spielten die Bewegungen der Atome keine Rolle. Die beiden Laser des EIT-Schemas wurden aus gegenüberliegenden Richtungen eingestrahlt und ihre Frequenzen waren jeweils mit den atomaren Übergängen $|1\rangle \rightarrow |2\rangle$ bzw. $|2\rangle \rightarrow |3\rangle$ resonant (Abb. 1.1). Die Intensität des Testlasers wurde mit einer empfindlichen Photodiode und einer Zeitauflösung von 20 ns gemessen. Aus den aufgenommen Werten der Photodiode $I_{\mathrm{T}}(t)$ wurde die optische Dichte $\mathrm{OD}(t)$ berechnet, indem diese mit einer Aufnahme der Laserintensität ohne Atome $I_{\mathrm{ref}}(t)$ verglichen wurde. Dazu wurde

$$\mathrm{OD}(t) = -\ln\left(\frac{I_{\mathrm{T}}(t)}{I_{\mathrm{ref}}(t)}\right) \tag{3.4}$$

genutzt. Die Ergebnisse dieser Berechnungen wurden normalisiert, so dass relative optische Dichten wie in Abbildung 3.5(b) für den Vergleich mit den Ergebnissen der numerischen Simulation zur Verfügung standen.

Damit alle Atome am Ende wieder den gleichen Grundzustand $|5\mathrm{S}_{1/2}, F = 2\rangle$ und nicht $|5\mathrm{S}_{1/2}, F = 1\rangle$ erreichten, wurde ein Rückpumplaser während der gesamten Pulssequenz angelassen. Die Pulssequenz beinhaltete die drei Abschnitte A, B und C (Abb. 3.5(a)). Im

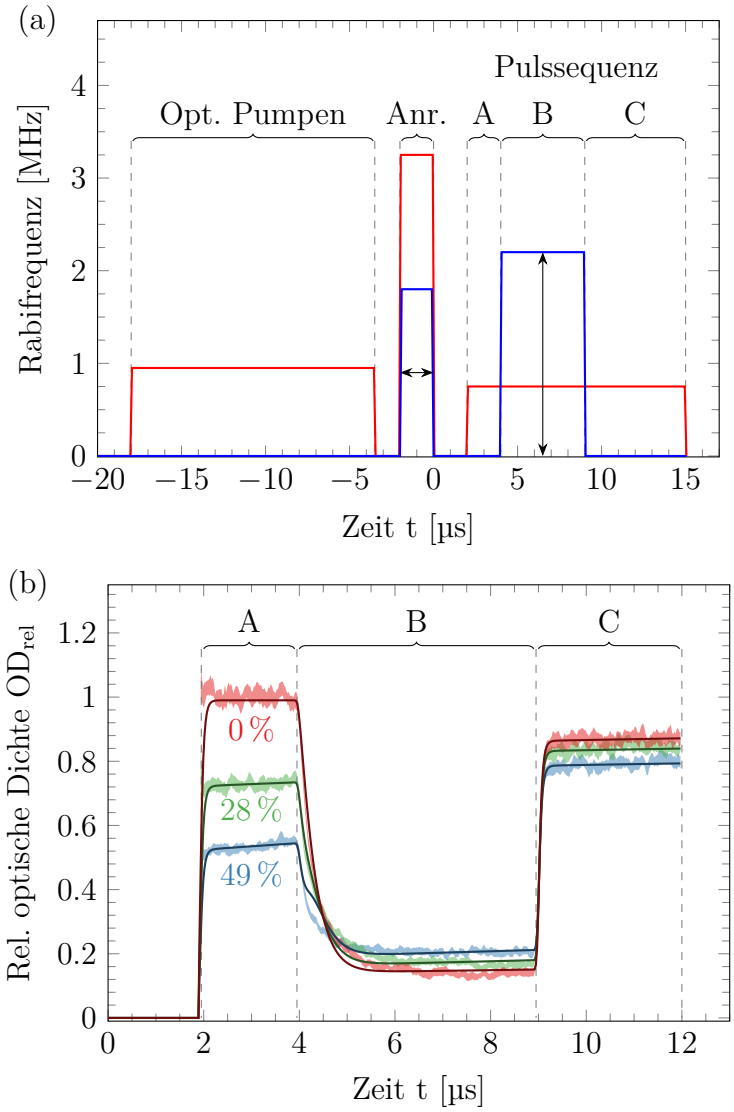

Abbildung 3.5: Pulssequenz zur Messung der Rydbergpopulation (a) und damit gemessene relative optische Dichten (b)

(a): Am Ende der Präparation wurden alle Atome optisch in den passenden Polarisationszustand gepumpt (Opt. Pumpen). Danach wurde ein Teil der Atome in den Rydbergzustand angeregt (Anr.). Die zeitliche Entwicklung der optischen Dichte wurde anschließend während der Pulssequenz mit dem Testlaser (rot) gemessen (A, B, C). Der Kopplungslaser (blau) wurde im Intervall B zusätzlich eingestrahlt.

(b): In rot, grün und blau sind die relativen optischen Dichten für drei unterschiedliche Messungen gemeinsam mit den Ergebnissen der numerischen Simulationen dargestellt. Dabei bezeichnet die Prozentzahl den jeweiligen, in der Auswertung bestimmten, Anteil der Atome im Rydbergzustand zum Zeitpunkt $t = 0$. Im Intervall A wurde der Anteil der Atome, die sich nicht im Grundzustand befanden, bestimmt. In Kombination mit den Intervallen B und C konnte der genaue Anteil der Atome im adressierten Rydbergzustand berechnet werden. Während des EIT-Intervalls (B) ist zu erkennen, dass die Transparenz umso kleiner war, je mehr Atome sich im Rydbergzustand befanden. Dies ist eine Folge der Dipol-Dipol-Wechselwirkung zwischen Rydbergatomen in Zustand $|3\rangle$ und $|4\rangle$. Im Intervall C sind ebenfalls unterschiedliche optische Dichten zu erkennen. Dies liegt daran, dass bei stärkerer Anregung in den Rydbergzustand durch Schwarzkörperstrahlung und Superradianz mehr Atome in den Reservoir-Zustand $|4\rangle$ umverteilt wurden. Die Abbildungen wurden der Veröffentlichung [5] entnommen und angepasst.

Teil A wurde nur der Testlaser eingestrahlt, um die Besetzung des Grundzustands zu bestimmen. Im Intervall B wurde EIT durch den Kopplungslaser erzeugt. Mit der Analyse dieses Abschnitts bestimmten wir, ob die fehlenden Besetzungen des Grundzustands aus Intervall A im adressierten Rydbergzustand oder in anderen waren. Im letzten Abschnitt C wurde wieder nur der Testlaser eingestrahlt. Die Analyse dieses Abschnitts nutzten wir, um Effekte wie Ionisation und andere Verluste der Atome auszuschließen. Dazu wurde die relative optische Dichte bis zu 1 ms lang gemessen. Nach dieser Zeit war sie bei allen Messungen wieder bei 1.

Als theoretisches Modell zur Beschreibung und zum Verständnis der Ergebnisse entwickelten wir eine numerische Simulation auf Basis einer Mastergleichung in Lindblad-Form (1.4). Für die Theorie des EIT-Effekts wird zwar lediglich ein Drei-Niveau-System benötigt, allerdings besitzen Rubidiumatome in der Praxis sehr viele relevante Energieniveaus. Obwohl ^{87}Rb zwei Grundzustände hat, wurde durch das optische Pumpen und den Rückpumplaser nur $|5S_{1/2}, F = 2\rangle \mathrel{\widehat{=}} |1\rangle$ besetzt, so dass wir keine weiteren Grundzustände in unser Modell einbeziehen mussten. Durch die EIT-Laser wurden die Zustände $|5P_{3/2}, F = 3\rangle \mathrel{\widehat{=}} |2\rangle$ und $|35S_{1/2}\rangle \mathrel{\widehat{=}} |3\rangle$ angeregt. Ein Populationstransfer aufgrund von Stößen konnte für dieses System wegen der geringen Dichte und den kurzen Zeitskalen vernachlässigt werden. Ein Effekt, der jedoch nicht vernachlässigt werden konnte, ist der Populationstransfer in energetisch naheliegende Rydbergzustände. Die Übergänge wurden von der Schwarzkörperstrahlung der ≈300 K warmen Umgebung angeregt, da die Frequenzen dieser Dipolübergänge im Bereich von ≈100 GHz liegen. Um dieser Tatsache Rechnung zu tragen, nutzten wir ein viertes, virtuelles Energieniveau $|4\rangle$, das sogenannte Reservoir, das alle Rydbergzustände außer $|3\rangle$ beinhaltete [30]. Da die Wellenlängen der Übergänge von $|3\rangle \to |4\rangle$ bis zu 3 mm und die Größe der Atomwolke ≈1 mm betrug, erwarteten wir Wechselwirkungen zwischen unterschiedlichen Rydbergatomen und damit kollektive Effekte für diesen Übergang. Der Hamilton-Operator aus der Mastergleichung (1.4) bezieht sich auf ein einzelnes Atom. Die Erweiterung des Operators auf viele Atome würde eine numerische Lösung auf aktuellen Computern verhindern. Deswegen integrierten wir die zu erwartende Superradianz [46] zusammen mit den Auswirkungen der Schwarzkörperstrahlung in die Rate der Übergänge von $|3\rangle \to |4\rangle$,

$$\tilde{\Gamma}_{34}(t) = \Gamma_{34,\mathrm{sp}} \cdot [\rho_{44}(t) \cdot p_{\mathrm{sup}} + 1] + \Gamma_{34,\mathrm{bb}}. \tag{3.5}$$

$\Gamma_{34,\mathrm{sp}}$ ist dabei die spontane Übergangsrate, $\rho_{44}(t)$ die zeitabhängige Besetzung von $|4\rangle$, p_{sup} ein Parameter, der die Stärke der Superradianz beschreibt, und $\Gamma_{34,\mathrm{bb}}$ die Übergangsrate, die durch die Schwarzkörperstrahlung verursacht wird. $\tilde{\Gamma}_{34}(t)$ wurde durch die Modifikation zu einer zeitabhängigen Rate. Alle spontanen und durch Schwarzkörperstrahlung verursachten Übergangsraten wurden mithilfe der Wellenfunktionen ausgerechnet, die in den vorherigen Untersuchungen [1, 4] berechnet und mit Messungen verifiziert wurden [47, 48].

Ein weiterer Effekt, der durch Wechselwirkungen zwischen Rydbergatomen verursacht

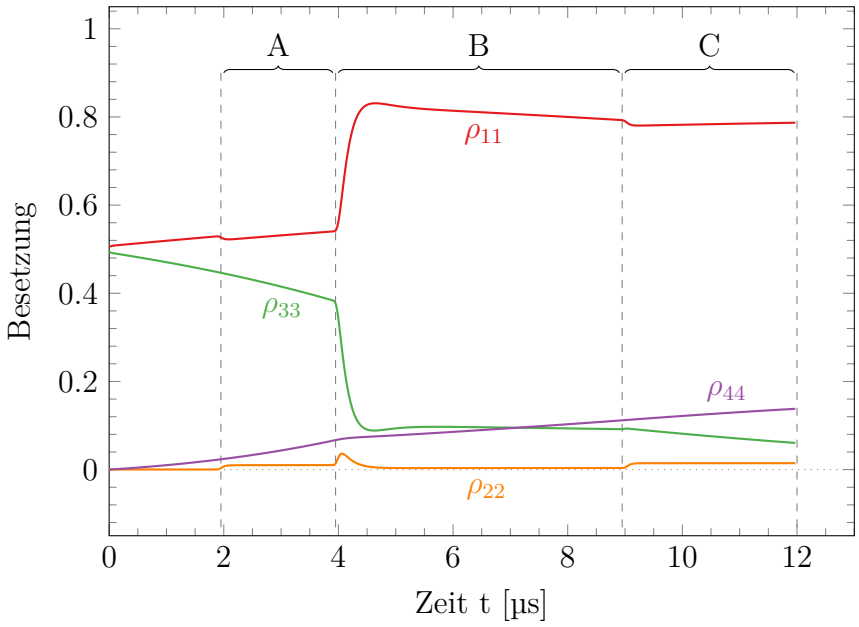

Abbildung 3.6: Dynamik der Populationen
Die dargestellten Besetzungen wurden aus dem Datensatz mit einer Anregung von 49 % aus Abbildung 3.5(b) berechnet. Die anfängliche Anregung in $|35S_{1/2}\rangle$ betrug dementsprechend $\rho_{33}(0) = 49\,\%$. Sofort begann der Zerfall in den Grundzustand $|5S_{1/2}\rangle$ mit der Besetzung $\rho_{11}(t)$ und den Reservoirzustand mit der Besetzung $\rho_{44}(t)$. Zu Beginn des EIT-Intervalls (B) wurde ein großer Teil der Besetzung des Rydbergzustands zurück in den Grundzustand gepumpt. Die Abbildung wurde der Veröffentlichung [5] entnommen und angepasst.

wird, ist eine scheinbare Dekohärenz der atomaren Zustände. Da die im Zustand $|4\rangle$ vorhandenen Atome sich hauptsächlich in P-Zuständen befinden und diese zufällig, d.h. in variablen Abständen, innerhalb der Atomwolke verteilt sind, wird die Phase durch Dipolkräfte zwischen Rydbergatomen in S- und Rydbergatomen in P-Zuständen für jedes Atom unterschiedlich beeinflusst. Bei einer gemittelten Messung über alle Atome erscheinen unterschiedliche Phasen als Dekohärenz [49]. Diesen Effekt modellierten wir durch eine zeitabhängige Dephasierungsrate

$$\tilde{\gamma}_c(t) = \gamma_c + \gamma_{3,dd} \cdot \rho_{44}(t). \tag{3.6}$$

γ_c entspricht dabei der Dephasierung aufgrund des Phasenrauschens der Laser, $\gamma_{3,dd}$ ist der Parameter, der die Stärke des Dipol-Dipol-Dephasierungseffekts beschreibt. Dieser Sachverhalt erklärt, warum die Stärke des EIT-Effekts im Intervall B abhängig von der vorherigen Anregung von Rydbergatomen ist. Nur durch die Einbeziehung der Wechselwirkungen zwischen Rydbergatomen in das theoretische Modell lassen sich die Ergebnisse der Simulation und die Messergebnisse gut in Übereinstimmung bringen.

Ein Merkmal der Simulation ist die Möglichkeit, die Populationen der beteiligten Atomzustände zu jedem betrachteten Zeitpunkt ausgeben zu können (Abb. 3.6). Durch den Vergleich der errechneten Absorption mit der gemessenen relativen optischen Dichte kann die Übereinstimmung geprüft werden. Aus der Simulation ergibt sich nun nicht nur die Popula-

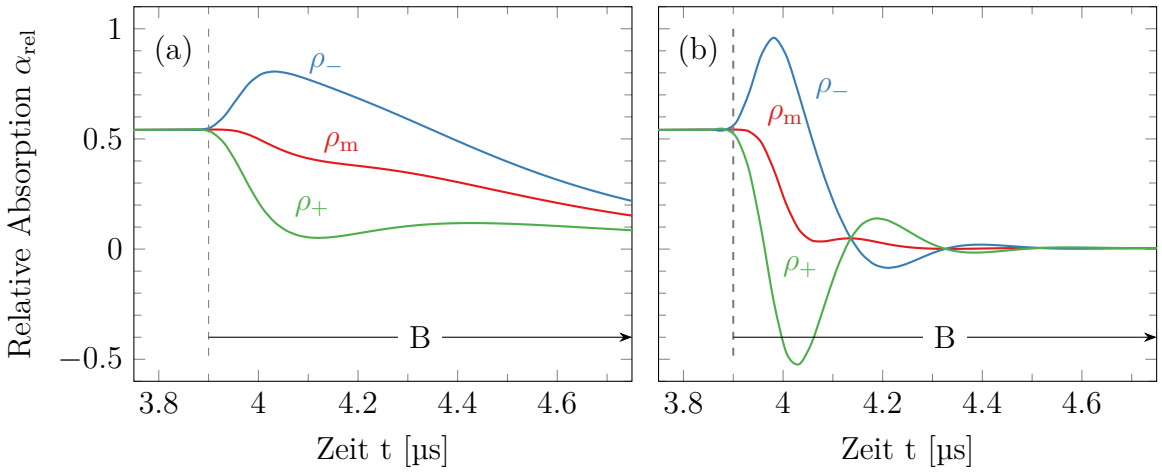

Abbildung 3.7: Messung der Kohärenz
Dargestellt ist die numerisch berechnete relative Absorption α_{rel} des Testlasers am Anfang des Intervalls B für Atome, die in den Zuständen $\rho_{\mathrm{m}}(t=0) = (|1\rangle\langle 1| + |3\rangle\langle 3|)/2$ (statistische Mischung) und $\rho_{\pm}(t=0) = \frac{1}{4}(|1\rangle \pm |3\rangle)(\langle 1| \pm \langle 3|)$ (kohärente Superposition) präpariert wurden. Die Parameter, die für (a) gewählt wurden, entsprechen denen, die im Experiment realisiert wurden. Für (b) wurde die Rabi-Frequenz des Kopplungslasers um einen Faktor 3 erhöht. In beiden Fällen ist der Unterschied signifikant und die Kohärenz direkt messbar. In (b) ist der Effekt noch deutlicher und ein Einschwingverhalten kann beobachtet werden. Dabei kann es sogar kurzfristig zu einer überhöhten Transmission, also negativer Absorption kommen. Die Abbildung wurde der Veröffentlichung [5] entnommen und angepasst.

tion des adressierten Rydbergzustands zu Beginn der Pulssequenz, wie es als Ziel formuliert war, sondern auch die zeitliche Entwicklung aller beteiligten Populationen über die gesamte Länge der Pulssequenz.

Die vorgestellte optische Detektionsmethode ermöglicht es, kohärente Superpositionen aus Grund- und Rydbergzustand zu messen. Da EIT ein kohärenter Effekt ist, lässt sich dies für eine Messung der Kohärenz ausnutzen. In unserem Experiment nutzten wir einen nicht-kohärenten Anregungspuls, weswegen wir den experimentellen Nachweis der Kohärenzmessung nicht durchführten. In den numerischen Simulationen untersuchten wir diesen Aspekt jedoch detailliert. Die Ergebnisse sind in Abbildung 3.7 dargestellt. Dazu wurden alle Parameter mit Ausnahme des Anregungspulses aus der experimentellen Situation übernommen, um realistische Bedingungen zu simulieren. Die Anregung wurde für diesen Fall vollständig kohärent angenommen. Am Beginn von Intervall B, während der Ausbildung des EIT-Effekts, zeigten sich deutliche Unterschiede für eine statistische Mischung von Rydberg- und Grundzustandsatomen im Vergleich zu Mischungen zwischen Rydberg- und Grundzustand. Bei Erhöhung der Rabi-Frequenz des Kopplungslasers können sogar eine Verstärkung des Testlasers durch konstruktive Interferenz und Rabi-Oszillationen beobachtet werden. Auch die Phase zwischen den atomaren Zuständen erscheint hier messbar.

Den Nutzen unserer rein optischen Detektionsmethode für Rydbergpopulationen haben wir in unserer Studie theoretisch und experimentell bestätigt. Für ultrakalte Atomwolken mit optischen Dichten zwischen 0,5 und 3 lässt sich damit der Anteil der Atome in einem Rydbergzustand mit hoher Genauigkeit messen. In Systemen mit mehr als einem Ryd-

bergzustand kann die Besetzung eines einzelnen Rydbergzustands ausgelesen werden, ohne die anderen zu beeinflussen. Dabei darf der Zustand energetisch unterhalb der anderen Rydbergzustände liegen. Dies ist ein großer Vorteil gegenüber der SFI-Methode, bei der alle energetisch höherliegenden Rydbergzustände bis zum adressierten Rydbergzustand ionisiert werden. Die Möglichkeit der direkten Messung der Kohärenz ist ein weiterer Vorteil unseres Schemas, der sich aus der Analyse der numerischen Simulationen ergab.

4 Ausblick

Die im Rahmen dieser Arbeit gemessenen absoluten Übergangsfrequenzen von ^{87}Rb, das daraus entwickelte Potential des Atomrumpfs und die Wellenfunktionen sowie die präzise Charakterisierung des Stark-Effekts erlauben die Konzeption von komplexen experimentellen Szenarien, wie dies zum Beispiel für Quantensimulationen mit Rydbergatomen oder für die Kopplung von Rydbergatomen an Mikrowellenresonatoren erforderlich ist. Das Problem der Oberflächenadsorbate, die auch im Rahmen dieser Arbeit durch Rydbergspektroskopie nachgewiesen wurden, bleibt noch zu lösen. Aus unseren Messungen des Stark-Effekts lassen sich jedoch Zustandspaare erkennen, die eine parallele differentielle Verschiebung ihrer Energieniveaus mit der elektrischen Feldstärke und daher eine konstante Übergangsfrequenz in einem begrenzten Feldbereich aufweisen. Solche Zustandspaare lassen sich auch durch Mikrowellen-Dressing generieren [50]. Somit rücken Rydbergatome als Bestandteil einer hybriden Quantenelektronik näher.

Die hier vorgestellte rein optische Detektion der Rydbergpopulation bietet ganz neue Perspektiven für Experimente mit Rydbergatomen. So können beispielsweise Rydbergzustände gemessen werden, die energetisch unterhalb von anderen besetzten Rydbergzuständen liegen, ohne diese zu beeinflussen. Da das Messschema im Gegensatz zu ionisierenden Methoden die Atome nicht aus dem experimentellen System entfernt, ist es in Studien mit wenigen oder sogar einzelnen Atomen einsetzbar [51]. Es kann in den meisten bestehenden Experimenten genutzt werden, da die benötigten Laser bereits vorhanden sind. Die Möglichkeit, die Kohärenz von Superpositionen atomarer Zustände nachzuweisen, erweitert die Anwendungsmöglichkeiten der vorgestellten Detektionsmethode zusätzlich. Im Vergleich zur Nutzung der SFI-Technik und der Ramsey-Interferometrie bietet sie den Vorteil, dass die Messung der Kohärenz in einem Schritt erfolgen könnte. Die Untersuchung dieses Aspekts der optischen Detektion von Rydbergzuständen soll in zukünftigen Studien erfolgen.

Rydbergatome sind durch die Möglichkeiten zur präzisen optischen Zustandspräparation, ihre starken Wechselwirkungen untereinander sowie ihre starke Kopplung an elektromagnetische Felder wichtige Bausteine der Forschung an Quantensystemen. Die hier präsentierte rein optische Manipulation und Detektion von Rydbergpopulationen und Kohärenzen ergänzen vorhandene Quantentechnologien um eine Methode, die dazu beitragen soll, vielseitige Quantensimulationen zu realisieren.

Literatur

[1] M. Mack, F. Karlewski, H. Hattermann, S. Höckh, F. Jessen, D. Cano und J. Fortágh, „Measurement of absolute transition frequencies of ^{87}Rb to nS and nD Rydberg states by means of electromagnetically induced transparency“, *Physical Review A* **83**, 052515 (2011).

[2] H. Hattermann, M. Mack, F. Karlewski, F. Jessen, D. Cano und J. Fortágh, „Detrimental adsorbate fields in experiments with cold Rydberg gases near surfaces“, *Physical Review A* **86**, 022511 (2012).

[3] A. Sanayei, N. Schopohl, J. Grimmel, M. Mack, F. Karlewski und J. Fortágh, „Quasiclassical quantum defect theory and the spectrum of highly excited rubidium atoms“, *Physical Review A* **91**, 032509 (2015).

[4] J. Grimmel, M. Mack, F. Karlewski, F. Jessen, M. Reinschmidt, N. Sándor und J. Fortágh, „Measurement and numerical calculation of Rubidium Rydberg Stark spectra“, *New Journal of Physics* **17**, 053005 (2015).

[5] F. Karlewski, M. Mack, J. Grimmel, N. Sándor und J. Fortágh, „State-selective all-optical detection of Rydberg atoms“, *Physical Review A* **91**, 043422 (2015).

[6] I. M. Georgescu, S. Ashhab und F. Nori, „Quantum simulation“, *Reviews of Modern Physics* **86**, 153–185 (2014).

[7] R. Blatt und D. Wineland, „Entangled states of trapped atomic ions“, *Nature* **453**, 1008–1015 (2008).

[8] W. Li, I. Mourachko, M. Noel und T. Gallagher, „Millimeter-wave spectroscopy of cold Rb Rydberg atoms in a magneto-optical trap: Quantum defects of the ns, np, and nd series“, *Physical Review A* **67**, 052502 (2003).

[9] J. Clarke und F. K. Wilhelm, „Superconducting quantum bits“, *Nature* **453**, 1031–1042 (2008).

[10] X. Peng, J. Zhang, J. Du und D. Suter, „Quantum Simulation of a System with Competing Two- and Three-Body Interactions“, *Physical Review Letters* **103**, 140501 (2009).

[11] P. Kok, K. Nemoto, T. C. Ralph, J. P. Dowling und G. J. Milburn, „Linear optical quantum computing with photonic qubits“, *Reviews of Modern Physics* **79**, 135–174 (2007).

[12] M. Saffman, T. G. Walker und K. Mølmer, „Quantum information with Rydberg atoms“, *Reviews of Modern Physics* **82**, 2313–2363 (2010).

[13] A. Sørensen, C. van der Wal, L. Childress und M. Lukin, „Capacitive Coupling of Atomic Systems to Mesoscopic Conductors“, *Physical Review Letters* **92**, 063601 (2004).

[14] D. Petrosyan und M. Fleischhauer, „Quantum Information Processing with Single Photons and Atomic Ensembles in Microwave Coplanar Waveguide Resonators“, *Physical Review Letters* **100**, 170501 (2008).

[15] S. Bernon, H. Hattermann, D. Bothner, M. Knufinke, P. Weiss, F. Jessen, D. Cano, M. Kemmler, R. Kleiner, D. Koelle und J. Fortágh, „Manipulation and coherence of ultra-cold atoms on a superconducting atom chip“, *Nature communications* **4**, 2380 (2013).

[16] T. F. Gallagher, *Rydberg atoms*, Digitally printed 1st pbk. version, Bd. 3, Cambridge University Press, 2005.

[17] E. Urban, T. A. Johnson, T. Henage, L. Isenhower, D. D. Yavuz, T. G. Walker und M. Saffman, „Observation of Rydberg blockade between two atoms“, *Nature Physics* **5**, 110–114 (2009).

[18] A. Gaëtan, Y. Miroshnychenko, T. Wilk, A. Chotia, M. Viteau, D. Comparat, P. Pillet, A. Browaeys und P. Grangier, „Observation of collective excitation of two individual atoms in the Rydberg blockade regime“, *Nature Physics* **5**, 115–118 (2009).

[19] C. Froese Fischer, T. Brage und P. Jönsson, *Computational atomic structure: An MCHF approach*, Institute of Physics Publ., 1997.

[20] M. Marinescu, H. Sadeghpour und A. Dalgarno, „Dispersion coefficients for alkali-metal dimers“, *Physical Review A* **49**, 982–988 (1994).

[21] M. Pawlak, N. Moiseyev und H. R. Sadeghpour, „Highly excited Rydberg states of a rubidium atom: Theory versus experiments“, *Physical Review A* **89**, 042506 (2014).

[22] K.-J. Boller, A. Imamolu und S. Harris, „Observation of electromagnetically induced transparency“, *Physical Review Letters* **66**, 2593–2596 (1991).

[23] A. K. Mohapatra, T. R. Jackson und C. S. Adams, „Coherent Optical Detection of Highly Excited Rydberg States Using Electromagnetically Induced Transparency“, *Physical Review Letters* **98**, 113003 (2007).

[24] M. Fleischhauer, A. Imamoglu und J. Marangos, „Electromagnetically induced transparency: Optics in coherent media“, *Reviews of Modern Physics* **77**, 633–673 (2005).

[25] R. Löw, H. Weimer, J. Nipper, J. B. Balewski, B. Butscher, H. P. Büchler und T. Pfau, „An experimental and theoretical guide to strongly interacting Rydberg gases“, *Journal of Physics B: Atomic, Molecular and Optical Physics* **45**, 113001 (2012).

[26] I. I. Ryabtsev, D. B. Tretyakov und I. I. Beterov, „Stark-switching technique for fast quantum gates in Rydberg atoms“, *Journal of Physics B: Atomic, Molecular and Optical Physics* **36**, 297–306 (2003).

[27] V. Nascimento, L. Caliri, A. d. Oliveira, V. Bagnato und L. Marcassa, „Measurement of the lifetimes of S and D states below $n = 31$ using cold Rydberg gas“, *Physical Review A* **74**, 054501 (2006).

[28] D. Tate, „Comment on "Measurement of the lifetimes of S and D states below $n = 31$ using cold Rydberg gas"“, *Physical Review A* **75**, 066502 (2007).

[29] L. Caliri und L. Marcassa, „Reply to "Comment on 'Measurement of the lifetimes of S and D states below $n = 31$ using cold Rydberg gas' "“, *Physical Review A* **75**, 066503 (2007).

[30] K. J. Weatherill, J. D. Pritchard, R. P. Abel, M. G. Bason, A. K. Mohapatra und C. S. Adams, „Electromagnetically induced transparency of an interacting cold Rydberg ensemble“, *Journal of Physics B: Atomic, Molecular and Optical Physics* **41**, 201002 (2008).

[31] B. P. Stoicheff und E. Weinberger, „Doppler-free two-photon absorption spectrum of rubidium“, *Canadian Journal of Physics* **57**, 2143–2154 (1979).

[32] J. A. Crosse, S. Å. Ellingsen, K. Clements, S. Y. Buhmann und S. Scheel, „Erratum: Thermal Casimir-Polder shifts in Rydberg atoms near metallic surfaces [Phys. Rev. A 82, 010901(R) (2010)]“, *Physical Review A* **82**, 029902 (2010).

[33] J. A. Crosse, S. Å. Ellingsen, K. Clements, S. Y. Buhmann und S. Scheel, „Thermal Casimir-Polder shifts in Rydberg atoms near metallic surfaces“, *Physical Review A* **82**, 010901 (2010).

[34] J. McGuirk, D. Harber, J. Obrecht und E. Cornell, „Alkali-metal adsorbate polarization on conducting and insulating surfaces probed with Bose-Einstein condensates“, *Physical Review A* **69**, 062905 (2004).

[35] J. Obrecht, R. Wild und E. Cornell, „Measuring electric fields from surface contaminants with neutral atoms“, *Physical Review A* **75**, 062903 (2007).

[36] A. Tauschinsky, R. M. T. Thijssen, S. Whitlock, H. B. van Linden van den Heuvell und R. J. C. Spreeuw, „Spatially resolved excitation of Rydberg atoms and surface effects on an atom chip“, *Physical Review A* **81**, 063411 (2010).

[37] M. Littman, M. Zimmerman, T. Ducas, R. Freeman und D. Kleppner, „Structure of Sodium Rydberg States in Weak to Strong Electric Fields“, *Physical Review Letters* **36**, 788–791 (1976).

[38] M. L. Zimmerman, M. G. Littman, M. M. Kash und D. Kleppner, „Stark structure of the Rydberg states of alkali-metal atoms“, *Physical Review A* **20**, 2251–2275 (1979).

[39] M. O'Sullivan und B. Stoicheff, „Scalar and tensor polarizabilities of ^{2}D Rydberg states in Rb“, *Physical Review A* **33**, 1640–1645 (1986).

[40] A. Grabowski, R. Heidemann, R. Löw, J. Stuhler und T. Pfau, „High resolution Rydberg spectroscopy of ultracold rubidium atoms“, *Fortschritte der Physik* **54**, 765–775 (2006).

[41] D. P. Fahey und M. W. Noel, „Excitation of Rydberg states in rubidium with near infrared diode lasers“, *Optics Express* **19**, 17002–17012 (2011).

[42] A. Tauschinsky, R. Newell, H. B. van Linden van den Heuvell und R. J. C. Spreeuw, „Measurement of ^{87}Rb Rydberg-state hyperfine splitting in a room-temperature vapor cell“, *Physical Review A* **87**, 042522 (2013).

[43] D. Barredo, H. Kübler, R. Daschner, R. Löw und T. Pfau, „Electrical Readout for Coherent Phenomena Involving Rydberg Atoms in Thermal Vapor Cells“, *Physical Review Letters* **110**, 123002 (2013).

[44] L. Aldridge, P. L. Gould und E. E. Eyler, „Experimental isotope shifts of the 5 $^2S_{1/2}$ state and low-lying excited states of Rb“, *Physical Review A* **84**, 034501 (2011).

[45] J. E. Sansonetti, „Wavelengths, Transition Probabilities, and Energy Levels for the Spectra of Rubidium“, *Journal of Physical and Chemical Reference Data* **35**, 301 (2006).

[46] J. O. Day, E. Brekke und T. G. Walker, „Dynamics of low-density ultracold Rydberg gases“, *Physical Review A* **77**, 052712 (2008).

[47] I. Beterov, I. Ryabtsev, D. Tretyakov und V. Entin, „Quasiclassical calculations of blackbody-radiation-induced depopulation rates and effective lifetimes of Rydberg nS, nP, and nD alkali-metal atoms with n$\leq$80“, *Physical Review A* **79**, 052504 (2009).

[48] T. Wang, S. Yelin, R. Côté, E. Eyler, S. Farooqi, P. Gould, M. Koštrun, D. Tong und D. Vrinceanu, „Superradiance in ultracold Rydberg gases“, *Physical Review A* **75**, 033802 (2007).

[49] W. Anderson, M. Robinson, J. Martin und T. Gallagher, „Dephasing of resonant energy transfer in a cold Rydberg gas“, *Physical Review A* **65**, 063404 (2002).

[50] L. Jones, J. Carter und J. Martin, „Rydberg atoms with a reduced sensitivity to dc and low-frequency electric fields“, *Physical Review A* **87**, 023423 (2013).

[51] H. Labuhn, S. Ravets, D. Barredo, L. Béguin, F. Nogrette, T. Lahaye und A. Browaeys, „Single-atom addressing in microtraps for quantum-state engineering using Rydberg atoms“, *Physical Review A* **90**, 023415 (2014).

Anhang A

Veröffentlichungen

Publikation [1], Seite 29

Measurement of absolute transition frequencies of ^{87}Rb *to nS and nD Rydberg states by means of electromagnetically induced transparency*
M. Mack, **F. Karlewski**, H. Hattermann, S. Höckh, F. Jessen, D. Cano, and J. Fortágh
Physical Review A **83**, 052515 (2011), ©American Physical Society.

Publikation [2], Seite 37

Detrimental adsorbate fields in experiments with cold Rydberg gases near surfaces
H. Hattermann, M. Mack, **F. Karlewski**, F. Jessen, D. Cano, and J. Fortágh
Physical Review A **86**, 022511 (2012), ©American Physical Society.

Publikation [3], Seite 41

Quasiclassical quantum defect theory and the spectrum of highly excited rubidium atoms
A. Sanayei, and N. Schopohl,
J.Grimmel, M. Mack, **F. Karlewski**, and J. Fortágh
Physical Review A **91**, 032509 (2015), ©American Physical Society.

Publikation [4], Seite 47

Measurement and numerical calculation of Rubidium Rydberg Stark spectra
J. Grimmel, M. Mack, **F. Karlewski**, F. Jessen, M. Reinschmidt, N. Sándor, and J. Fortágh
New Journal of Physics **17**, 053005 (2015), ©IOPscience.

Publikation [5], Seite 55

State-selective all-optical detection of Rydberg atoms
F. Karlewski, M. Mack, J. Grimmel, N. Sándor, and J. Fortágh
Physical Review A **91**, 043422 (2015), ©American Physical Society.

Die Nachdrucke auf den folgenden Seiten erfolgen mit Genehmigungen der *American Physical Society* und von *IOPscience*.

Measurement of absolute transition frequencies of ^{87}Rb to nS and nD Rydberg states by means of electromagnetically induced transparency

Markus Mack,* Florian Karlewski, Helge Hattermann, Simone Höckh, Florian Jessen, Daniel Cano, and József Fortágh†
CQ Center for Collective Quantum Phenomena and their Applications, Physikalisches Institut, Eberhard-Karls-Universität Tübingen, Auf der Morgenstelle 14, D-72076 Tübingen, Germany
(Received 23 February 2011; published 23 May 2011)

We report the measurement of absolute excitation frequencies of ^{87}Rb to nS and nD Rydberg states. The Rydberg transition frequencies are obtained by observing electromagnetically induced transparency on a rubidium vapor cell. The accuracy of the measurement of each state is $\lesssim$1 MHz, which is achieved by frequency stabilizing the two diode lasers employed for the spectroscopy to a frequency comb and a frequency comb calibrated wavelength meter, respectively. Based on the spectroscopic data we determine the quantum defects of ^{87}Rb, and compare it with previous measurements on ^{85}Rb. We determine the ionization frequency from the $5S_{1/2}(F = 1)$ ground state of ^{87}Rb to 1010.029 164 6(3) THz, providing the binding energy of the ground state with an accuracy improved by two orders of magnitude.

DOI: 10.1103/PhysRevA.83.052515 PACS number(s): 32.30.−r, 32.80.Rm, 32.80.Ee

I. INTRODUCTION

Rydberg atoms are attracting large research interest as their quantum state can be prepared and controlled with high precision and flexibility by means of electromagnetic fields [1]. Actual research subjects include cavity quantum electrodynamics [2], Rydberg-Rydberg interactions [3] with possible applications in quantum information processing [4], ultracold chemistry [5–7], and sensing dispersion forces between atoms and surfaces [8–10]. Due to their large polarizability, Rydberg atoms respond to static and dynamic electric fields with level shifts and are therefore sensitive to interactions with microscopic and macroscopic objects. For precision measurements of such interactions and accurate quantum state control, it is beneficial to know the unperturbed Rydberg energy levels that we quantify in the present paper for the ^{87}Rb atom, which is widely used in experiments.

In alkali-metal atoms, the deviation from the hydrogen energy structure can be expressed in terms of quantum defects δ [1]. If the quantum defects are known, the energy of Rydberg levels can be calculated with respect to the ionization limit. The quantum defects of the nS and nD lines of ^{85}Rb have been measured by Li *et al.* [11] using microwave excitation between Rydberg states. This method provides superior frequency resolution on the order of ∼10 kHz; however, it does not serve as an absolute frequency reference. If, in addition, absolute transition frequencies between the ground and Rydberg states are known, the binding energy of the ground state can be determined.

Absolute measurements of the nS and nD lines of ^{85}Rb as well as the isotope shift for ^{87}Rb have been done by Stoicheff and Weinberger [12] using two-photon spectroscopy with an accuracy of 100 MHz. Higher accuracy measurements include the nF states of the ^{85}Rb isotope with an accuracy of 8 MHz [13] and on the nS levels of ^{85}Rb with an uncertainty greater than 6 MHz [14]. In the present work, we measure Rydberg transition frequencies of ^{87}Rb with an absolute accuracy of $\lesssim$1 MHz, which results from frequency stabilizing the lasers employed for the spectroscopy to absolute frequency references.

High-resolution spectroscopy of Rydberg states is possible by observing electromagnetically induced transparency (EIT) [15]. The detection of Rydberg states by means of EIT, and the measurement of the fine structure splitting of ^{85}Rb have been reported by Mohapatra *et al.* [16]. In the present work, we implement EIT for measuring the absolute frequency of Rydberg excitations of ^{87}Rb, from which we determine the quantum defects of the nS and nD levels and the ground-state ionization energy of this isotope.

II. EIT LEVEL SCHEME AND EXPERIMENTAL SETUP

The energy-level diagram of ^{87}Rb relevant for this work is shown in Fig. 1. The three-level system consists of the ^{87}Rb $5S_{1/2}(F = 2)$ ground state, the $5P_{3/2}(F = 3)$ intermediate state, and nS or nD Rydberg states with a high principal quantum number n. We observe EIT spectra on a rubidium vapor cell using two counterpropagating laser beams. The frequency of the "probe laser" is fixed at the $5S_{1/2}(F = 2) \leftrightarrow 5P_{3/2}(F = 3)$ transition, which is known to be 384.228 115 2 THz [17] ($\hat{=}$ 780.246 020 9 nm), while the "coupling laser" (≈480 nm) is scanned across the Rydberg resonance. We record EIT spectra by monitoring the probe laser transmission as a function of the coupling laser frequency.

The experimental setup is illustrated in Fig. 2. Absolute frequency measurements are achieved by referencing the probe and coupling laser frequencies to a frequency comb (Menlo Systems, FC 1500).

The source of the probe beam is a grating stabilized diode laser of ∼500 kHz linewidth. The laser is stabilized to 780.246 020 9 nm by superimposing it with the beam of the frequency comb on a fast photodiode and locking the corresponding radio frequency beat signal with the nearest comb mode. The beat signal deviation, and thus the accuracy of the probe laser frequency, was maintained within 500 kHz.

*mack@pit.physik.uni-tuebingen.de
†fortagh@uni-tuebingen.de

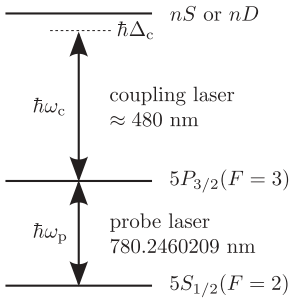

FIG. 1. Energy-level diagram of ^{87}Rb and corresponding laser wavelengths for observation of electromagnetically induced transparency using a Rydberg state. The probe laser is stabilized to the lower atomic resonance, while the coupling laser, with a variable detuning $\hbar\Delta_c$, is scanned across the Rydberg resonance.

The coupling beam at 480 nm is sourced from a frequency-doubled, grating-stabilized diode laser (Toptica, TA SHG Pro) at 960 nm of ∼500 kHz linewidth. In order to access any desired coupling frequency, we stabilize the 960-nm laser to a Fizeau interferometer-based wavelength meter (HighFinesse, WS Ultimate-2). The wavelength meter with a built-in servo feedback unit measures frequency and controls the frequency scans of the coupling laser.

In order to assure the absolute accuracy of the wavelength meter, we perform an automated calibration procedure. A beat signal between the 960-nm laser and a known frequency comb mode is recorded with a digital spectrum analyzer. The beat frequency is determined by software peak recognition and the corresponding laser frequency is used to calibrate the wavelength meter. The resulting accuracy of frequency control by the calibrated wavelength meter was characterized with the frequency comb by exemplary measurements of the frequency offset with respect to the set frequency. We found the frequency offset after calibration approximately to be normally distributed with a standard deviation of 400 kHz.

The experimental sequence for recording EIT spectra on Rydberg levels is as follows. First, the wavelength meter is calibrated using the method described above. Second, a trigger is sent to the wavelength meter, that starts sweeping the coupling laser frequency (at most 12 MHz/s sweeping

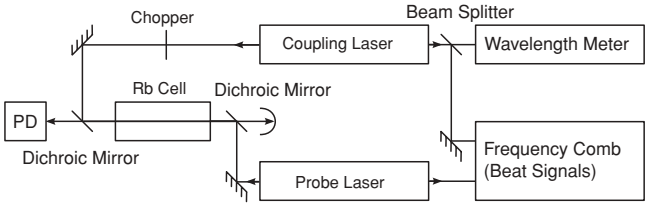

FIG. 2. Optical setup (schematic) for the observation of EIT in a rubidium vapor cell. The probe and coupling beams are counterpropagating in the rubidium vapor cell (heated to ∼45°C) and the probe laser intensity is monitored with a photodiode (PD). A chopper in the coupling laser beam provides a reference signal for lock-in detection of the photodiode signal. The probe laser is frequency stabilized to a frequency comb. The coupling beam at 480 nm comes from a frequency-doubled 960-nm laser that is stabilized and scanned by a wavelength meter. The wavelength meter is calibrated with the help of a frequency comb beat signal at 960 nm.

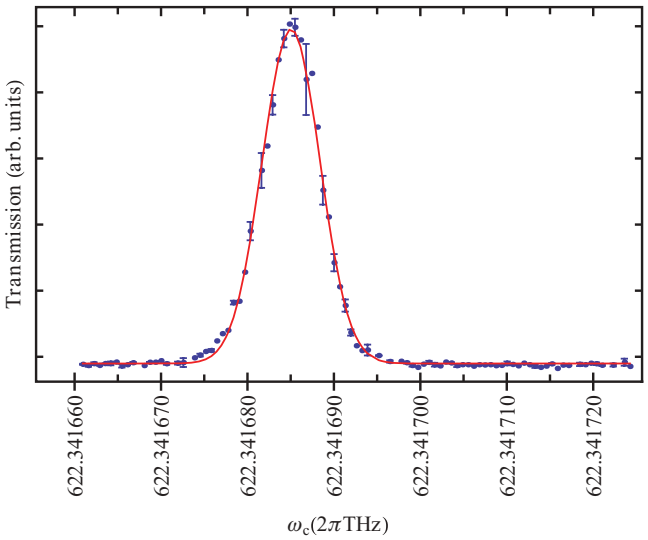

FIG. 3. (Color online) EIT resonance for the $34S_{1/2}$ Rydberg state (exemplary) as recorded by the photodiode, against the coupling laser frequency measured simultaneously by the wavelength meter. A Gaussian shape is fitted for peak frequency determination (solid line).

rate, 30 MHz span at ∼960 nm), while recording the measured coupling laser frequency. The photodiode signal of the probe beam is recorded by a digital storage oscilloscope. If the scan range covers an EIT resonance, a sharp transmission peak is recorded. In order to detect weak EIT signals of high n states, the coupling laser beam is periodically blocked by a chopper wheel at a frequency of about 1 kHz, and the photodiode signal of the probe beam is recorded using a lock-in amplifier synchronized to the chopper. As both the laser frequency and the photodiode signal are recorded simultaneously, we obtain the probe laser transmission as a function of the coupling laser frequency as shown in Fig. 3. The measurement at each EIT resonance is fitted by a Gaussian function to determine the peak position. In order to reduce the statistical error, the measurement sequence is performed five times for each Rydberg level.

III. RYDBERG TRANSITION FREQUENCIES AND MEASUREMENT ACCURACY

Absolute frequencies of transitions $5P_{3/2}(F=3) \rightarrow nS_{1/2}(F=2)$, $5P_{3/2}(F=3) \rightarrow nD_{3/2}$, and $5P_{3/2}(F=3) \rightarrow nD_{5/2}$ of ^{87}Rb were observed for principal quantum numbers n in the range 19–65 (nS states) and 19–57 (nD states). The results are listed in Tables III, IV, and V (Appendix). We note that we were able to observe Rydberg states up to $n = 180$ with the help of the lock-in amplifier. Such highly excited Rydberg states, however, exhibit large linewidths and partially irregular line shapes, thus these are not analyzed in the present manuscript. For quantum defect calculations, we use only the data given in Tables III, IV, and V.

The uncertainty of the frequency data comprise several known error sources of physical and technical nature. The main error source arises from the frequency stabilization of the probe laser with an uncertainty of 500 kHz (see Sec. II).

A frequency deviation Δ_p from the atomic resonance ω_p leads to the excitation of atoms with a velocity of $v = c\frac{\Delta_p}{\omega_p}$. If Δ_p is small compared to the Doppler broadening, the EIT transmission peak appears at a coupling laser frequency shifted by $\Delta_c = \frac{v}{c}\omega_c = (\omega_c/\omega_p)\Delta_p$ with respect to the resonance frequency ω_c. Consequently, the uncertainty of the probe laser frequency translates into an uncertainty of (780 nm/480 nm) × 500 kHz ≈ 800 kHz of the EIT peak position measured with the coupling laser.

The uncertainty of the coupling laser frequency enters the EIT peak determination with 200 kHz. This is less than the uncertainty of the frequency stabilization of this laser (400 kHz) because of the fivefold repetition of the frequency measurement (including calibration).

In our setup, the frequency of the comb modes can be determined with an absolute accuracy on the order of 10 kHz. This uncertainty is negligible with respect to other sources of error. The high accuracy of the frequency comb is achieved by a 10 MHz GPS disciplined rubidium frequency reference (Precision Test Systems, GPS10RBN) with a specified Allan deviation of 2×10^{-11} at 1 s observation time. The accuracy of the transfer of the rf reference frequency to optical frequencies was determined by Kubina *et al.* [18], who compared two similar frequency combs referenced to one common rf frequency standard, finding the optical frequencies that were measured with both combs to agree to a level of 6×10^{-16}.

The width of the observed EIT resonances is typically $\lesssim$10 MHz. The linewidth of the lasers, technical noise, triggering precision, and physical deviations from the Gaussian line shape that has been used for finding the peak position contribute to the uncertainty of the measured resonance frequency as well. The overall uncertainty resulting from these effects was determined independently for each transition and was typically less than 300 kHz.

Despite the strong n^7 dependence of the polarizability [1], line shifts due to stray electric fields are not present in the vapor cell due to screening by ions and electrons on the inner surface of the glass cell [16]. We verified the screening in our setup for field strengths up to 470 V/cm and on Rydberg states up to $n = 150$. We observed line broadening due to external magnetic fields, which are in our setup on the order of the earth magnetic field, but no significant line shift or asymmetry of the resonance peak. Pressure shifts at a cell temperature of $\lesssim$45°C are calculated to be less than 200 kHz [19].

IV. QUANTUM DEFECTS AND IONIZATION ENERGY

The energies of Rydberg levels [1] are given by

$$E_{n,l,j} = E_{\mathrm{i}} - \frac{\mathcal{R}^*}{[n - \delta(n,l,j)]^2}, \tag{1}$$

where E_i is the ionization energy threshold and

$$\mathcal{R}^* = \frac{1}{1 + \frac{m_e}{m_{^{87}\mathrm{Rb}}}}\mathcal{R}_\infty = h \cdot 3289.821\,194\,66(2)\,\mathrm{THz}$$

is the Rydberg constant, corrected for the reduced electron mass in ^{87}Rb.

For sufficiently large principal quantum numbers n, the quantum defects $\delta(n,l,j)$ depend only little on n and can be approximated by the modified Rydberg-Ritz parameters

$$\delta(n,l,j) \approx \delta_0 + \frac{\delta_2}{(n - \delta_0)^2}. \tag{2}$$

Within the accuracy of our measurements on $n \geqslant 19$ Rydberg states, the inclusion of higher-order terms in the approximation did not lead to improved results.

A precise measurement of the modified Rydberg-Ritz parameters for the nS, nP, and nD series of ^{85}Rb was performed by Li *et al.* [11]. By exciting microwave transitions between Rydberg levels ($n = 32$ up to 37) and subsequent detection by field ionization, the transition frequencies were determined with a resolution of up to 10 kHz. The "average" quantum defects $\delta(n,n+1)$ determined by this measurement were used to improve the value of quantum defects previously obtained by Lorenzen and Niemax [20].

Traditionally, the quantum defects are determined for the fine structure levels. The hyperfine splitting is negligible for nD states but not for nS states because of a nonzero probability amplitude at the position of the nucleus. In our measurements of nS states, only transitions to $F = 2$ states were observed because of selection rules. In order to obtain quantum defects for the fine structure, we need to consider the hyperfine shifts in the evaluation of our data.

The hyperfine splitting of states between $n = 28$ and 33 of both ^{85}Rb and ^{87}Rb was determined by Li *et al.* [11]. Using their data, we extrapolate the hyperfine splitting between the $nS_{1/2}(F = 1)$ and $(F = 2)$ states of ^{87}Rb according to a n^{*-3} law $n^* := n - \delta(n,l,j)$ as

$$\Delta_{\mathrm{HFS},F=2} - \Delta_{\mathrm{HFS},F=1} = 33.5(9)\ \mathrm{GHz} \times n^{*-3}.$$

In general, the hyperfine shift is given by $\Delta_{\mathrm{HFS},F} = \frac{A}{2}[F(F+1) - I(I+1) - J(J+1)]$, which, compared with the measurement, yields the value of the hyperfine constant A. For the $J = 1/2$ states of ^{87}Rb (nuclear spin $I = 3/2$), the hyperfine splitting is $\Delta_{\mathrm{HFS},F=2} - \Delta_{\mathrm{HFS},F=1} = 2A$.

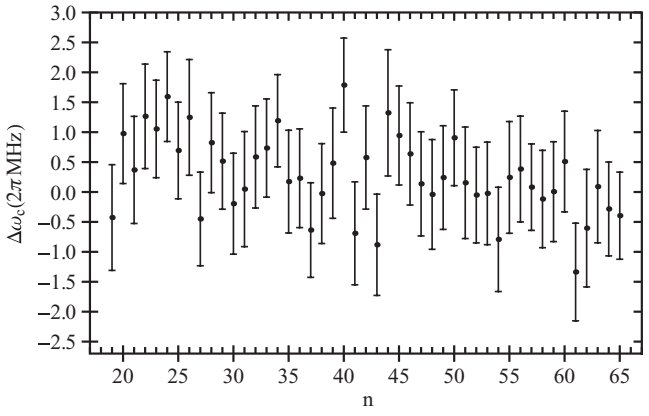

FIG. 4. Difference between measured transition frequencies to $nS_{1/2}$ Rydberg states (see Table III) and the transition frequencies calculated with Eq. (1) based on the Rydberg-Ritz parameters and ionization frequency specified in Tables I and II.

Extending the extrapolation with the n^{*-3} law for the states $n \geqslant 28$ to $n = 19$ leads to a systematical error in the determination of A. In order to quantify this error we extrapolate further down to $n = 11$, for which the hyperfine splitting is known from a measurement by Farley *et al.* [21]. We find 10% deviation between the calculated ($A_{11S_{1/2}} = 34.5$ MHz) and the measured $A_{11S_{1/2}} = 37.4(3)$ MHz value, which gives an upper limit of the systematic error for $n > 11$ states.

We now can compute the hyperfine shift of the $nS_{1/2}(F = 2)$ states that have been measured in this work,

$$\Delta_{\mathrm{HFS},F=2} = \frac{3}{4}A = \frac{3}{2\times 4} \times 34(3)\ \mathrm{GHz} \times n^{*-3},$$

and subtract these frequency shifts from the measured transition frequencies to the $nS_{1/2}(F = 2)$ states to find the quantum defects with respect to the fine structure levels. For the lowest nS state measured in this work, $n = 19$, the hyperfine shift is $\Delta_{\mathrm{HFS},F=2} = 3.2(3)$ MHz.

In order to determine the modified Rydberg-Ritz parameters, Eq. (1) is simultaneously fitted to all three data series ($nS_{1/2}$, $nD_{3/2}$, and $nD_{5/2}$), with the ionization frequency $\omega_{\mathrm{i}} = E_{\mathrm{i}}/\hbar$ as a common fit parameter. The difference between the measured frequencies and the corresponding values obtained by the fit (residuals) are shown in Fig. 4 exemplary for the measurement series on the $nS_{1/2}$ lines. The residuals vary around zero with an rms deviation of $\lesssim$0.75 MHz, which applies to all three data series, consistent with the expected overall precision of the experimental setup.

The resulting values for the modified Rydberg-Ritz parameters are shown in Table I along the values determined by Li *et al.* [11] for ^{85}Rb. The parameters for the nS series of ^{85}Rb [11] and ^{87}Rb (this work) match each other with comparable uncertainties. Omitting the hyperfine structure correction, the fit of our data returns a slightly different value of $\delta_0 = 3.131\,178\,8(8)$ (with no difference in δ_2) that gives the value of the quantum defect of the $nS_{1/2}(F = 2)$ hyperfine levels.

The values of δ_0 of the nD series show a deviation from the values of Li *et al.* of about 3 times the stated uncertainty. Nonetheless, comparing the frequency differences measured in this work ($\omega_{c,n+1} - \omega_{c,n}$) with the Rydberg-Rydberg transition frequencies $\omega_{n,n+1}$ measured by Li *et al.*, we find that the values available in both data sets are well within one standard deviation ($nS_{1/2}$ and $nD_{5/2}$) or at most just outside one standard deviation ($nD_{3/2}$). We therefore suspect differences in the analysis as well as the range of included n values to be the reason for the discrepancy.

TABLE I. Modified Rydberg-Ritz parameters δ_0 and δ_2 of the nS and nD lines of ^{85}Rb following [11] and of ^{87}Rb as determined in this work. nS quantum defects refer to the fine structure levels, corrected for shifts due to hyperfine structure.

		^{85}Rb (Li *et al.* [11])	^{87}Rb (this work)
$nS_{1/2}$	δ_0	3.131 180 4(10)	3.131 180 7(8)
	δ_2	0.178 4(6)	0.178 7(2)
$nD_{3/2}$	δ_0	1.348 091 7(4)	1.348 094 8(11)
	δ_2	−0.602 9(3)	−0.605 4(4)
$nD_{5/2}$	δ_0	1.346 465 7(3)	1.346 462 2(11)
	δ_2	−0.596 0(2)	−0.594 0(4)

TABLE II. Ionization frequency from the $5P_{3/2}(F = 3)$ state (fit result including systematic error) and the $5S_{1/2}(F = 1)$ ground state (calculated on basis of the fit result) of ^{87}Rb as determined in this work and compared with the value given by Stoicheff and Weinberger [12].

	Stoicheff and Weinberger [12]	This work
$E_{\mathrm{i},5P_{3/2}(F=3)}/h$	—	625.794 214 8(3) THz
$E_{\mathrm{i},5S_{1/2}(F=1)}/(hc)$	33 690.945 5(15) cm^{-1}	33 690.946 44(1) cm^{-1}
$E_{\mathrm{i},5S_{1/2}(F=1)}/h$	1 010.029 14(5) THz	1 010.029 164 6(3) THz

The value of the ground-state ionization energy (i.e., the binding energy of the ground state), as obtained by fitting Eq. (1) to the experimental data, is given in Table II. Because all measured Rydberg transition frequencies enter into this value, its statistical error is small (90 kHz) and systematic uncertainties like pressure shifts become significant. We estimate systematic shifts to be on the order of 200 kHz, resulting in $\lesssim$300 kHz uncertainty of the ground-state ionization energy. The ground-state ionization energy found in this work is within the uncertainty stated by Stoicheff and Weinberger [12] and is two orders of magnitude more accurate.

V. CONCLUSIONS

In summary, we performed precision spectroscopy of Rydberg states of ^{87}Rb using diode lasers, frequency stabilized to a frequency comb and a calibrated wavelength meter. This allows for absolute frequency measurements with an uncertainty of $\lesssim$1 MHz. The system presented in this work combines the ease of use of the wavelength meter with the accuracy of the frequency comb, enabling absolute frequency measurements over a wide frequency range, not limited by the availability of atomic lines to serve as an absolute reference.

We determined quantum defects and the ionization energy of ^{87}Rb with an uncertainty of $\lesssim$300 kHz. In the future, the precision of such measurements can be improved further by reducing the laser linewidths and increasing the bandwidth of the frequency locks.

ACKNOWLEDGMENTS

The authors acknowledge financial support by the BMBF (NanoFutur 03X5506), the European Research Council (ERC Advanced Research Grant "SOCATHES"), and the Strukturfonds of the University of Tübingen. The authors thank the company HighFinesse for technical support.

APPENDIX: RYDBERG TRANSITION FREQUENCIES

1. $nS_{1/2}$

TABLE III. Measured absolute transition frequencies (ω_c) between the $5P_{3/2}(F = 3)$ state and $nS_{1/2}(F = 2)$ Rydberg states of ^{87}Rb. The quantum defects δ include the correction for hyperfine structure. $\Delta\omega_c$ is the difference between the measured transition frequency and the frequency calculated with Eq. (1) using the quantum defects and ionization energy determined in this work.

n	ω_c (2π THz)	δ	$\Delta\omega_c$ (2π MHz)
19	612.7288381(8)	3.1318908(5)	−0.8
20	614.2321542(8)	3.1318083(6)	0.5
21	615.4901687(8)	3.1317405(7)	−0.2
22	616.5534925(8)	3.1316819(8)	0.7
23	617.4603214(8)	3.1316328(10)	0.5
24	618.2399264(8)	3.1315896(11)	1.0
25	618.9150382(8)	3.1315541(13)	0.2
26	619.5035327(8)	3.131521(2)	0.7
27	620.0196148(8)	3.131496(2)	−1.0
28	620.4746999(8)	3.131469(2)	0.3
29	620.8780318(8)	3.131448(2)	0.0
30	621.2371711(8)	3.131430(2)	−0.6
31	621.5583473(8)	3.131412(3)	−0.4
32	621.8467280(8)	3.131395(3)	0.2
33	622.1066304(8)	3.131380(3)	0.3
34	622.3416850(8)	3.131365(4)	0.8
35	622.5549595(8)	3.131358(4)	−0.2
36	622.7490663(8)	3.131347(4)	−0.1
37	622.9262334(8)	3.131342(5)	−1.0
38	623.0883784(8)	3.131330(5)	−0.4
39	623.2371515(8)	3.131319(6)	0.1
40	623.3739846(8)	3.131301(6)	1.4
41	623.5001176(8)	3.131314(7)	−1.0
42	623.6166445(8)	3.131297(7)	0.3
43	623.7245107(8)	3.131305(8)	−1.2
44	623.8245598(9)	3.131277(9)	1.0
45	623.9175235(8)	3.131275(9)	0.6
46	624.0040577(8)	3.131274(10)	0.3
47	624.0847416(8)	3.131276(11)	−0.2
48	624.1600915(8)	3.131274(11)	−0.3
49	624.2305675(8)	3.131266(12)	−0.0
50	624.2965811(8)	3.131252(13)	0.6
51	624.3584995(8)	3.131261(14)	−0.1
52	624.4166563(8)	3.131261(14)	−0.3
53	624.4713499(8)	3.13126(2)	−0.3
54	624.5228490(8)	3.13127(2)	−1.1
55	624.5714000(8)	3.13125(2)	−0.0
56	624.6172212(8)	3.13124(2)	0.1
57	624.6605140(8)	3.13125(2)	−0.2
58	624.7014614(8)	3.13125(2)	−0.4
59	624.7402301(8)	3.13124(2)	−0.3
60	624.7769720(8)	3.13123(2)	0.3
61	624.8118234(8)	3.13128(2)	−1.6
62	624.8449163(8)	3.13126(3)	−0.9
63	624.8763648(8)	3.13124(3)	−0.2
64	624.9062750(8)	3.13125(3)	−0.5
65	624.9347470(8)	3.13125(3)	−0.6

2. $nD_{3/2}$

TABLE IV: Measured Rydberg transition frequencies $5P_{3/2}(F = 3) \rightarrow nD_{3/2}$ of ^{87}Rb. See description of Table III.

n	ω_c (2π THz)	δ	$\Delta\omega_c$ (2π MHz)
19	615.2383571(8)	1.3461520(7)	−0.1
20	616.3395780(8)	1.3463543(8)	0.3
21	617.2770769(8)	1.3465269(10)	0.3
22	618.0817641(8)	1.3466765(11)	−0.9
23	618.7775900(8)	1.3468033(13)	0.1
24	619.3833361(8)	1.3469144(14)	0.3
25	619.9139034(8)	1.347013(2)	−0.4
26	620.3812369(8)	1.347100(2)	−0.4
27	620.7949991(8)	1.347174(2)	0.2
28	621.1630743(8)	1.347241(2)	0.5
29	621.4919489(8)	1.347301(3)	0.6
30	621.7869975(8)	1.347356(3)	0.3
31	622.0527045(8)	1.347407(3)	−0.2
32	622.2928357(8)	1.347452(4)	−0.3
33	622.5105718(8)	1.347488(4)	0.6
34	622.7086101(8)	1.347533(4)	−1.1
35	622.8892621(8)	1.347556(5)	0.8
37	623.2060305(8)	1.347618(6)	0.1
38	623.3453297(8)	1.347640(6)	0.6
39	623.4736776(8)	1.347668(7)	−0.0
40	623.5921942(8)	1.347689(7)	0.1
41	623.7018578(8)	1.347711(8)	−0.1
42	623.8035293(8)	1.347727(8)	0.1
43	623.8979667(8)	1.347740(9)	0.5
44	623.9858378(8)	1.347778(10)	−1.4
45	624.0677426(8)	1.347778(10)	−0.1
46	624.1442056(8)	1.347789(11)	0.2
47	624.2156986(8)	1.347808(12)	−0.3
48	624.2826438(8)	1.347827(13)	−0.7
51	624.4597844(8)	1.34784(2)	0.7
53	624.5611212(8)	1.34788(2)	−0.7
54	624.6075157(8)	1.34788(2)	−0.2
55	624.6513410(8)	1.34786(2)	0.9
57	624.7320082(8)	1.34789(2)	0.4

3. $nD_{5/2}$

TABLE V: Measured Rydberg transition frequencies $5P_{3/2}(F = 3) \rightarrow nD_{5/2}$ of ^{87}Rb. See description of Table III.

n	ω_c (2π THz)	δ	$\Delta\omega_c$ (2π MHz)
19	615.2402660(8)	1.3445555(7)	0.6
20	616.3411990(8)	1.3447550(8)	−0.1
21	617.2784664(8)	1.3449236(9)	0.6
22	618.0829639(8)	1.3450698(11)	−0.2
23	618.7786314(8)	1.3451963(13)	−0.7
24	619.3842463(8)	1.3453060(15)	−0.8
25	619.9147046(8)	1.345402(2)	−0.7
26	620.3819464(8)	1.345484(2)	0.5
27	620.7956283(8)	1.345560(2)	−0.2
28	621.1636344(8)	1.345629(2)	−1.1
29	621.4924518(8)	1.345685(3)	0.2
30	621.7874500(8)	1.345738(3)	0.1
31	622.0531143(8)	1.345783(3)	1.0
32	622.2932066(8)	1.345828(4)	0.4
33	622.5109082(8)	1.345866(4)	0.6
34	622.7089185(8)	1.345901(4)	0.8
35	622.8895425(8)	1.345931(5)	1.2
37	623.2062666(8)	1.345992(6)	0.5
38	623.3455461(8)	1.346020(6)	−0.0
39	623.4738779(8)	1.346042(7)	0.1
40	623.5923802(8)	1.346057(7)	0.9
41	623.7020295(8)	1.346084(8)	0.0
42	623.8036883(8)	1.346104(8)	−0.1
43	623.8981149(8)	1.346112(9)	0.7
44	623.9859786(8)	1.346118(10)	1.5
45	624.0678704(8)	1.346162(10)	−0.9
46	624.1443264(8)	1.346155(11)	0.7
48	624.2827502(8)	1.346185(13)	0.3
51	624.4598714(8)	1.34622(2)	0.3
53	624.5611995(8)	1.34624(2)	−0.2
54	624.6075890(8)	1.34626(2)	−0.4
55	624.6514104(8)	1.34623(2)	0.9
57	624.7320704(8)	1.34626(2)	0.5

[1] T. F. Gallagher, *Rydberg Atoms* (Cambridge University Press, Cambridge, UK, 1994).

[2] J. M. Raimond, M. Brune, and S. Haroche, Rev. Mod. Phys. **73**, 565 (2001).

[3] D. Comparat and P. Pillet, J. Opt. Soc. Am. B **27**, A208 (2010).

[4] M. Saffman, T. G. Walker, and K. Mølmer, Rev. Mod. Phys. **82**, 2313 (2010).

[5] C. H. Greene, A. S. Dickinson, and H. R. Sadeghpour, Phys. Rev. Lett. **85**, 2458 (2000).

[6] C. Boisseau, I. Simbotin, and R. Côté, Phys. Rev. Lett. **88**, 133004 (2002).

[7] V. Bendkowsky, B. Butscher, J. Nipper, J. P. Shaffer, R. Löw, and T. Pfau, Nature (London) **458**, 1005 (2009).

[8] H. Kübler, J. Shaffer, T. Baluktsian, R. Löw, and T. Pfau, Nat. Photon. **4**, 112 (2010).

[9] J. A. Crosse, S. A. Ellingsen, K. Clements, S. Y. Buhmann, and S. Scheel, Phys. Rev. A **82**, 010901 (2010).

[10] A. Tauschinsky, R. M. T. Thijssen, S. Whitlock, H. B. van Linden van den Heuvell, and R. J. C. Spreeuw, Phys. Rev. A **81**, 063411 (2010).

[11] W. Li, I. Mourachko, M. W. Noel, and T. Gallagher, Phys. Rev. A **67**, 052502 (2003).

[12] B. P. Stoicheff and E. Weinberger, Can. J. Phys. **57**, 2143 (1979).

[13] L. A. M. Johnson, H. O. Majeed, B. Sanguinetti, T. Becker, and B. T. H. Varcoe, New J. Phys. **12**, 063028 (2010).

[14] C. Sansonetti and K. Weber, J. Opt. Soc. Am. B **2**, 1385 (1985).

[15] M. Fleischhauer, A. Imamoglu, and J. P. Marangos, Rev. Mod. Phys. **77**, 633 (2005).

[16] A. K. Mohapatra, T. R. Jackson, and C. S. Adams, Phys. Rev. Lett. **98**, 113003 (2007).

[17] J. Ye, S. Swartz, P. Jungner, and J. Hall, Opt. Lett. **21**, 1280 (1996).
[18] P. Kubina, P. Adel, F. Adler, G. Grosche, T. Hänsch, R. Holzwarth, A. Leitenstorfer, B. Lipphardt, and H. Schnatz, Opt. Express **13**, 904 (2005).
[19] D. C. Thompson, E. Weinberger, G.-X. Xu, and B. P. Stoicheff, Phys. Rev. A **35**, 690 (1987).
[20] C. J. Lorenzen and K. Niemax, Phys. Scr. **27**, 300 (1983).
[21] J. Farley, P. Tsekeris, and R. Gupta, Phys. Rev. A **15**, 1530 (1977).

PHYSICAL REVIEW A **86**, 022511 (2012)

Detrimental adsorbate fields in experiments with cold Rydberg gases near surfaces

H. Hattermann,* M. Mack, F. Karlewski, F. Jessen, D. Cano, and J. Fortágh†
CQ Center for Collective Quantum Phenomena and their Applications, Physikalisches Institut, Eberhard-Karls-Universität Tübingen, Auf der Morgenstelle 14, D-72076 Tübingen, Germany
(Received 4 June 2012; published 17 August 2012)

We observe the shift of Rydberg levels of rubidium close to a copper surface when atomic clouds are repeatedly deposited on it. We measure transition frequencies of rubidium to S and D Rydberg states with principal quantum numbers n between 31 and 48 using the technique of electromagnetically induced transparency. The spectroscopic measurement shows a strong increase of electric fields towards the surface that evolves with the deposition of atoms. Starting with a clean surface, we measure the evolution of electrostatic fields in the range between 30 and 300 μm from the surface. We find that after the deposition of a few hundred atomic clouds, each containing $\sim 10^6$ atoms, the field of adsorbates reaches 1 V/cm for a distance of 30 μm from the surface. This evolution of the electrostatic field sets serious limitations on cavity QED experiments proposed for Rydberg atoms on atom chips.

DOI: 10.1103/PhysRevA.86.022511 PACS number(s): 32.30.−r, 32.80.Rm, 68.43.−h

I. RYDBERG ATOMS AT SURFACES

The large electric polarizability of Rydberg atoms leads to a large response to electric fields [1]. This property is an enormous advantage for applications that require fast coupling between atoms and photons, such as the entanglement of Rydberg atoms via the electromagnetic modes of radio-frequency and microwave cavities [2]. Several quantum computation schemes have been proposed based on Rydberg atoms coupled to superconducting coplanar cavities [3–5]. In the proposed scenarios, cold atomic gases are first positioned near a coplanar resonator. The atoms are subsequently laser excited into Rydberg states which interact with the electromagnetic modes of the resonator. Recent progress with coupling such cavities to superconducting qubits [6,7] and the coupling of Rydberg atoms to a microwave stripline [8] outline good perspectives.

However, the technical realization faces challenges. One significant problem is the detrimental effect of the electrostatic fields generated by adsorbed atoms on the chip surface. Because of the high electronegativity of metals, atoms deposited on the chip surface partially donate their valence electron to the metal. The result is a permanent electric dipole layer on the surface that produces inhomogeneous electrostatic fields and alters both the energy and the orbital structure of nearby Rydberg atoms. The fields can be strong enough to shift Rydberg states out of the cavity resonance.

New chips are initially free of adsorbates, but experiments progressively accumulate adatoms on the surface. An important question is how long it takes until the accumulation of atoms on the surface becomes detrimental. Two research groups reported previously on this subject. First, McGuirk *et al*. [9] and Obrecht *et al*. [10] studied the electrostatic field of adsorbed atoms on both conducting and insulating surfaces. Second, Tauschinsky *et al*. [11] measured electrostatic fields of adsorbates using electromagnetically induced transparency (EIT) on Rydberg states. The results presented in this article complement the data published by these two groups. We measure the evolution of electrostatic fields at distances of 30–300 μm to the surface during a series of consecutive experiments. Starting with a clean copper surface we deposit clouds of ^{87}Rb atoms onto the surface and measure the inhomogeneous electrostatic field of polarized adatoms by spectroscopy on Rydberg states. We find that the electrostatic fields are already significant after about a few hundred experimental cycles. This corresponds to only a few hours of operation for a typical cold atom experiment.

II. MEASUREMENT OF THE ELECTROSTATIC FIELDS OF ADSORBATES BY RYDBERG EIT

We measure the electrostatic field of adsorbed and polarized adatoms through the energy shift (dc Stark shift) induced on highly excited Rydberg states of rubidium. We start our experiments with a clean copper surface which is horizontally aligned inside a vacuum chamber [Fig. 1(a)] at a base pressure of 10^{-11} mbar. We transport ultracold clouds of ^{87}Rb ($T = 1.5$ μK) with optical tweezers to a position 200 μm above the surface and release the atomic cloud. About $\sim 10^6$ atoms are dropped in each experimental cycle onto the surface. While the atomic cloud is falling towards the surface, we measure its EIT spectra.

The ladder-type excitation scheme used for the EIT measurements [13,14] is shown in Fig. 1(b). We probe the absorption on the $5S$-$5P$ transition with a weak probe laser. The $5P$ state is strongly coupled to a highly excited nS or nD Rydberg state by means of a 480-nm laser. While the frequency of the probe laser is stabilized to the $5S$-$5P$ transition, the coupling laser can be continuously scanned within a wide range of frequencies ($\pm$50 MHz). Whenever the coupling laser is on resonance with a Rydberg state, the conditions for EIT are satisfied and the atomic ensemble becomes transparent for the probe laser [15]. The presence of adsorbed atoms on the surface perturbs the Rydberg states and the resonance conditions for the coupling laser. We observe pronounced energy shifts towards the surface which increase with the deposition of atomic clouds. For the measurements we use S and D Rydberg states with principal quantum numbers n between 31 and 48.

*hattermann@pit.physik.uni-tuebingen.de
†fortagh@uni-tuebingen.de

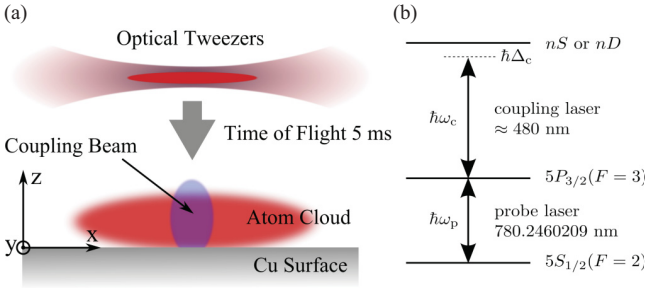

FIG. 1. (Color online) (a) An atomic cloud (10^6 ^{87}Rb atoms in the $5S_{1/2}$ ($F = 2, m_F = 2$) ground state at temperature 1.5 μK) is released from an optical dipole trap to free fall and expand. The cloud hits a Cu surface 200 μm below the trap. The electric field of polarized adatoms is tested by means of Rydberg EIT. While the probe beam illuminates the full area, the coupling beam has a smaller, elliptical spot size, illustrated in blue. (b) Ladder configuration for EIT signals. The probe beam couples the $5S_{1/2}$ ($F = 2, m_F = 2$) and the $5P_{3/2}$ ($F = 3, m_F = 3$) levels. Simultaneously, a counterpropagating coupling beam focused onto a part of the cloud (blue spot) is switched on. The lasers are referenced to a frequency comb. In Ref. [12] we describe the details of the locking method.

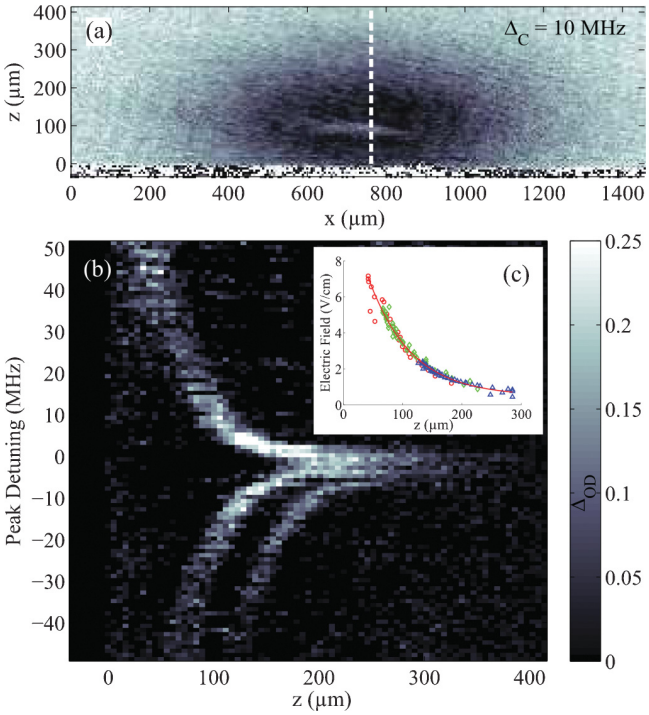

FIG. 2. (Color online) (a) Absorption image of an atomic cloud during free fall onto the surface taken with the probe beam. The stronger the absorption, the darker the pixel in the image. In this example, the coupling laser is blue detuned by 10 MHz from the $35D_{5/2}$ state of ^{87}Rb and produces a transparency window. The lateral extension of the window is given here by the width of the coupling laser beam. For the data analysis we take the z position of the transparency window along the vertical dashed line. Similar images have been taken for detunings ranging from −50 to +50 MHz, allowing the measurement of electrostatic fields as a function of z. (b) Map of the relative optical density as a function of distance to the surface (horizontal axis) and detuning of the coupling laser from the unperturbed transition frequency $5P_{3/2}$ ($F = 3$, m_F=3) → $35D_{5/2}$ (vertical axis). Each horizontal line shows a single measurement. (c) Calculated electrostatic field as function of z using the EIT measurements on the $35D_{5/2}$ state. The different colors are the field strengths obtained using the $|m_J| = 1/2$ (red circles), 3/2 (green diamonds), and 5/2 states (blue triangles). The data of the three states follow the same curve, which is well approximated by an exponential decay.

For our experiments we prepare clouds of ^{87}Rb atoms in the $5S_{1/2}$ ($F = 2, m_F = 2$) state in a setup described in Ref. [16]. The atomic cloud is loaded from a magneto-optical trap (MOT) into a Ioffe-Pritchard type magnetic trap and cooled by forced radio-frequency evaporation to a temperature of 1.5 μK. The cloud with about 10^6 atoms is then loaded into an optical dipole potential of a focused 1064-nm laser beam. By moving the focusing lens with an air bearing translation stage, the optical tweezers transport the atoms from the preparation zone over a distance of 35 mm to a position above a copper surface. The tweezers are micropositioned 200 μm above the surface and the atomic cloud is released by instantly ramping down the laser power. After 5 ms of free fall and expansion, the atomic cloud is imaged by absorption imaging. As the cloud falls, EIT spectra of the atoms are taken. The imaging beam (probe beam for the EIT) has a Gaussian profile of 7.5 mm full width at half maximum (FWHM) and ∼100 μW power. The counterpropagating coupling beam is simultaneously focused onto the cloud. It has an elliptical profile with ∼200 and 300 μm FWHM, respectively. The frequency stabilization of the lasers with an absolute accuracy of better than ±1.5 MHz is described in Ref. [12].

The measurements are illustrated in Fig. 2(a). The absorption image of an atomic cloud during free fall shows a "transparency window" at the positions where the coupling laser is resonant with the transition, in this case the $35D_{5/2}$ ($m_J = 1/2$) state. The image shows that the resonance condition is satisfied only in a small window revealing a spatial inhomogeneity of the energy shift. In this window the shift of the Rydberg level equals the detuning Δ_C of the coupling laser, in this example +10 MHz with respect to the unperturbed transition frequency. If the detuning of the coupling laser is changed, the transparency window appears at a different distance from the surface.

We take a series of absorption images as a function of the detuning Δ_C. The laser frequency is varied in steps of 1 MHz between consecutive measurements. The results are summarized in Fig. 2(b), which shows the Stark shift of Rydberg states as a function of the distance z to the surface. Each horizontal line of Fig. 2(b) is obtained from the vertical column of absorption images, as indicated by the vertical dashed line in Fig. 2(a). Thus it shows the position of the transparency window for different detunings. The three branches in Fig. 2(b) correspond to the projections of the total angular momentum J of the $35D_{5/2}$ Rydberg state: $|m_J| = 1/2, 3/2$, and $5/2$.

We now determine the electrostatic field above the copper surface by using the measured Stark shifts and comparing them with the theoretically calculated shift of Rydberg levels in electrostatic fields. We calculate the Stark maps with the numerical method of Ref. [17]. For our evaluation, we use

an algorithm which identifies the electrostatic fields that best fit the measured data. As shown in Fig. 2(c), the results for the three different $|m_J|$ states lie on the same curve, confirming the validity of our procedure. The shifts of the Rydberg states are thus explained by static electric fields alone. The decay of the electrostatic field is modeled here with an exponential function: $E(z) = E_0 \exp(-z/\sigma) + E_{\text{res}}$, where z is the distance to the surface, σ is the decay length, and E_{res} is a residual, homogeneous electrostatic field that accounts for possible external field sources. Figure 2(c) shows the best-fit fields calculated with the three experimental curves of Fig. 2(b). We repeated our measurements on S and D Rydberg states with principal quantum numbers n between 31 and 48 that reproduce the same behavior. For distances smaller than 30 μm, the electrostatic field cannot be determined reliably, as high field gradients over the size of one pixel of the camera (5.6 μm in the object plane) lead to blurring of the measured line shifts. We note that the electric field is also inhomogeneous along the x axis. This is a result of the Gaussian distribution of the atomic clouds dropped onto the surface and of the residual roughness of the copper. In order to facilitate the evaluation of the changes of the field with time, all the measurements have been evaluated along the same line, as indicated in Fig. 2(a).

III. TEMPORAL EVOLUTION OF THE ELECTROSTATIC FIELDS OF DEPOSITED ADATOMS

We evaluate the evolution of the electrostatic field close to the surface as atom clouds are repeatedly deposited on it. Figure 3 summarizes the results. The diagram shows the electric field as a function of the distance from the surface and the number of deposited atomic clouds. Different colors correspond to different strengths of the electric field. The red (solid) lines are exponential fits that we use for determining the electric field as in Sec. II. The inset shows the increase of the measured electric field with the number of deposited atoms

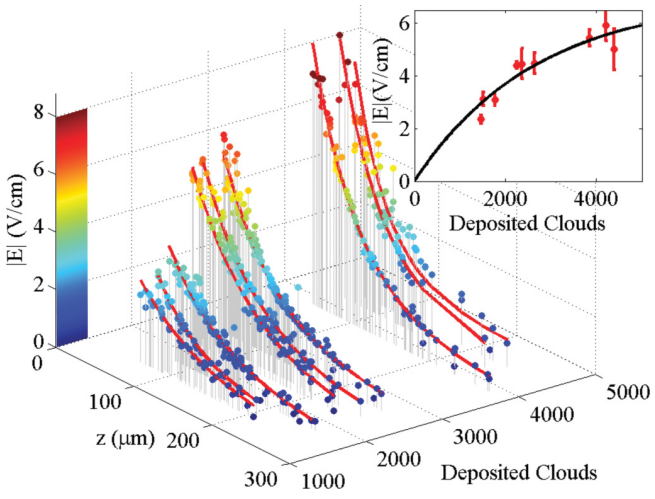

FIG. 3. (Color online) Measured electrostatic field as a function of z and the number of experimental cycles carried out. Inset: Measured electrostatic field at a distance of 80 μm from the surface. We observe an increase of the electric field due to adsorption of rubidium onto the copper surface. The saturation builds up after the deposition of few thousand atomic clouds.

for a distance of 80 μm from the surface. The magnitude of the field increases with the number of experimental runs. However, we observe a saturation after about ten days of experiments during which we released approximately 5×10^9 atoms on the copper surface. Based on our measurements, we estimate that it takes as little as few hundred experimental runs to produce an electric field of 1 V/cm at a distance of 30 μm, assuming a zero-field at the beginning of the experiments. This field produces a level shift of -2 MHz on the $35S_{1/2}$ state and of -49 MHz on the $55S_{1/2}$ state. This is much larger than the linewidth of a high-Q stripline resonator, making cavity QED experiments problematic by shifting the atoms out of the cavity resonance.

IV. CONCLUSION

Our measurements show that neutral atoms adsorbed on a metal surface cause electrostatic fields on the order of 1 V/cm after as little as 100 repetitions of a cold atom experimental cycle. Adsorbate fields have also been observed on dielectric surfaces [18]. This sets serious limitations on the feasibility of cavity QED experiments with Rydberg atoms and coplanar cavities. Also dispersion forces between Rydberg atoms and planar surfaces [19] are masked by the strong electric fields of adsorbates. A search for strategies to correct for this problem is therefore very important for atom chips. A possible solution could be the cleaning of the surface whenever the electrostatic fields due to adsorbates become harmful. For example, regular heating of the surface cause adsorbed atoms to diffuse. Another possibility would be photodissorption of the adsorbed atoms, but given the work function of metals, this would require light in the far ultraviolet range. Given the fast appearance of detrimental adsorbate fields, an open question is still if there are cleaning techniques which can be applied quickly between experimental cycles. A workaround for this problem would be the development of experimental techniques that avoid deposition of atoms onto the surface or using surface coatings with materials on which no adsorbate fields have been observed [14]. While atoms on surfaces have undesired effects on cold atom experiments, it is worth mentioning that adatoms may be useful to control electric properties of surface layers. For example, alkali-metal adsorbates have been used to engineer the electronic structure of graphene [20,21].

Rydberg EIT can be used for a sensitive measurement of electric fields. In combination with micropositioning of atomic clouds by optical tweezers or magnetic conveyor belts in a scanning probe configuration [22] three-dimensional imaging of the electric field distribution is feasible. However, the measurement technique contaminates the surface, which must be taken into account.

ACKNOWLEDGMENTS

The authors would like to thank Thomas Judd for useful discussions. This work was supported by the European Research Council (Socathes) and the Deutsche Forschungsgemeinschaft (SFB TRR21). The authors acknowledge additional support from the Evangelisches Studienwerk Villigst e.V. and the Baden-Württemberg-Stiftung through the "Kompetenznetz Funktionelle Nanostrukturen."

[1] T. F. Gallagher, *Rydberg Atoms* (Cambridge University Press, Cambridge, UK, 1994).
[2] J. M. Raimond, M. Brune, and S. Haroche, Rev. Mod. Phys. **73**, 565 (2001).
[3] D. Petrosyan and M. Fleischhauer, Phys. Rev. Lett. **100**, 170501 (2008).
[4] D. Petrosyan, G. Bensky, G. Kurizki, I. Mazets, J. Majer, and J. Schmiedmayer, Phys. Rev. A **79**, 040304 (2009).
[5] M. Saffman, T. G. Walker, and K. Mølmer, Rev. Mod. Phys. **82**, 2313 (2010).
[6] L. DiCarlo, J. M. Chow, J. M. Gambetta, L. S. Bishop, B. R. Johnson, D. I. Schuster, J. Majer, A. Blais, L. Frunzio, S. M. Girvin, and R. J. Schoelkopf, Nature (London) **460**, 240 (2009).
[7] A. Wallraff, D. Schuster, A. Blais, L. Frunzio, R. Huang, J. Majer, S. Kumar, S. Girvin, and R. Schoelkopf, Nature (London) **431**, 162 (2004).
[8] S. D. Hogan, J. A. Agner, F. Merkt, T. Thiele, S. Filipp, and A. Wallraff, Phys. Rev. Lett. **108**, 063004 (2012).
[9] J. M. McGuirk, D. M. Harber, J. M. Obrecht, and E. A. Cornell, Phys. Rev. A **69**, 062905 (2004).
[10] J. M. Obrecht, R. J. Wild, and E. A. Cornell, Phys. Rev. A **75**, 062903 (2007).
[11] A. Tauschinsky, R. M. T. Thijssen, S. Whitlock, H. B. van Linden van den Heuvell, and R. J. C. Spreeuw, Phys. Rev. A **81**, 063411 (2010).
[12] M. Mack, F. Karlewski, H. Hattermann, S. Höckh, F. Jessen, D. Cano, and J. Fortágh, Phys. Rev. A **83**, 052515 (2011).
[13] A. K. Mohapatra, T. R. Jackson, and C. S. Adams, Phys. Rev. Lett. **98**, 113003 (2007).
[14] H. Kübler, J. P. Shaffer, T. Baluktsian, R. Löw, and T. Pfau, Nat. Photonics **4**, 112 (2010).
[15] M. Fleischhauer, A. Imamoglu, and J. P. Marangos, Rev. Mod. Phys. **77**, 633 (2005).
[16] D. Cano, H. Hattermann, B. Kasch, C. Zimmermann, R. Kleiner, D. Koelle, and J. Fortágh, Eur. Phys. J. D **63**, 17 (2011).
[17] M. L. Zimmerman, M. G. Littman, M. M. Kash, and D. Kleppner, Phys. Rev. A **20**, 2251 (1979).
[18] R. P. Abel, C. Carr, U. Krohn, and C. S. Adams, Phys. Rev. A **84**, 023408 (2011).
[19] J. A. Crosse, S. A. Ellingsen, K. Clements, S. Y. Buhmann, and S. Scheel, Phys. Rev. A **82**, 010901 (2010).
[20] T. Ohta, A. Bostwick, T. Seyller, K. Horn, and E. Rotenberg, Science **313**, 951 (2006).
[21] K.-H. Jin, S.-M. Choi, and S.-H. Jhi, Phys. Rev. B **82**, 033414 (2010).
[22] M. Gierling, P. Schneeweiss, G. Visanescu, P. Federsel, M. Häffner, D. P. Kern, T. E. Judd, A. Günther, and J. Fortágh, Nat. Nanotechnol. **6**, 446 (2011).

Quasiclassical quantum defect theory and the spectrum of highly excited rubidium atoms

Ali Sanayei and Nils Schopohl*
Institut für Theoretische Physik and CQ Center for Collective Quantum Phenomena and their Applications in LISA⁺, Eberhard-Karls-Universität Tübingen, Auf der Morgenstelle 14, D-72076 Tübingen, Germany

Jens Grimmel, Markus Mack, Florian Karlewski, and József Fortágh†
Physikalisches Institut and CQ Center for Collective Quantum Phenomena and their Applications in LISA⁺, Eberhard-Karls-Universität Tübingen, Auf der Morgenstelle 14, D-72076 Tübingen, Germany
(Received 28 January 2015; published 23 March 2015)

We report on a significant discrepancy between recently published, highly accurate variational calculations and precise measurements of the spectrum of Rydberg states in ^{87}Rb on the energy scale of fine splitting. Introducing a modified effective single-electron potential, we determine the spectrum of the outermost bound electron from a standard WKB approach. Overall very good agreement with precise spectroscopic data is obtained.

DOI: 10.1103/PhysRevA.91.032509 PACS number(s): 31.10.+z, 32.80.Ee

I. INTRODUCTION

The spectrum of the outermost bound electron of an alkali atom such as ^{87}Rb is hydrogenlike but lacks the n^2 degeneracy of the eigenstates labeled by the principal quantum number n of the pure Coulomb potential [1,2]:

$$E_{n,l} = -\frac{1}{(n-\delta_l)^2}. \tag{1}$$

This effect is the well-known quantum defect δ_l, resulting from the interaction of the outermost electron with the ionic core of the atom and the nucleus. In a refined version of the statistical Thomas-Fermi theory [3], an effective potential determining the interaction between the outermost electron and the nucleus can be modeled accurately by a spherically symmetric potential $V_{\rm eff}(r;l)$ depending on the distance r from the center and depending on the orbital angular momentum $l \in \{0,1,2,\ldots,n-1\}$ [2,4,5]:

$$V_{\rm eff}(r;l) = -2\left[\frac{Z_{\rm eff}(r;l)}{r} + V_{\rm pol}(r;l)\right]. \tag{2}$$

Here the function $Z_{\rm eff}(r;l)$ represents a position-dependent weight function that interpolates the value of the charge between unity for large r and charge number Z near to the nucleus for $r \to 0$, and $V_{\rm pol}(r;l)$ represents a short-range interaction taking into account the static electric polarizability of the ionic core [1,6].

Overall good agreement with spectroscopic data of alkali atoms (but discarding the fine splitting) has been reported in [5], choosing

$$Z_{\rm eff}(r;l) = 1 + (Z-1)e^{-ra_1(l)} - re^{-ra_2(l)}\left[a_3(l) + ra_4(l)\right] \tag{3}$$

and

$$V_{\rm pol}(r;l) = \frac{\alpha_c}{2}\frac{1-\exp\left[-\left(\frac{r}{r_c(l)}\right)^6\right]}{r^4}. \tag{4}$$

A table of the parameters $a_1(l)$, $a_2(l)$, $a_3(l)$, $a_4(l)$, α_c, and $r_c(l)$ can be found in [5].

In an attempt to also describe the fine splitting of the excitation spectrum of the outermost electron of ^{87}Rb, it has been suggested [4] to superimpose *a posteriori* a spin-orbit term

$$\widetilde{V}_{\rm SO}(r;j,l) = \frac{V_{\rm SO}(r;j,l)}{[1-\alpha^2 V_{\rm eff}(r;l)]^2} \tag{5}$$

on the potential $V_{\rm eff}(r;l)$, which then influences the spectrum $E_{n,j,l}$ on the scale of fine splitting and the orbitals $\psi_{n,j,l}(r)$ accessible to the outermost electron. Here

$$V_{\rm SO}(r;j,l) = \alpha^2\frac{1}{r}\frac{\partial V_{\rm eff}(r;l)}{\partial r}g(j,l), \tag{6}$$

and $\alpha = \frac{\lambda_C}{a_B} \simeq \frac{1}{137.036}$ denotes the fine-structure constant, and

$$g(j,l) = \begin{cases} 0 & \text{if } l = 0, \\ \frac{j(j+1)-l(l+1)-\frac{3}{4}}{2} & \text{if } l \geqslant 1, \end{cases} \tag{7}$$

where $j \in \{l-\frac{1}{2}, l+\frac{1}{2}\}$. To determine those orbitals (with principal quantum number $n = n_r + l + 1$ and radial quantum number $n_r \in \mathbb{N}_0$), a normalizable solution to the Schrödinger eigenvalue problem for the radial wave function $U_{n,j,l}(r) = rR_{n,j,l}(r)$ and associated eigenvalues $E_{n,j,l} < 0$ is required:

$$\left[-\frac{d^2}{dr^2} + \frac{l(l+1)}{r^2} + \widetilde{V}(r;j,l) - E_{n,j,l}\right]U_{n,j,l}(r) = 0, \tag{8}$$

where

$$\widetilde{V}(r;j,l) = V_{\rm eff}(r;l) + \widetilde{V}_{\rm SO}(r;j,l) \tag{9}$$

denotes the effective single-electron potential.

A highly accurate variational calculation of the excitation spectrum of the outermost electron of ^{87}Rb has been carried out recently [7], in which the authors expand the radial wave function of the Schrödinger eigenvalue problem (8) in a basis spanned by 500 Slater-type orbitals (STOs). On the other hand, modern high-precision spectroscopy of Rydberg levels of ^{87}Rb has been conducted recently. Millimeter-wave spectroscopy employing selective field ionization allows for precise measurements of the energy differences between Rydberg

*nils.schopohl@uni-tuebingen.de
†fortagh@uni-tuebingen.de

TABLE I. Fine splitting $\Delta E_{n,l=1}$ for P states in megahertz.

State $\|n,l=1\rangle$	Expt. [11]	Expt. [8]	Theory [7]	Theory (this work)
8P	$565.1(4)\times 10^3$	NA	602.04×10^3	567.75×10^3
10P	$219.1(4)\times 10^3$	NA	231.87×10^3	218.77×10^3
30P	NA	4246.30(5)	4500.50	4246.46
35P	NA	2566.41(32)	2717.41	2566.28
45P	NA	1144.09(13)	1217.24	1143.95
55P	NA	605.77(7)	644.81	605.68
60P	NA	460.76(5)	480.32	460.68

levels [8]. An independent approach is to perform purely optical measurements on absolute Rydberg level energies by observing electromagnetically induced transparency (EIT) [9,10]. However, there is a systematic discrepancy between variational calculations and the spectroscopic measurements of the fine splitting,

$$\Delta E_{n,l} = E_{n,l+\frac{1}{2},l} - E_{n,l-\frac{1}{2},l}\,, \tag{10}$$

as shown in Tables I and II. Given the fact that the error bars of the independent experiments [8,10] are below 1.1 MHz down to 20 kHz, and on the other hand considering the high accuracy of the numerical calculations presented in [7], such a discrepancy between experiment and theory is indeed significant.

So, what could be the reason for the reported discrepancies? First, it should be pointed out that in the variational calculations [7] a slightly different potential was used, that is,

$$V\,(r;j,l) = V_{\rm eff}(r;l) + V_{\rm SO}\,(r;j,l)\,. \tag{11}$$

Certainly, within the first-order perturbation theory there exists no noticeable discrepancy in the spectrum of the outermost electron on the fine-splitting scale, when taking into account the spin-orbit forces with $V_{\rm SO}\,(r;j,l)$ instead of working with $\widetilde{V}_{\rm SO}\,(r;j,l)$. This is due to the differences being negligible for $r > Z\alpha^2$. However, since $V_{\rm SO}\,(r;j,l)$ eventually dominates even the contribution of the centrifugal barrier term $\frac{l(l+1)}{r^2}$ within the tiny region $0 < r \lesssim \alpha^2 Z$, a subtle problem with a non-normalizable radial wave function $U_{n,j,l}(r)$ emerges when attempting to solve the Schrödinger eigenvalue problem for any $l > 0$ with the potential $V_{\rm SO}\,(r;j,l)$. Such a problem is absent when one works with $\widetilde{V}_{\rm SO}\,(r;j,l)$ [4].

A variational calculation with the potential (11) employing $N = 500$ normalizable STOs as basis functions thus engenders a systematic (small) error of the matrix elements calculated in [7] on the fine-splitting scale. When employing substantially more STOs this error would certainly become larger. With $N = 500$ STOs the discrepancy of these theoretical results with the high-precision spectroscopic data, as shown in Tables I and II, is far too large to be corrected by simply replacing $V_{\rm SO}\,(r;j,l)$ with $\widetilde{V}_{\rm SO}\,(r;j,l)$. Hence another explanation is required.

II. QUASICLASSICAL APPROACH AND FINE SPLITTING OF THE HIGHLY EXCITED ^{87}Rb

In 1941 alkali atoms had already been studied in the context of modern quantum mechanics in the seminal work by Mayer [3], who emphasized the exceptional role of the $l = 1$ and $l = 2$ orbitals. According to Mayer, the outermost electron of an alkali atom is governed by an effective r-dependent charge term

$$Z_{\rm eff}\,(r) = 1 + (Z-1)F(r), \tag{12}$$

where the function $F(r)$ has been determined by employing the semiclassical statistical Thomas-Fermi approach to the many-electron-atom problem, posing the boundary conditions as $\lim_{r\to 0} F(r) = 1$ and $\lim_{r\to\infty} F\,(r) = 0$. As discussed by Schwinger [12], this approach ceases to be valid in the inner-shell region $Z^{-1} < r < Z^{-\frac{1}{3}}$ of the atom. Therefore, taking into account the fine splitting in the spectrum of the outermost electron of alkali atoms *a posteriori* by simply adding the phenomenological spin-orbit term (5) to (2), resulting in the effective single-electron potential (9), seems to be questionable on general grounds in that inner-shell region.

On a more fundamental level, the treatment of relativistic effects in multi-electron-atom spectra requires an *a priori* microscopic description based on the well-known Breit-Pauli Hamiltonian [13,14]:

$$\mathcal{H} = \mathcal{H}_{\rm nr} + \mathcal{H}_{\rm rs} + \mathcal{H}_{\rm fs}. \tag{13}$$

Here $\mathcal{H}_{\rm nr}$ is the ordinary *nonrelativistic* many-electron Hamiltonian, while the *relativistic corrections* are represented by the perturbation operators $\mathcal{H}_{\rm rs}$ and $\mathcal{H}_{\rm fs}$. The perturbation term $\mathcal{H}_{\rm rs}$

TABLE II. Fine splitting $\Delta E_{n,l=2}$ for D states in megahertz.

State $\|n,l=2\rangle$	Expt. [11]	Expt. [8]	Expt. [10]	Theory [7]	Theory (this work)
8D	$30.4(4)\times 10^3$	NA	NA	113.17×10^3	36.42×10^3
10D	$14.9(2)\times 10^3$	NA	NA	52.05×10^3	16.56×10^3
30D	NA	452.42(18)	452.5(11)	1447.53	456.13
35D	NA	279.65(10)	280.4(11)	894.84	281.52
45D	NA	128.33(4)	127.8(11)	407.64	128.98
55D	NA	69.17(2)	69.4(11)	223.71	69.47
57D	NA	61.98(2)	62.2(11)	197.39	62.24

contains all the relativistic perturbations like *mass correction*, one- and two-body *Darwin terms*, and further the *spin-spin contact* and *orbit-orbit* terms, which all commute with the total angular momentum $\mathbf{L}$ and total spin $\mathbf{S}$, thus effectuating only small *shifts* of the spectrum of the nonrelativistic Hamiltonian $\mathcal{H}_{\rm nr}$. The perturbation operator $\mathcal{H}_{\rm fs}$, on the other hand, breaks the rotational symmetry. It consists of the standard *nuclear spin-orbit*, the *spin-other-orbit*, and the *spin-spin dipole* interaction terms, which all commute with $\mathbf{J} = \mathbf{L} + \mathbf{S}$, but not with $\mathbf{L}$ or with $\mathbf{S}$ separately, thus inducing the fine splitting of the nonrelativistic spectrum.

Although the proposed functional form of the potential (11) is highly plausible on physical grounds outside the inner-core region $r > Z^{-\frac{1}{3}}$, *prima facie* it appears to be inconsistent to lump the aforementioned relativistic many-body forces, spin-other-orbit and spin-spin dipole interaction, into an effective single-electron potential of the functional form (11), so that it provides an accurate description also for small distances $Z^{-1} < r < Z^{-\frac{1}{3}}$.

In the absence of a better microscopic theory for an effective single-electron potential $V_{\rm eff}\,(r;j,l)$ describing the fine splitting of the spectrum of the outermost electron in the alkali atoms, we introduce a *cutoff* at a distance $r_{\rm so}(l)$ with $Z^{-1} < r_{\rm so}(l) < Z^{-\frac{1}{3}}$ so that the effective single-electron potential is now described by the following modified potential:

$$\widetilde{V}_{\rm mod}\,(r;j,l) = \begin{cases} V_{\rm eff}(r;l) & \text{if } 0 \leqslant r \leqslant r_{\rm so}(l), \\ V_{\rm eff}(r;l) + V_{\rm SO}\,(r;j,l) & \text{if } r > r_{\rm so}(l). \end{cases} \tag{14}$$

The choice [2]

$$\begin{aligned} r_{\rm so}\,(l=1) &= 0.029\,483 \times r_c\,(l=1) = 0.044\,282\,5, \\ r_{\rm so}\,(l=2) &= 0.051\,262 \times r_c\,(l=2) = 0.249\,572\,0, \end{aligned} \tag{15}$$

gives a surprisingly accurate description of the fine splitting in the spectroscopic data for *all* principal quantum numbers n (see Fig. 1, Tables I and II). By choosing larger values for $r_{\rm so}(l)$ than stated in (15), the calculated fine splitting is too small compared to experiment, and vice versa, by choosing smaller values for $r_{\rm so}(l)$ we find the calculated fine splitting is too large compared to experiment.

The calculation of the spectrum of the outermost bound electron is then reduced to solving the radial Schrödinger equation (8) with the modified potential $\widetilde{V}_{\rm mod}\,(r;j,l)$. The resulting spectrum is actually hydrogenlike, that is,

$$E_{n,j,l} = -\frac{1}{(n-\Delta_{j,l})^2}, \tag{16}$$

where $\Delta_{j,l}$ denotes a quantum defect also comprising the fine splitting. In actual fact the quantum defect describes a reduction of the number of nodes n_r of the radial wave function for $l = 0,1,2$ as a result of the short-range interaction of the outermost electron with the ionic core of the atom. Because the higher the orbital angular momentum quantum number l, the lower the probability of the electron being located near to the center, it is clear that the quantum defect decreases rapidly with increasing orbital angular momentum l. Therefore $\Delta_{j,l}$ is only notably different from zero for $l = 0,1,2$.

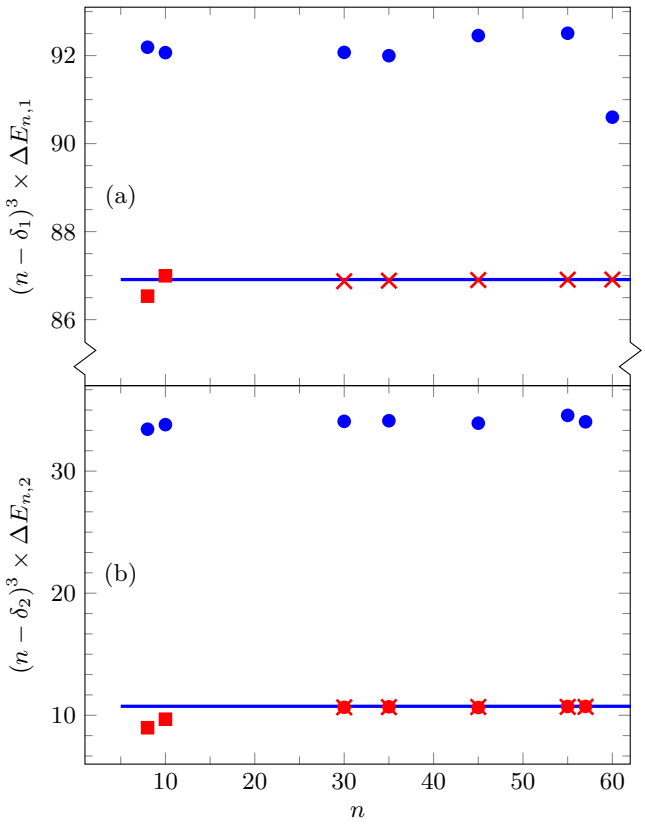

FIG. 1. (Color online) Reduced fine splitting in THz (a) for P states (cf. Table I) and (b) for D states (cf. Table II). The blue line corresponds to the theory from this work [see Eq. (17)]. The blue circles show the recent numerically calculated results from [7]. The red symbols denote experimental data from Refs. [11] (squares), [8] (crosses), and [10] (circles). The error bars for the experimental data are given in Tables I and II.

Writing $\Delta_{j,l} = \delta_l + \eta_{j,l}$ with $\eta_{j,l} \ll \delta_l$, the fine splitting to leading order in α^2 is

$$\Delta E_{n,l} = 2\frac{\eta_{l-\frac{1}{2},l} - \eta_{l+\frac{1}{2},l}}{(n-\delta_l)^3}. \tag{17}$$

The quasiclassical momentum $p \equiv \sqrt{-Q}$ of the bound electron depending on energy $E < 0$ with orbital angular momentum $l > 0$, total angular momentum $j = l \pm \frac{1}{2}$, and taking into account the Langer shift $l(l+1) \to (l+\frac{1}{2})^2$ in the centrifugal barrier [15,16] is then given by

$$Q\,(r;j,l,E) = \frac{\left(l+\frac{1}{2}\right)^2}{r^2} + \widetilde{V}_{\rm mod}\,(r;j,l) - E. \tag{18}$$

For $l = 0$ the centrifugal barrier term and the spin-orbit potential are absent.

Considering high excitation energies $E < 0$ of the bound outermost electron, i.e., a principal quantum number $n \gg 1$, the respective positions of the turning points $r^{(\pm)}$ are given

approximately by

$$r^{(-)} = \frac{\left(l+\frac{1}{2}\right)^2}{1+\sqrt{1+\left(l+\frac{1}{2}\right)^2 E}} \quad \text{if } l \geqslant 3,$$
$$r^{(+)} \simeq \frac{1}{-E}\left[1+\sqrt{1+\left(l+\frac{1}{2}\right)^2 E}\right] \quad \text{if } l \geqslant 1, \tag{19}$$

where $0 < l \ll \frac{1}{\sqrt{-E}}$. Of course, for $l = 0$ only a single (large) turning point $r^{(+)} = \frac{2}{-E}$ exists due to the absence of the centrifugal barrier. However, the lower turning points $r^{(-)}$ are strongly modified for $l = 1,2$ compared to the pure Coulomb potential case, taking into account the core polarization. For $l = 1,2$ the relation $r^{(-)}(l) \simeq 0.02 \times r_c(l)$ holds; that is, $r^{(-)}(l=1) \simeq 0.034\,72$ and $r^{(-)}(l=2) \simeq 0.128\,27$ [2]. While the analytic formula for the lower turning points $r^{(-)}(l)$ in (19), being valid for $3 \leqslant l \ll n$, depends only weakly on the principal quantum number n, we find from numerical calculations with the potential (14) that this also applies for $l = 1,2$ and $n \geqslant 8$. Since the cutoff $r_{so}(l)$ in (15) is substantially above those values of the lower turning points $r^{(-)}(l)$, a quasiclassical calculation of the fine-split spectrum of the bound outermost electron is reliable.

For a chosen radial quantum number n_r, the associated eigenvalues $E = E_{n,j,l} < 0$ of the outermost electron moving in the potential (14) now follow from the WKB patching condition [17–19]:

$$\nu(j,l,E) \stackrel{!}{=} \begin{cases} n_r + 1 & \text{if } l = 0, \\ n_r + \frac{1}{2} & \text{if } l > 0, \end{cases} \tag{20}$$

where $\nu(j,l,E)$ denotes the action integral

$$\nu(j,l,E) = \frac{1}{\pi}\int_{r^{(-)}}^{r^{(+)}} \mathrm{d}r\sqrt{-Q(r;j,l,E)} = \frac{1}{2\pi}\oint \mathrm{d}r\, p(r;j,l,E). \tag{21}$$

Plotting the function $\nu(j,l,E)$ versus $\frac{1}{\sqrt{-E}}$ for $l = 0,1,2$ clearly reveals a linear dependence of the form $\nu(j,l,E) = \frac{1}{\sqrt{-E}} + c(j,l)$ (see Fig. 2).

According to [6], for $A,B,C,D \in \mathbb{R}$, with $A > 0$, $B > 0$, $C > 0$, and $|D| \ll C$, the following equality holds:

$$\frac{1}{2\pi}\oint \mathrm{d}r\sqrt{-A+\frac{2B}{r}-\frac{C}{r^2}+\frac{D}{r^3}} = \frac{B}{\sqrt{A}} - \sqrt{C} + \frac{BD}{2C\sqrt{C}}. \tag{22}$$

For a pure Coulomb potential $A \equiv -E$, $B \equiv 1$, $C \equiv (l+\frac{1}{2})^2$, and $D \equiv \alpha^2 g(j,l)$. The corresponding action integral then reads

$$\nu^{(\mathrm{C})}(j,l,E) = \begin{cases} \frac{1}{\sqrt{-E}} & \text{if } l = 0, \\ \frac{1}{\sqrt{-E}} - \left(l+\frac{1}{2}\right) + \frac{\alpha^2 g(j,l)}{2\left(l+\frac{1}{2}\right)^3} & \text{if } l > 0. \end{cases} \tag{23}$$

It is thus found from WKB theory that the quantum defect associated with the single-electron potential $\widetilde{V}_{\mathrm{mod}}(r;j,l)$ is

$$\Delta_{j,l} = \lim_{E\to 0^-}[\nu(j,l,E) - \nu^{(\mathrm{C})}(j,l,E)]. \tag{24}$$

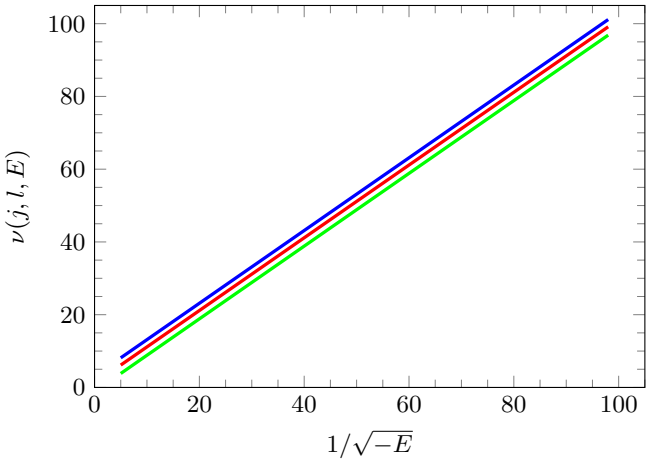

FIG. 2. (Color online) The action integral $\nu(j,l,E)$ associated with the effective single-electron potential $\widetilde{V}_{\mathrm{mod}}(r;j,l)$ vs scaled energy $\frac{1}{\sqrt{-E}}$ for $l = 0$ (blue line), $l = 1$ (red line), $l = 2$ (green line), all for $j = l + \frac{1}{2}$. The curves for $j = l - \frac{1}{2}$ differ only by a tiny shift proportional to α^2.

Ignoring spin-orbit coupling, i.e., for $\alpha = 0$, one has $\Delta_{j,l} \equiv \delta_l$, the standard quantum defect. For $l = 0$ the centrifugal barrier and the spin-orbit coupling term (6) are zero, so $\Delta_{j,l} \to \Delta_{\frac{1}{2},0} \equiv \delta_0$.

The dependence of the quasiclassical momentum $\sqrt{-Q(r;j,l,E)}$ on the scaled distance $\frac{r}{r_c(l)}$ is shown for $l = 0,1,2$ in Fig. 3. Clearly, it is the inner-core region $r^{(-)}(l) < r < r_c(l)$ that provides the main contribution to the quantum defect values. We find, for $l = 0,2$, that changing the fitting parameter $a_3(l)$ in (3) from its tabulated value in [5] according to the scaling prescription $a_3(l=0) \to 0.814 \times a_3(l=0)$ and $a_3(l=2) \to 0.914 \times a_3(l=2)$ leads to a slight downward

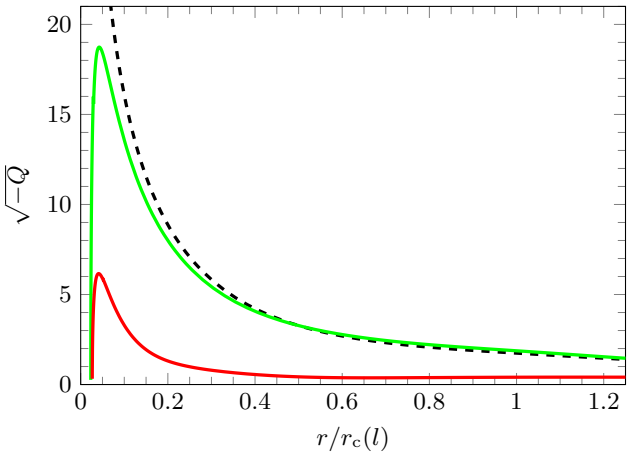

FIG. 3. (Color online) The quasiclassical momentum $\sqrt{-Q(r;j,l,E)}$ vs scaled distance $\frac{r}{r_c(l)}$ for $l = 0$ (dashed black), $l = 1$ (green), and $l = 2$ (red) for $E = E_{n,j,l}$, corresponding to principal quantum number $n = 57$ and $j = l + \frac{1}{2}$. The lower turning points $r^{(-)}(l)$ for the case of a pure Coulomb potential, for $l > 0$ all being greater than $0.6 \times r_c(l)$, are located well outside the core region. The main contribution to the quantum defect values in (24) thus originates from the inner-core region $r < r_c(l)$.

TABLE III. The values of quantum defect $\Delta_{j,l}$ associated with the Rydberg level $n = 57$ for $l = 0,1,2$.

Quantum defect $\Delta_{j,l}$	Expt. [8]	Expt. [10]	Theory [7]	Theory (this work)
$\Delta_{\frac{1}{2},0}$	3.1312419(10)	3.13125(2)	3.12791	3.13095
$\Delta_{\frac{1}{2},1}$	2.6549831(10)	NA	2.65795	2.65197
$\Delta_{\frac{3}{2},1}$	2.6417735(10)	NA	2.64399	2.63876
$\Delta_{\frac{1}{2},1} - \Delta_{\frac{3}{2},1}$	0.0132096(14)	NA	0.01396	0.01321
$\Delta_{\frac{3}{2},2}$	1.3478971(4)	1.34789(2)	1.35145	1.34851
$\Delta_{\frac{5}{2},2}$	1.3462733(3)	1.34626(2)	1.34628	1.34688
$\Delta_{\frac{3}{2},2} - \Delta_{\frac{5}{2},2}$	0.0016238(5)	0.00163(3)	0.00517	0.00163

constant shift of the WKB-quantum defect. As a result of this change, the calculated WKB-quantum defect $\Delta_{l\pm\frac{1}{2},l}$ then agrees well with the spectroscopic data (see Table III). Such a change of $a_3(l)$ does *not* affect the fine-splitting values $\Delta E_{n,l}$ though. We also find that the dependence of the fine splitting $\Delta E_{n,l}$ on the principal quantum number n is well described by (17) for all $n \geqslant 8$ (see Tables I and II).

In actual fact, for $r^{(+)} \gg r^{(-)}$, which is a criterion that is always met for high excitation energies $\sqrt{-E} \simeq 0$ of the outermost electron, the uniform Langer-WKB wave function $U^{(\mathrm{WKB})}_{n,j,l}(r)$ [19,20], with $r^{(+)}$ considered as the only turning point, describes the numerical solution $U_{n,j,l}(r)$ to the radial differential equation (8) under the influence of the effective modified single-electron potential (14) rather accurately [21]. Only very near to the second turning point $r^{(-)}$, at a distance smaller than $r_{\mathrm{so}}(l)$, does the Langer-WKB wave function $U^{(\mathrm{WKB})}_{n,j,l}(r)$ cease to be a good approximation to the numerical solution $U_{n,j,l}(r)$ of the radial Schrödinger equation (8) [21].

III. CONCLUSIONS

In this work we reported a significant discrepancy between experiment [8,10] and highly accurate variational calculations [7] of the spectrum of Rydberg states of ^{87}Rb on the energy scale of the fine splitting. We discussed that the usual *a posteriori* adding of the relativistic spin-orbit potential to the effective single-electron potential governing the outermost electron of alkali atoms is indeed inconsistent inside the inner atomic core region. In the absence of a full microscopic theory that lumps all many-body interactions together with the relativistic corrections into an effective single-electron potential in a consistent manner, we suggested a modified effective single-electron potential, cf. (14), that enables a correct description of the spectrum of Rydberg states on the fine-splitting scale in terms of a simple WKB-action integral for all principal quantum numbers $n \geqslant 8$. Modern precision spectroscopy of highly excited Rydberg states thus enables the probing of the multielectron correlation problem of the ionic core of alkali atoms. This is certainly a fascinating perspective for further experiments and theoretical studies.

ACKNOWLEDGMENTS

This work was financially supported by the EU FET-Open Xtrack Project HAIRS and the Carl Zeiss Stiftung Foundation.

[1] T. F. Gallagher, *Rydberg Atoms*, 1st ed. (Cambridge University Press, Cambridge, UK, 1994).
[2] We use scaled variables so that length is measured in units of the Bohr radius $a_B = \frac{\hbar^2}{m_e}\frac{4\pi\varepsilon_0}{|e|^2} \simeq 5.2918 \times 10^{-11}$ m and energy is measured in units of Rydberg, $\mathrm{Ry} = \frac{m_e|e|^4}{8\varepsilon_0^2 h^2} \simeq 13.605$ eV.
[3] M. Goeppert Mayer, Phys. Rev. **60**, 184 (1941).
[4] C. H. Greene and M. Aymar, Phys. Rev. A **44**, 1773 (1991).
[5] M. Marinescu, H. R. Sadeghpour, and A. Dalgarno, Phys. Rev. A **49**, 982 (1994).
[6] M. Born, *Vorlesungen über Atommechanik* (Springer, Berlin, 1925), §27, §28, and II. Anhang.
[7] M. Pawlak, N. Moiseyev, and H. R. Sadeghpour, Phys. Rev. A **89**, 042506 (2014).
[8] W. Li, I. Mourachko, M. W. Noel, and T. F. Gallagher, Phys. Rev. A **67**, 052502 (2003).
[9] A. K. Mohapatra, T. R. Jackson, and C. S. Adams, Phys. Rev. Lett. **98**, 113003 (2007).
[10] M. Mack, F. Karlewski, H. Hattermann, S. Höckh, F. Jessen, D. Cano, and J. Fortágh, Phys. Rev. A **83**, 052515 (2011).
[11] J. E. Sansonetti, J. Phys. Chem. Ref. Data **35**, 301 (2006).
[12] J. Schwinger, *Quantum Mechanics: Symbolism of Atomic Measurements*, 1st ed. (Springer, Berlin, 2001).
[13] H. A. Bethe and E. E. Salpeter, *Quantum Mechanics of One- and Two-Electron Atoms* (Springer, Berlin, 1957).
[14] C. Froese-Fischer, T. Brage, and P. Jönsson, *Computational Atomic Structure: An MCHF Approach* (IOP Physics, Bristol, 1997).
[15] R. E. Langer, Phys. Rev. **51**, 669 (1937).
[16] M. V. Berry and K. E. Mount, Rep. Prog. Phys. **35**, 315 (1972).
[17] A. B. Migdal, *Qualitative Methods in Quantum Theory* (Addison-Wesley, Reading, MA, 1977).
[18] B. M. Karnakov and V. P. Krainov, *WKB Approximation in Atomic Physics* (Springer, Berlin, 2013).
[19] C. M. Bender and S. A. Orszag, *Advanced Mathematical Methods for Scientists and Engineers* (McGraw-Hill, Singapore, 1978).
[20] R. E. Langer, Bull. Am. Math. Soc. **40**, 545 (1934).
[21] A. Sanayei and N. Schopohl (unpublished).

New Journal of Physics
The open access journal at the forefront of physics

Deutsche Physikalische Gesellschaft DPG
IOP Institute of Physics

Published in partnership with: Deutsche Physikalische Gesellschaft and the Institute of Physics

OPEN ACCESS

RECEIVED
29 January 2015

REVISED
11 March 2015

ACCEPTED FOR PUBLICATION
31 March 2015

PUBLISHED
6 May 2015

PAPER

Measurement and numerical calculation of Rubidium Rydberg Stark spectra

Jens Grimmel[1], **Markus Mack**[1], **Florian Karlewski**[1], **Florian Jessen**[1], **Malte Reinschmidt**[1], **Nóra Sándor**[1,2] and **József Fortágh**[1]

[1] CQ Center for Collective Quantum Phenomena and their Applications, Physikalisches Institut, Eberhard-Karls-Universität Tübingen, Auf der Morgenstelle 14, D-72076 Tübingen, Germany
[2] Wigner Research Center for Physics, Hungarian Academy of Sciences, Konkoly-Thege Miklós út 29-33, H-1121 Budapest, Hungary

E-mail: jens.grimmel@uni-tuebingen.de **and** fortagh@uni-tuebingen.de

Keywords: Rydberg states, Stark effect, electromagnetically induced transparency, precision spectroscopy

Supplementary material for this article is available online

Abstract

We report on the measurement of Stark shifted energy levels of ^{87}Rb Rydberg atoms in static electric fields by means of electromagnetically induced transparency (EIT). Electric field strengths of up to 500 V cm^{-1}, ranging beyond the classical ionization threshold, were applied using electrodes inside a glass cell with rubidium vapour. Stark maps for principal quantum numbers $n = 35$ and $n = 70$ have been obtained with high signal-to-noise ratio for comparison with results from *ab initio* calculations following the method described in (Zimmerman *et al* 1979 *Phys. Rev.* A **20** 2251), which was originally only verified for states around $n = 15$. We also calculate the dipole matrix elements between low-lying states and Stark shifted Rydberg states to give a theoretical estimate of the relative strength of the EIT signal. The present work significantly extends the experimental verification of this numerical method in the range of both high principal quantum numbers and high electric fields with an accuracy of up to 2 MHz.

1. Introduction

The response of atoms to static electric fields (dc Stark effect) results in line shifts, state mixing and, for sufficiently large fields, ionization. The line shifts are conventionally summarized in Stark maps, displaying the energy levels as a function of the applied field. Stark maps of alkali atoms are routinely calculated by diagonalising the perturbed Hamiltonian [1], taking into account quantum defects and corresponding electronic wavefunctions [2]. A precise knowledge and control of Stark shifted Rydberg states is required for the application of Rydberg atoms as quantum probes [3], for controlling the interactions between Rydberg atoms [4], the production of circular Rydberg atoms [5], the structure and dynamics of Rydberg gases [6, 7], and possible applications in quantum information processing [8]. In the context of hybrid quantum systems based on atoms and solid state quantum circuits [9, 10], Stark shifts of Rydberg states [11–13] and their control [14] are of particular interest.

Stark maps of Rydberg excited alkali atoms were studied in the 1970s using pulsed laser excitations and subsequent pulsed-field ionization [1, 15]. For low-lying Rydberg states of sodium, lithium and caesium with principal quantum numbers $n < 20$, Stark maps have been recorded up to and beyond the classical ionization limit [1, 15]. Stark maps of ^{85}Rb for n up to 55 were studied in the 1980s for low electric fields using two-photon laser excitation and detecting ionization from thermal collisions [16]. In this regime of low electric fields the Stark maps do not show level crossings but quadratic dependence on the applied field with slight deviation from this for highly excited states ($n = 55$).

Many recent experiments on Stark shifts use electromagnetically induced transparency (EIT) [17–19]. This spectroscopic method provides a high resolution of the energy levels [18] and is suitable for the detection of states of high principal quantum numbers. However, the measurements so far only covered the range of low

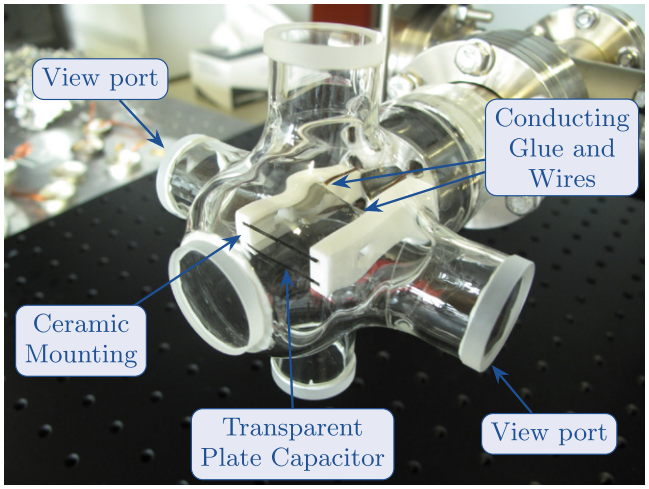

Figure 1. Vapour cell with electrodes. The capacitor plates are formed by two glass plates with 5 nm of nickel facing each other at a separation of 5 mm. Two wires are glued to each capacitor plate to contact them. For the measurements the laser beams counterpropagate through the view ports indicated in the image.

electric fields, in which just the first avoided crossings appear. Similarly, the detection of ions by micro-channel plates [20] and the technique of measuring the ionization currents from Stark-shifted Rydberg states [21] have only been used at low electric fields.

In this article, we report on the optical spectroscopy of Stark shifted Rydberg states with principal quantum numbers of $n = 35$ and $n = 70$ for electrostatic fields between 0 and 500 V cm^{-1}, ranging beyond the classical ionization limit. Our measurements go to higher principal quantum numbers and cover a three to four times larger range of electric fields relative to the classical ionization threshold than any of the aforementioned works using EIT. The observed Stark maps are compared with results from numerical calculations following the lines of the numerical method by [1], including the recently improved accuracy of the quantum defects [22]. In the original work this method was optimized for Rydberg states around $n = 15$ due to computational limitations as well as the accessible experimental data. The high accuracy of this method at low electric fields is always given by the accuracy of the unperturbed energy levels, which are used in the calculation. However, for strong electric fields and high principal quantum numbers, where a high accuracy of the calculated energy levels is desirable, this method becomes more susceptible to numerical errors [1]. In this article we show by direct comparison, that it is still applicable even in these regions of study. Furthermore, we calculate dipole matrix elements between $5P_{3/2}$ and the observed Stark shifted states, which are then used to give an estimate for the relative strength of the measured signals.

2. Measurement of Stark maps

For the measurement of Stark shifts of ^{87}Rb Rydberg atoms we use a vapour cell with a pair of plate electrodes for applying homogeneous electric fields. The electrodes are inside the cell (figure 1), trying to avoid the effect observed in previous works where static electric fields applied to a vapour cell with outside electrodes are compensated by ionized rubidium and electrons [23]. The rubidium vapour in the cell is at room temperature with an estimated pressure of $\approx 1 \cdot 10^{-7}$ mbar. The electrodes in the center of the glass cell (figure 1) are formed by two square glass plates coated with 5 nm of nickel. This gives the plates ≈60% transparency, which allows for optical access on the axis perpendicular to them. However, this optical access was not used in the experiments presented in this work. The plates are mounted with 5 mm separation on insulating ceramics (Macor) and connected to a voltage source through metallic wires. Laser beams for the optical spectroscopy are introduced through view ports and pass through the cell between the plates.

We measure the transition frequency from the rubidium ground state to Rydberg states by EIT. The EIT three level ladder scheme [23] consists of the ground state $5S_{1/2}(F = 2)$, the intermediate state $5P_{3/2}(F = 3)$ and a Rydberg state nS or nD (figure 2). However, it is important to keep in mind that l is not a good quantum number any more in the presence of an external electric field and that the Stark shifted states can be considered as a mix of all possible unperturbed l states. For the spectroscopy we use a *probe* laser that is locked to the $5S_{1/2}(F = 2) \rightarrow 5P_{3/2}(F = 3)$ transition (780 nm) and a *coupling* laser with a variable frequency close to the

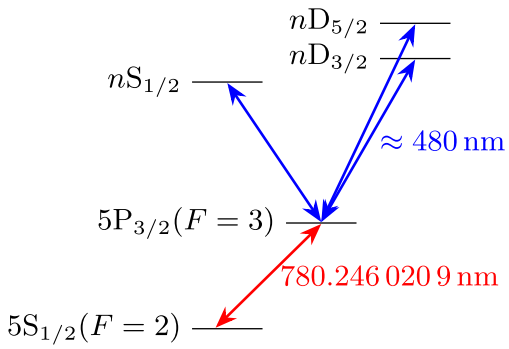

Figure 2. Ladder scheme for electromagnetically induced transparency (EIT). For our measurements the probe laser is held on resonance with the $5S_{1/2}(F = 2) \rightarrow 5P_{3/2}(F = 3)$ transition of ^{87}Rb and the coupling laser is scanned around the upper transition. Dipole selection rules only allow for the measurement of nS and nD states in this scheme.

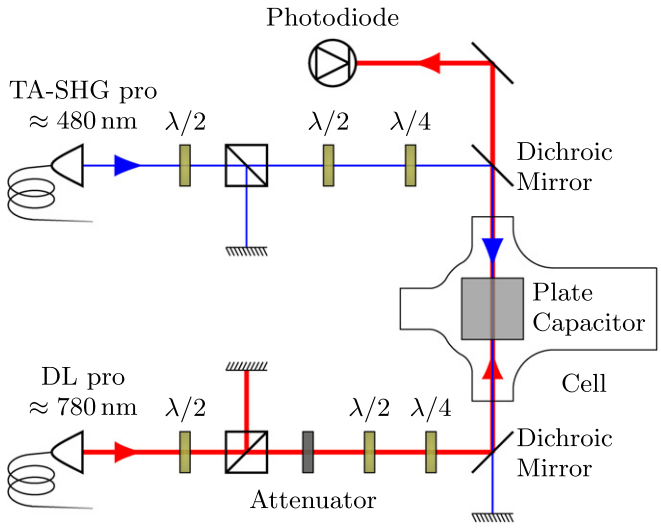

Figure 3. Optical setup (schematic) for the measurement of Stark maps using EIT. Both lasers are guided to the experiment through optical fibers and overlapped within the volume of the plate capacitor using two dichroic mirrors. Intensity and polarization of both lasers are adjusted independently. The transmission of the probe beam through the vapour cell is measured with a photodiode.

transition between $5P_{3/2}(F = 3)$ and a Rydberg state (480 nm). When the coupling laser is resonant with this transition we detect a maximum in the transmission of the probe laser through the vapour.

We use a grating-stabilized diode laser (Toptica, DL pro) of ≈100 kHz linewidth as the probe laser and a frequency-doubled, grating-stabilized diode laser of ≈200 kHz linewidth (Toptica, TA-SHG pro) as the coupling laser. Both lasers are phase-locked to a frequency comb (Menlo Systems, FC 1500). For conveniently selecting the right modes of the frequency comb for both lasers we use a calibrated wavelength meter (HighFinesse, WS Ultimate 2) [22]. The power of the probe laser is 1 μW and the power of the coupling laser is 25 mW with $1/e^2$ diameters of 450 and 150 μm in the cell, respectively. The small diameter of the coupling beam results in a high intensity and therefore high Rabi frequency on the corresponding transition while the bigger diameter of the probe beam is chosen in order to ensure maximal overlap of the two beams within the cell. The laser powers and polarizations were adjusted to maximize the EIT signal in zero field (figure 3). A measurement of the polarizations after this adjustment revealed that this resulted in circular polarizations for both lasers. The frequency of the probe laser is kept on resonance with the $5S_{1/2}(F = 2) \rightarrow 5P_{3/2}(F = 3)$ transition (figure 2) and its transmission through the cell is measured using an avalanche photodiode.

In order to reach a high signal-to-noise ratio in the spectroscopy, we use the following lock-in measurement technique. We modulate the power of the coupling laser using an acousto-optic modulator and demodulate the signal from the photodiode on the carrier frequency. In addition we modulate the frequency of the intensity modulation and demodulate the photodiode signal on two of the sidebands that arise from this. We then average the demodulated signal from the carrier and both sidebands. The additional frequency modulation decreases the signal strength on the carrier frequency and creates an even lower signal strength on the sidebands, but averaging

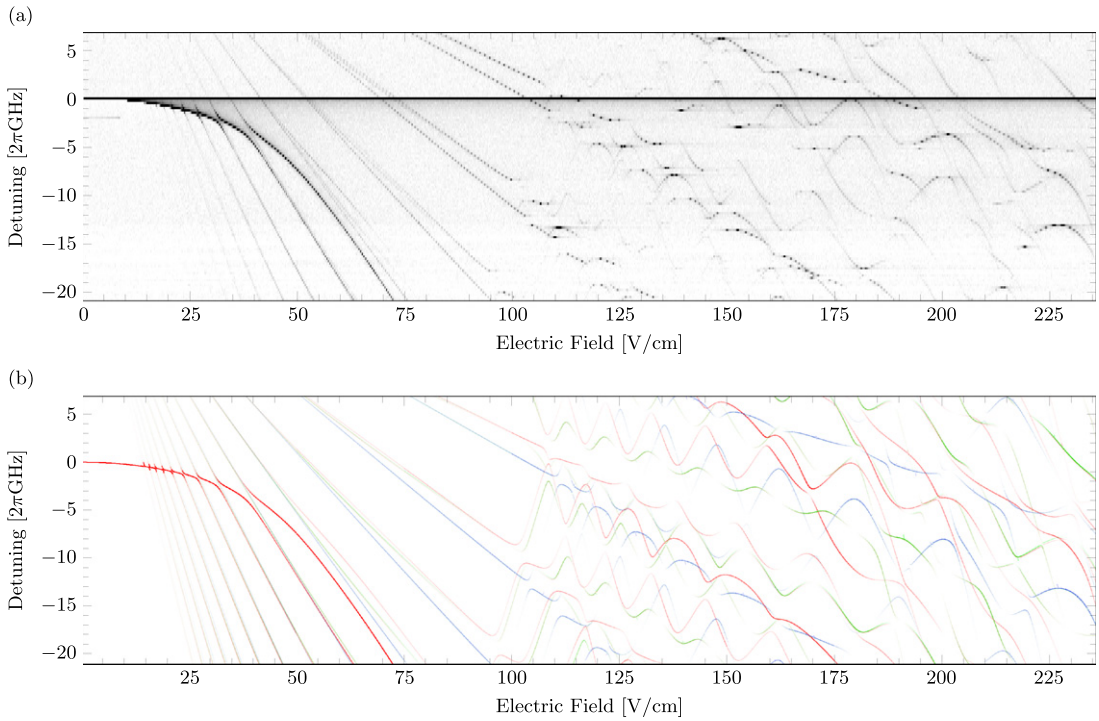

Figure 4. (a) Stark map for $35S_{1/2}$ for an electric field range of 0–235 V cm^{-1}. The gray scale is determined from the measured EIT signal, which represents the demodulated transmission signal from the photodiode. Due to the frequency resolution of 125 MHz some of the lines with a small slope appear dotted here. (b) The red, green and blue lines show the numerically calculated Stark map for $|m_j| = 1/2$, $|m_j| = 3/2$ and $|m_j| = 5/2$, respectively. The opacity gradients indicate the calculated transition strength D to the corresponding Stark shifted Rydberg states. In this region we find a very good agreement between experimental and numerically calculated results in the Stark shifts as well as the transition strengths.

the signal from three frequencies lowers the noise level at the same time. In total, the resulting signal-to-noise ratio is improved by a factor of ≈2 as compared to a simple lock-in measurement without frequency modulation. For every set frequency of the coupling laser we ramp up the voltage on the plate capacitor using an auxiliary output of the lock-in amplifier (Zurich Instruments, HF2LI). This is sufficient for electric fields up to ≈20 V cm^{-1}. For even higher fields up to ≈500 V cm^{-1} we use an additional voltage amplifier.

Measured data near the unperturbed $35S_{1/2}$ state is shown in figures 4 and 5. Near the unperturbed $70S_{1/2}$ state we conducted a preliminary measurement, which is not shown in this work, and then selected a smaller region for a more detailed measurement in order to test the frequency precision of the numerical calculations (figure 6). Each pixel in the gray scale images represents an average of the demodulated signal over 200 ms. Between every two pixels we add a waiting time of 50 ms to allow for the low-pass filter of the lock-in amplifier to settle. The gray scale was adjusted with a cutoff for better visibility of weaker signals. Our data shows states ranging up to and even beyond the classical ionization threshold that have not been measured by means of EIT before. The classical ionization threshold E_{ion}, i.e. the saddle point which is formed by a Coulomb potential with an external electric field F, is given by

$$E_{\mathrm{ion}} = -2\sqrt{F} \tag{1}$$

in atomic units ([2]). This results in an electric field strength for the ionization threshold of ≈312 V cm^{-1} for $35S_{1/2}$ and ≈16 V cm^{-1} for $70S_{1/2}$. For a quantitative analysis we give a brief review of the numerical calculation of Stark maps in section 3.

We observe two background effects (figures 4 and 6) which are caused by the region of the cell that is not covered by the plate capacitor (figure 1). The first is the line of the unperturbed state, which remains visible for all applied voltages because we probe those outer regions of the cell as well. The second is a smearing of the lines to the right at low fields as visible in figure 4 at the avoided crossings up to ≈50 V cm^{-1} and in figure 6. For a certain electric field strength inside the plate capacitor one always finds lower electric field strengths in the inhomogeneous outside region, causing the asymmetry of the smearing to the right.

Inside the capacitor undesirable electric fields could also arise from the dipole which is formed between adsorbed rubidium and the nickel surface of the capacitor plates. In previous experiments the repeated deposition of cold atom clouds of rubidium onto a copper surface led to electric fields close to the surface which saturated as the number of deposited clouds increased [11]. Since the work functions of nickel and copper are

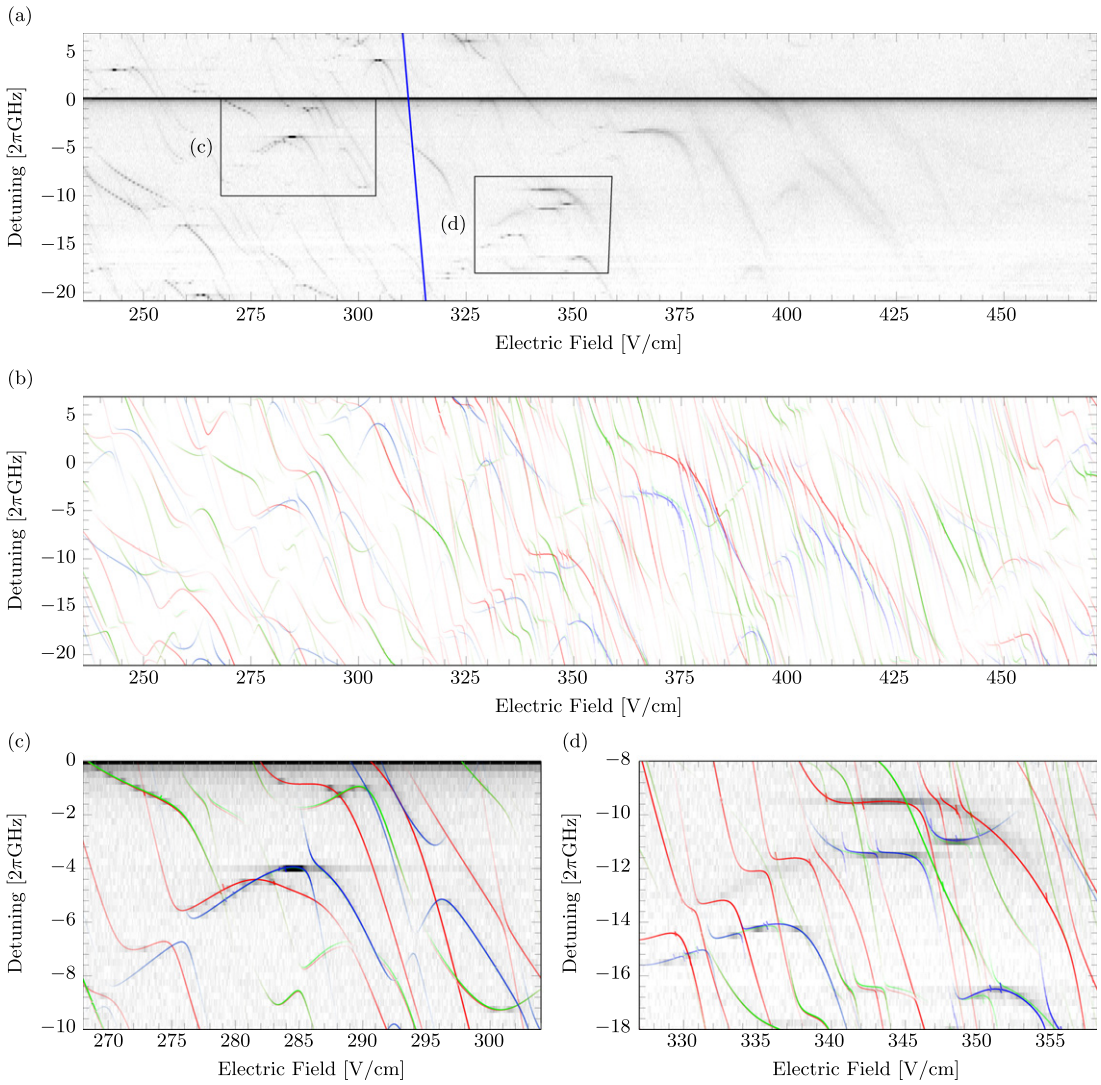

Figure 5. (a) Stark map for $35S_{1/2}$ for an electric field range of 235–470 V cm^{-1}. The gray scale represents the measured EIT signal. Due to the frequency resolution of 125 MHz some of the lines with a small slope appear dotted here. The blue solid line indicates the classical ionization limit. Beyond this limit fewer states are present in the measurement. The states also appear broader and weaker as the external electric field lowers and extends the opening of the potential barrier it forms with the atomic potential. (b) Results from our numerical calculations for the same region. The red lines represent $|m_j| = 1/2$, the green lines $|m_j| = 3/2$ and the blue lines $|m_j| = 5/2$ with the opacity gradients indicating the calculated transition strengths D to each state. (c) and (d) show details of the measurement with the numerically calculated Stark map on top. The opacity of the colors has been increased with a linear scaling in comparison to (b) for better visibility of the calculated lines on top of the experimental data. The agreement in the energy levels remains even beyond the classical ionization threshold, but we find some discrepancies in the transition strengths as the electric field strength increases.

similar and the cell is filled with rubidium vapour at all times we may find a similar effect for the capacitor plates. This effect may play a role for Rydberg states higher than $n = 70$ at low electric fields, but is negligible for the measured data presented in this article, where the distance between the laser beams and the capacitor plates is ≈2 mm. Other stray fields could originate from outside of the cell, but should be compensated by electrons and ionized rubidium [23].

3. Calculation of Stark maps and dipole matrix elements

The Hamiltonian for the valence electron in an alkali atom with an external electric field in z-direction can be written as

$$\hat{H} = \hat{H}_0 + E\hat{z} \tag{2}$$

in atomic units with $\hat{H}_0$ the Hamiltonian for the valence electron in absence of any perturbation, E the electric field strength and $\hat{z}$ the position operator in z-direction. For the following calculations we include the fine structure splitting in $\hat{H}_0$ and neglect the hyperfine structure splitting as it is smaller than our frequency

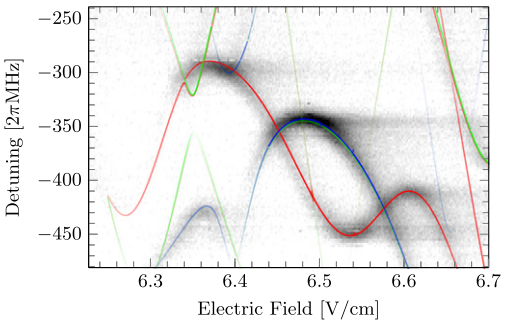

Figure 6. Detailed part of a Stark map for $70S_{1/2}$ for an electric field range of 6.23–6.70 V cm^{-1}. The gray scale represents the measured EIT signal. The red, green and blue lines plotted on top of the measured signal show the numerically calculated Stark map for $|m_j| = 1/2$, $|m_j| = 3/2$ and $|m_j| = 5/2$, respectively, with the opacity gradient scaled to the calculated transition strength D. The frequency resolution of this measurement is 2 MHz and, again, we find a very good agreement between the experimental and numerically calculated results.

resolution in the experiment [1]. The Stark shifts of the $5S_{1/2}(F = 2)$ and $5P_{3/2}(F = 3)$ states from the EIT scheme are negligible as well, as they amount to less than 100 kHz for the region of the field strength up to 500 V cm^{-1}. We then create a matrix representation of $\hat{H}$ in a subset of the basis given by $\hat{H}_0$. This way $\hat{H}_0$ is represented by a diagonal matrix with the energy levels from [22] on its diagonal.

The matrix representation of $\hat{z}$ is symmetric with only off-diagonal entries and in spherical coordinates we obtain from [1]

$$\left\langle n,\, l,\, j,\, m_j \,|\hat{z}|\, n',\, l',\, j',\, m_j' \right\rangle = \delta_{m_j,m_j'}\delta_{l,l'\pm1}\langle n,\, l,\, j \,|r|\, n',\, l',\, j'\rangle \sum_{m_l=m_j\pm\frac{1}{2}} \left\{ \left\langle l,\, \frac{1}{2},\, m_l,\, m_j - m_l \middle| j,\, m_j \right\rangle \times \left\langle l',\, \frac{1}{2},\, m_l,\, m_j - m_l | j',\, m_j \right\rangle \langle l,\, m_l \,|\cos\theta|\, l',\, m_l\rangle \right\} \tag{3}$$

with the radial overlap integral $\langle n,\, l,\, j \,|r|\, n',\, l',\, j'\rangle$ in the first line of the right hand side. From the Kronecker delta $\delta_{m_j,m_j'}$ we can see that the matrix representations of H for different values of m_j can be calculated separately. It is also evident that the Stark shifts for $\pm|m_j|$ are always equal. Therefore we only calculate matrix representations for positive values of m_j in this step. This reduces the computing time for diagonalizing the matrices, but we need to consider states with both signs for the calculation of transition strengths later on again.

For the calculation of the overlap integrals we tried two different methods to calculate the radial wavefunctions for all states in the chosen subset of the basis and also for $5S_{1/2}(F = 2)$ and $5P_{3/2}(F = 3)$, which will be used later on in the calculation of the measure for the transition strengths. One method was to further follow [1] using their atomic potential for ^{87}Rb and Numerov's method to solve the radial Schrödinger equation. We also tried using the parametric model potential from [24] with another solving algorithm[3], which allowed us to obtain parts of the wavefunctions that are located further inside the ionic core. While the two methods lead to slightly different amplitudes of the wavefunctions due to normalization, the differences in the Stark shifts and transition strengths calculated from the two methods for the observed states lie below our experimental accuracy. All calculations presented in this work utilized the latter method.

We can then calculate the matrix representations of the perturbed Hamiltonians H using equation (3) and diagonalize them efficiently in parallel for different values of the electric field strength to obtain the energy eigenvalues. In this step we also calculate the eigenvector β corresponding to every eigenvalue. With this we can further follow the method from [1] to represent every Stark shifted Rydberg state ξ as a linear combination of unperturbed states, given by the eigenvectors, and calculate the dipole matrix elements

$$\langle \xi \,|\vec{r}|\, 5P_{3/2},\, F = 3,\, m_F\rangle \quad = \sum_{n,l,j,m_j} \beta_{n,l,j,|m_j|} \left\langle n,\, l,\, j,\, m_j \,|\vec{r}|\, 5P_{3/2},\, F = 3,\, m_F \right\rangle \tag{4}$$

with $\beta_{n,l,j,|m_j|}$ the entry of β that corresponds to the states $|n,\, l,\, j,\, \pm|m_j|\rangle$. Here we sum over all states in the selected subset of the basis given by the unperturbed states and both signs for each value of m_j. For the calculation of the dipole matrix elements between the unperturbed Rydberg states and $|5P_{3/2},\, F = 3,\, m_F\rangle$ we separate the radial and the angular parts of the wavefunctions. We use the radial overlap integrals from equation (3) and calculate the three components of the angular overlap integrals following [25].

[3] MATLAB 2014a; Solver function: ode45.

We take into account the effect of the probe laser, which couples the different m_F substates of $|5S_{1/2},\ F = 2\rangle$ and $|5P_{3/2},\ F = 3\rangle$ by calculating the weighting factors

$$\eta_{m_F} = \sum_{m_F'} \left| \left\langle 5P_{3/2},\ F = 3,\ m_F \left| \vec{\varepsilon}_p \vec{r} \right| 5S_{1/2},\ F' = 2,\ m_F' \right\rangle \right|^2 \tag{5}$$

with $\vec{\varepsilon}_p$ the polarization of the probe laser. In this step we assume that all m_F substates of $|5S_{1/2},\ F = 2\rangle$ are evenly occupied. The weighting factors are then used to calculate the measure for the transition strength

$$D = \sum_{m_F} \eta_{m_F} \left| \langle \xi \left| \vec{\varepsilon}_c \vec{r} \right| 5P_{3/2},\ F = 3,\ m_F \rangle \right|^2 \tag{6}$$

with $\vec{\varepsilon}_c$ the polarization of the coupling laser. In the experiment the two lasers are counterpropagating and perpendicular to the external electric field with circular polarizations. Therefore we use $\vec{\varepsilon}_p = \vec{\varepsilon}_c = (0,\ i,\ 1)$ here. The measure for the transition strength D is used to determine the opacity gradients for the lines in figures 4–6.

The Stark map for $35S_{1/2}$, which is shown in figures 4 and 5, was calculated from a subset of the basis of approximately 1600 states and for 2000 values of the electric field strength using MATLAB. For $70S_{1/2}$, shown in figure 6, the calculations run similarly with 4000 states and 500 values of the electric field strength. The number of states that was used for these calculations was adjusted so that a further increase only yields changes which lie below the accuracy of the experimental data. Calculated Stark maps for $|m_j| = 1/2$, $|m_j| = 3/2$ and $|m_j| = 5/2$ are included in the figures. The measurements were performed in frequency regions around S states, but since l is not a good quantum number any more in the presence of an electric field [1], we find that other states with $|m_j| = 3/2$ and $|m_j| = 5/2$ are shifted far enough by the Stark effect to appear within the measured frequency range.

4. Comparison of measurements and calculations

Figures 4 and 5 show comparisons of the measured and numerically calculated Stark maps for $35S_{1/2}$. The frequency axis shows the detuning of the coupling laser relative to the absolute value of the transition frequency from [22]. A linear scaling with an offset has been applied to the electric field axis of the measured data. Using only this scaling we achieve a match between calculated and measured energy levels for Stark states in the whole range of our measurement.

The lines in the calculated Stark maps are drawn with an opacity gradient, resulting in a color range between white and the respective color associated with the different values for $|m_j|$. The opacity gradient is scaled to D from equation (6) with an upper cutoff at 70% of its maximum for better visibility. We find a good agreement between this calculated measure for the transition strength and the experimental data in the range of electric fields shown in figure 4. The quality of the agreement deteriorates slightly approaching the classical ionization threshold, but there is still good agreement beyond this point, as can be seen in figure 5. The very weak signals we still find in the experimental data at electric fields around 400 V cm^{-1} all correspond to calculated states with a strong calculated transition strength. Considering this, we think that the method described here can be applied for these high electric field strengths, where only few states are still visible in the experimental data, as a way to select potentially interesting areas before a measurement.

One important cause for discrepancies between the experimental and numerically calculated data we present here is that no ionization effects were taken into account for the calculations. However, it is interesting to note that even though the calculated measure for the transition strength shows some differences at high electric fields, we still find a remarkable agreement of calculated and measured energy levels in this region of study. These differences could be related to the calculation of the radial wavefunctions. We calculate the radial wavefunctions for $|5S_{1/2}\rangle$ and $|5P_{3/2}\rangle$ using the same method as for Rydberg states. Evidently this works quite well here, but more accurate radial wavefunctions, especially for $|5P_{3/2}\rangle$ but also for Rydberg states with low l, could further improve the quality of the calculated transition strengths. This is further emphasized as the biggest discrepancies of the transition strengths at high electric fields can be found for states $|m_j| = 1/2$ while states with $|m_j| = 5/2$ show hardly any discrepancies on the whole range of electric fields. On the other hand, these discrepancies could also be explained by a stronger coupling of Rydberg states with low l to the continuum. Some disagreements on the whole range of our measurements can also be caused by the scaling of the EIT signal with the dipole matrix elements, which is only approximated by the squared scaling in D. Furthermore, lines with small slopes and especially local extrema may appear over-pronounced in the experimental data. Since these parts of the lines are broad in the electric field domain and the inhomogeneous electric field outside of the plate capacitor still lies within the volume of the cell, this results in an effective contribution of more atoms to the signal.

We find a match similar to the one presented for $35S_{1/2}$ in the energy levels and transition strengths for $70S_{1/2}$, which is shown in detail in figure 6. Discrepancies lie within the frequency resolution of 2 MHz for figure 6, which is the highest accuracy we present here. The opacity gradients were assigned the same way as for

$35S_{1/2}$. The calculated transition strengths match the experimental data equally well as for $35S_{1/2}$. The experimental data presented in figures 4–6 is provided as supplementary data to this article[4]. All results presented in this work were measured and calculated in the energy range near nS states. However, they intrinsically include contributions from all possible l states due to the mixing of states caused by the external electric field.

For a possible extension of our measurements to a wider range of principal quantum numbers n than the region between $n = 35$ and $n = 70$, the most important limiting factor is that the coupling of Rydberg states to the intermediate $5P_{3/2}(F = 3)$ grows weaker as n increases, which leads to a lower signal-to-noise ratio. Another factor influencing the signal-to-noise ratio is the density of the vapour, which on the other hand gives rise to collective effects which in turn cause undesired changes of the EIT signal [26].

5. Conclusion

In summary, we have demonstrated agreement between measured and calculated Stark maps of ^{87}Rb up to an accuracy of 2 MHz. This agreement holds for the range from zero field to beyond the classical ionization threshold and for principal quantum numbers $n = 35$ and $n = 70$. Such data and calculations may aid the accurate mapping of electric fields at surfaces [11]. Furthermore, we presented numerical calculations to estimate the transition strength from low-lying states to Stark shifted Rydberg states. The results from these calculations show a very good agreement with our experimental data on a high range of electric fields and even beyond the classical ionization threshold.

Altogether, the methods presented in this paper can be used to find experimentally accessible Stark shifted Rydberg states with an appropriate sensitivity to external electric fields for a wide range of applications. For example, the dependence of the transition strength to different Stark shifted Rydberg levels could be used to determine not only the strength of an external electric field in an experimental system but also the electric field axis.

Acknowledgments

This work was financially supported by the FET-Open Xtrack Project HAIRS and the Carl Zeiss Stiftung. Nóra Sándor acknowledges financial support from the framework of TÁMOP-4.2.4.A/2-11/1-2012-0001 'National Excellence Program'. We thank Nils Schopohl and Ali Sanayei for helpful discussions. We acknowledge support by Deutsche Forschungsgemeinschaft and Open Access Publishing Fund of University of Tübingen.

References

[1] Zimmerman M L, Littman M G, Kash M M and Kleppner D 1979 *Phys. Rev.* A **20** 2251
[2] Gallagher T F (ed) 1994 *Rydberg Atoms* 1st edn (Cambridge: Cambridge University Press)
[3] Guerlin C, Bernu J, Deleglise S, Sayrin C, Gleyzes S, Kuhr S, Brune M, Raimond J-M and Haroche S 2007 *Nature* **448** 889
[4] Daschner R, Ritter R, Kübler H, Frühauf N, Kurz E, Löw R and Pfau T 2012 *Opt. Lett.* **37** 2271
[5] Anderson D A, Schwarzkopf A, Sapiro R E and Raithel G 2013 *Phys. Rev.* A **88** 031401
[6] Comparat D and Pillet P 2010 *J. Opt. Soc. Am.* B **27** A208
[7] Beterov I I, Ryabtsev I I, Tretyakov D B and Entin V M 2009 *Phys. Rev.* A **79** 052504
[8] Paredes-Barato D and Adams C S 2014 *Phys. Rev. Lett.* **112** 040501
[9] Petrosyan D and Fleischhauer M 2008 *Phys. Rev. Lett.* **100** 170501
[10] Tauschinsky A, Thijssen R M T, Whitlock S, van Linden van den Heuvell H B and Spreeuw R J C 2010 *Phys. Rev.* A **81** 063411
[11] Hattermann H, Mack M, Karlewski F, Jessen F, Cano D and Fortágh J 2012 *Phys. Rev.* A **86** 022511
[12] Abel R P, Carr C, Krohn U and Adams C S 2011 *Phys. Rev.* A **84** 023408
[13] Chan K S, Siercke M, Hufnagel C and Dumke R 2014 *Phys. Rev. Lett.* **112** 026101
[14] Jones L A, Carter J D and Martin J D D 2013 *Phys. Rev.* A **87** 023423
[15] Littman M G, Zimmerman M L, Ducas T W, Freeman R R and Kleppner D 1976 *Phys. Rev. Lett.* **36** 788
[16] O'Sullivan M S and Stoicheff B P 1986 *Phys. Rev.* A **33** 1640
[17] Fahey D P and Noel M W 2011 *Opt. Express* **19** 17002
[18] Tauschinsky A, Newell R, Van Linden van den Heuvell H B and Spreeuw R J C 2013 *Phys. Rev.* A **87** 042522
[19] Bason M G, Tanasittikosol M, Sargsyan A, Mohapatra A K, Sarkisyan D, Potvliege R M and Adams C S 2010 *New J. Phys.* **12** 065015
[20] Grabowski A, Heidemann R, Lw R, Stuhler J and Pfau T 2006 *Fortschr. Phys.* **54** 765
[21] Barredo D, Kübler H, Daschner R, Löw,and R and Pfau T 2013 *Phys. Rev. Lett.* **110** 123002
[22] Mack M, Karlewski F, Hattermann H, Höckh S, Jessen F, Cano D and Fortágh J 2011 *Phys. Rev.* A **83** 052515
[23] Mohapatra A K, Jackson T R and Adams C S 2007 *Phys. Rev. Lett.* **98** 113003
[24] Marinescu M, Sadeghpour H R and Dalgarno A 1994 *Phys. Rev.* A **49** 982
[25] Bethe H A and Salpeter E E 1957 *Quantum Mechanics of One- and Two-Electron Atoms* (Berlin: Springer) p 8, 368 S
[26] Ates C, Sevinçli S and Pohl T 2011 *Phys. Rev.* A **83** 041802

[4] See supplementary data available at stacks.iop.org/njp/17/053005/mmedia for the experimental data.

State-selective all-optical detection of Rydberg atoms

Florian Karlewski,[1,*] Markus Mack,[1] Jens Grimmel,[1] Nóra Sándor,[1,2,†] and József Fortágh[1,‡]

[1]*CQ Center for Collective Quantum Phenomena and their Applications, Physikalisches Institut, Eberhard-Karls-Universität Tübingen, Auf der Morgenstelle 14, D-72076 Tübingen, Germany*

[2]*Institute for Solid State Physics and Optics, Wigner Research Centre for Physics, Hungarian Academy of Sciences, H-1525 Budapest P.O. Box 49, Hungary*

(Received 13 February 2015; published 29 April 2015)

We present an all-optical protocol for detecting population in a selected Rydberg state of alkali-metal atoms. The detection scheme is based on the interaction of an ensemble of ultracold atoms with two laser pulses: one weak probe pulse which is resonant with the transition between the ground state and the first excited state, and a pulse with high intensity which couples the first excited state to the selected Rydberg state. We show that by monitoring the absorption signal of the probe laser over time, one can deduce the initial population of the Rydberg state. Furthermore, it is shown that—for suitable experimental conditions—the dynamical absorption curve contains information on the initial coherence between the ground state and the selected Rydberg state. We present the results of a proof-of-principle measurement performed on a cold gas of ^{87}Rb atoms. The method is expected to find application in quantum computing protocols based on Rydberg atoms.

DOI: 10.1103/PhysRevA.91.043422 PACS number(s): 32.80.Ee, 32.80.Qk, 32.80.Rm

I. INTRODUCTION

Rydberg atoms coupled to electromagnetic fields form a promising system for the physical realization of quantum information protocols [1] and quantum simulations [2]. In these protocols qubits are realized by a set of atomic states, which includes one or potentially more Rydberg levels. One requirement of these schemes is the ability to measure the Rydberg states' population in order to read out the results of the quantum operations. For accomplishing this task, most experiments with ultracold Rydberg gases use methods including field ionization and subsequent detection of electrons or ions on multichannel plates or channeltrons [3]. These techniques offer high sensitivity and —for carefully chosen experimental conditions [4,5]—selectivity among the Rydberg levels [6–8].

Selective field ionization (SFI) techniques are based on the fact that the ionization threshold is different for each atomic state, increasing from higher to lower lying levels. Hence, by slowly ramping up the electric field and monitoring the electrons or ions over time it is possible to deduce the initial populations in each level. However, the population of a lower lying Rydberg level cannot be probed without destroying the population of any higher lying Rydberg state. Therefore this method is not applicable in protocols which require independent probing of multiple Rydberg states [9]. Another inherent property of methods based on ionization is that the detected atoms are removed from the system and cannot be reused. Although this atomic loss is negligible in most cases [3], it might be a serious limitation in experiments working with only one or a few atoms [10].

One alternative to ionization detection methods is all-optical probing based on electromagnetically induced transparency (EIT) [11]. This approach has been successfully applied in order to nondestructively probe the Rydberg level structure in noninteracting [12,13] and weakly interacting [14] Rydberg gases, as well as in the presence of electric fields [15–19]. These experiments, however, did not access the population of the Rydberg state. On the other hand, an EIT-based scheme for the optical detection of the Rydberg population [20,21] has been proposed and demonstrated in dense atomic clouds where the Rydberg blockade allows the spatially resolved detection of Rydberg atoms.

Here we propose an all-optical scheme for detecting the population in a selected Rydberg state in dilute gases. By using a series of laser pulses in EIT configuration this technique also allows for distinction between coherent superpositions and statistical mixtures of the ground and Rydberg states of the atoms. Since this scheme is based on time-resolved observation of the optical response of individual atoms it may, in principle, be used down to the single atom level. Our method is state selective and applicable for testing the population not only in the highest Rydberg level of interest (cf. SFI) but any lower lying or intermediate Rydberg state.

We present our theoretical model along with numerical simulations and demonstrate the scheme in a proof-of-principle experiment with a dilute gas of ^{87}Rb atoms showing the detection of the population in an initially prepared Rydberg state. Our analysis includes characteristic effects of Rydberg experiments such as blackbody-induced depopulation [22,23], superradiance [24], and dipole-dipole interaction [25].

II. THEORETICAL MODEL

Let us consider a cold atomic gas interacting with two laser pulses in an EIT-like configuration [11]. One of the pulses, resonant with the atomic transition between the ground state $|1\rangle$ and the first excited state $|2\rangle$, is a weak probe pulse well below the saturation intensity, while the other one is a relatively strong coupling pulse which is resonant with the atomic transition between the first excited state $|2\rangle$ and a selected (arbitrary) Rydberg $nS_{1/2}$ state $|3\rangle$ (see Fig. 1). A

*florian.karlewski@uni-tuebingen.de

†Present address: IPCMS (UMR 7504) and ISIS (UMR 7006), Université de Strasbourg and CNRS, Strasbourg, France.

‡fortagh@uni-tuebingen.de

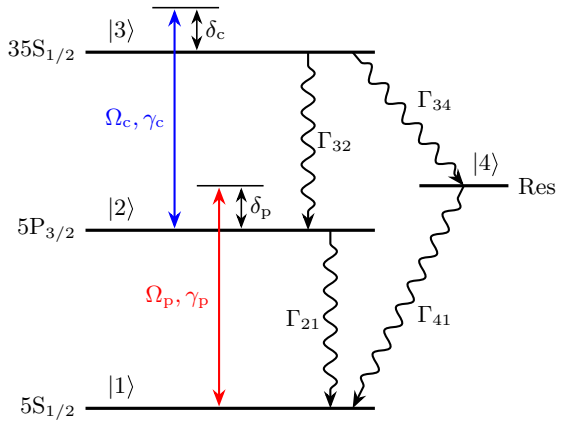

FIG. 1. (Color online) Illustration of the atom-laser interaction as used for the model of time-resolved EIT. States $|1\rangle$, $|2\rangle$, and $|3\rangle$ denote the ground state, the first excited state, and a Rydberg state of the atom, respectively. In our experimental setup, these states correspond to the $5S_{1/2}(F=2)$, $5P_{3/2}(F=3)$, and $35S_{1/2}(F=2)$ states of ^{87}Rb. The atomic transition $|1\rangle \leftrightarrow |2\rangle$ is driven by a weak probe laser with the Rabi frequency Ω_p (red), while the transition $|2\rangle \leftrightarrow |3\rangle$ is driven by a stronger coupling laser with the Rabi frequency Ω_c (blue). γ_p and γ_c denote coherence decay terms. δ_p and δ_c are the detunings of each laser to the corresponding atomic resonance. The radiative decay from the selected Rydberg state $|3\rangle$ to the neighboring states is accounted for by including a reservoir state $|4\rangle$. Γ_{ij} denote the respective incoherent decays, consisting of spontaneous emission as well as transitions induced by blackbody radiation.

single "reservoir" state $|4\rangle$ is used to model the neighboring Rydberg states [14].

We use a semiclassical approach for describing the dynamics of the system and the laser pulses are taken into account through their classical electric field. The atomic gas is modeled by a motionless ensemble of atoms. The state of the atoms is described by the density matrix $\rho = \sum_{i,j=1}^{4} \rho_{i,j} |i\rangle \langle j|$, where the states $|2\rangle$ and $|3\rangle$ rotate with the atomic transition frequencies ω_{21} and ω_{23}, respectively.

The time evolution of $\rho(t)$ is described by the master equation

$$i\hbar\dot{\rho} = [\mathcal{H}, \rho] + \mathcal{U}[\rho]. \tag{1}$$

Here the Hamiltonian $\mathcal{H}$ accounts for the interactions between the atoms and the laser pulses. The effects due to interatomic interactions are considered through dynamic effective rates in $\mathcal{U}[\rho]$ along with radiative losses occurring in the system. The Hamiltonian $\mathcal{H}$ is written as

$$\begin{aligned}\mathcal{H} = &-\frac{\hbar}{2}(\Omega_p |2\rangle \langle 1| + \Omega_c |3\rangle \langle 2| + \text{H.c.}) \\ &- \hbar(\delta_p |2\rangle \langle 2| + \delta_c |3\rangle \langle 3|),\end{aligned} \tag{2}$$

where $\Omega_p = (E_p d_{12})/\hbar$ and $\Omega_c = (E_c d_{23})/\hbar$ are the Rabi frequencies of the probe and coupling lasers, with E_p and E_c being the electric fields, and d_{12} and d_{23} the dipole matrix elements of the corresponding transitions, whereas δ_p and δ_c are the detunings of the probe and coupling laser from the corresponding transitions, respectively (see Fig. 1). Although we consider a situation where both the coupling and the probe laser are resonant with the atomic transitions they drive (i.e., $\delta_p = \delta_c = 0$), by including these detunings one can account for potentially uncompensated electric and/or magnetic fields in a specific experimental realization. The operator $\mathcal{U}$ which governs the non-Hamiltonian part of the dynamics reads as

$$\begin{aligned}\mathcal{U}[\rho] = &\frac{\Gamma_{32}}{2}(2\sigma_{13}\rho\sigma_{31} - \sigma_{33}\rho - \rho\sigma_{33}) \\ &+ \frac{\Gamma_{21}}{2}(2\sigma_{12}\rho\sigma_{21} - \sigma_{22}\rho - \rho\sigma_{22}) \\ &+ \frac{\Gamma_{34}}{2}(2\sigma_{43}\rho\sigma_{34} - \sigma_{33}\rho - \rho\sigma_{33}) \\ &+ \frac{\Gamma_{41}}{2}(2\sigma_{14}\rho\sigma_{41} - \sigma_{44}\rho - \rho\sigma_{44}) \\ &+ \frac{\gamma_p}{2}(2\sigma_{11}\rho\sigma_{11} - \rho_{11}\sigma - \rho\sigma_{11}) \\ &+ \frac{\gamma_c}{2}(2\sigma_{33}\rho\sigma_{33} - \rho_{33}\sigma - \rho\sigma_{33}),\end{aligned} \tag{3}$$

where $\sigma_{kj} = |k\rangle \langle j|$ are the atomic projection operators ($k, j \in \{1,2,3,4\}$).

There are multiple sources of nonunitary dynamics in the system. One of them is the spontaneous emission from the first excited state $|2\rangle$ and the Rydberg state $|3\rangle$ which we take into account by introducing radiative decay rates Γ_{21} and Γ_{32}. Another source, if present, is a depopulation of the Rydberg state $|3\rangle$ towards the neighboring Rydberg states. The depopulation may occur due to several phenomena depending on the actual realization of the system, such as amplified spontaneous emission and/or superradiance [24,26] as well as induced emission and absorption due to the blackbody radiation of the environment [22,23]. Following [26], we take these effects into account by modifying the third term in Eq. (3) to the dynamic effective decay rate

$$\tilde{\Gamma}_{34}(t) = \Gamma_{34,\text{sp}}[\rho_{44}(t) p_{\text{sup}} + 1] + \Gamma_{34,\text{bb}}, \tag{4}$$

with p_{sup} a superradiance parameter, and $\Gamma_{34,\text{sp}}$ and $\Gamma_{34,\text{bb}}$ the effective decay rates caused by spontaneous emission and blackbody radiation, respectively. In our model we assume that the entire population eventually ends up in the ground state $|1\rangle$. This assumption is valid provided the ionization from all involved states is negligible.

The above-mentioned phenomena cause population transfer between the atomic states. In contrast, there is a group of processes which do not result in a significant energy decay in the system but leads to a relevant coherence loss. One such process is the phase noise of the driving lasers, which is included into the model through the coherence decay rates γ_p and γ_c. Due to the redistribution of population from $|3\rangle$ to $|4\rangle$, atoms in Rydberg nP_j states are present in the cloud at various distances. As observed by [25], the dipole-dipole interaction with these nP_j state atoms results in an inhomogeneous broadening of the Rydberg $nS_{1/2}$ state. We take this into account by adding an effective dephasing term in Eq. (3) to γ_c,

$$\tilde{\gamma}_c(t) = \gamma_c + \gamma_{3,\text{dd}}\rho_{44}(t). \tag{5}$$

The optical response of the cloud under the effect of the two laser pulses is given by the macroscopic polarization $\vec{P} = \mathcal{N}\,\text{Tr}[\rho\vec{d}]$ where $\vec{d} = \sum_{i\neq j}(d_{ij} |i\rangle \langle j| + \text{H.c.})$ is the atomic dipole operator. The absorption α of the probe laser is then

given by the imaginary part of the electric susceptibility χ,

$$\alpha(t) = \mathrm{Im}[\chi(t)] = \frac{\mathcal{N} d_{12}^2}{\epsilon_0 \hbar \Omega_\mathrm{p}} \mathrm{Im}[\rho_{21}(t)], \tag{6}$$

where $\mathcal{N}$ is the atom density of the cloud. Note that here we make the approximation that the cloud is homogeneously irradiated and the propagation effects of the laser pulses can be neglected. The time-dependent absorption signal is thus given by the master equation, which, using the operators given in Eqs. (2) and (3), reads as

$$\dot{\rho}_{11} = \frac{i}{2}(\Omega_\mathrm{p}^* \rho_{21} - \Omega_\mathrm{p} \rho_{12}) + \Gamma_{21} \rho_{22} + \Gamma_{41} \rho_{44}, \tag{7a}$$

$$\dot{\rho}_{22} = \frac{i}{2}(\Omega_\mathrm{p} \rho_{12} - \Omega_\mathrm{p}^* \rho_{21} - \Omega_\mathrm{c} \rho_{23} + \Omega_\mathrm{c}^* \rho_{32}) - \Gamma_{21} \rho_{22} + \Gamma_{32} \rho_{33}, \tag{7b}$$

$$\dot{\rho}_{33} = \frac{i}{2}(\Omega_\mathrm{c} \rho_{23} - \Omega_\mathrm{c}^* \rho_{32}) - (\Gamma_{32} + \tilde{\Gamma}_{34}) \rho_{33}, \tag{7c}$$

$$\dot{\rho}_{21} = \frac{i}{2}[\Omega_\mathrm{c}^* \rho_{31} - \Omega_\mathrm{p} (\rho_{22} - \rho_{11}) + 2\delta_\mathrm{p} \rho_{21}] - \frac{1}{2}(\Gamma_{21} + \gamma_\mathrm{p}) \rho_{21}, \tag{7d}$$

$$\dot{\rho}_{31} = \frac{i}{2}[\Omega_\mathrm{c} \rho_{21} - \Omega_\mathrm{p} \rho_{32} + 2(\delta_\mathrm{p} + \delta_\mathrm{c}) \rho_{31}] - \frac{1}{2}(\gamma_\mathrm{p} + \tilde{\gamma}_\mathrm{c} + \Gamma_{32} + \tilde{\Gamma}_{34}) \rho_{31}, \tag{7e}$$

$$\dot{\rho}_{32} = \frac{i}{2}[-\Omega_\mathrm{p}^* \rho_{31} - \Omega_\mathrm{c} (\rho_{33} - \rho_{22}) - 2\delta_\mathrm{c} \rho_{32}] - \frac{1}{2}(\tilde{\gamma}_\mathrm{c} + \Gamma_{21} + \Gamma_{32}) \rho_{32}, \tag{7f}$$

$$\dot{\rho}_{44} = \tilde{\Gamma}_{34} \rho_{33} - \Gamma_{41} \rho_{44}, \tag{7g}$$

$$\dot{\rho}_{41} = \frac{i}{2}(-\Omega_\mathrm{p} \rho_{42} + 2\delta_\mathrm{p} \rho_{41}) - \frac{1}{2}(\Gamma_{41} + \gamma_\mathrm{p}) \rho_{41}, \tag{7h}$$

$$\dot{\rho}_{42} = -\frac{i}{2}(\Omega_\mathrm{p}^* \rho_{41} + \Omega_\mathrm{c} \rho_{43}) - \frac{1}{2}(\Gamma_{21} + \Gamma_{41}) \rho_{42}, \tag{7i}$$

$$\dot{\rho}_{43} = \frac{i}{2}(\Omega_\mathrm{c}^* \rho_{42} + 2\delta_\mathrm{c} \rho_{43}) - \frac{1}{2}(\Gamma_{32} + \tilde{\Gamma}_{34} + \Gamma_{41} + \tilde{\gamma}_\mathrm{c}). \tag{7j}$$

When there is no coupling to the Rydberg state ($\Omega_\mathrm{c} = 0$), an analytical steady state solution for α can be obtained, which will be used for normalization:

$$\alpha_0 = \frac{\mathcal{N} d_{12}^2}{\epsilon_0 \hbar} \Gamma_{21} (\gamma_\mathrm{p} + \Gamma_{21}) \times \left[\gamma_\mathrm{p}^2 \Gamma_{21} + 2\gamma_\mathrm{p} \left(\Omega_\mathrm{p}^2 + \Gamma_{21}^2\right) + \Gamma_{21} \left(4\delta_\mathrm{p}^2 + 2\Omega_\mathrm{p}^2 + \Gamma_{21}^2\right)\right]^{-1}. \tag{8}$$

III. DETECTION OF THE RYDBERG POPULATION: RESULTS OF THE NUMERICAL SIMULATION

We numerically solve the equation system (7) with the pulse sequence of the lasers given by $\Omega_\mathrm{p}(t)$ and $\Omega_\mathrm{c}(t)$ (see the sequence A, B, C in Fig. 2). The solution provides a description of the population dynamics while the atom is being probed by the weak laser on the $|1\rangle \leftrightarrow |2\rangle$ transition along with a time-dependent coupling between states $|2\rangle$ and $|3\rangle$. Furthermore, through Eq. (6) it describes the absorption of the probe laser, which we give relative to α_0 [see Eq. (8)]:

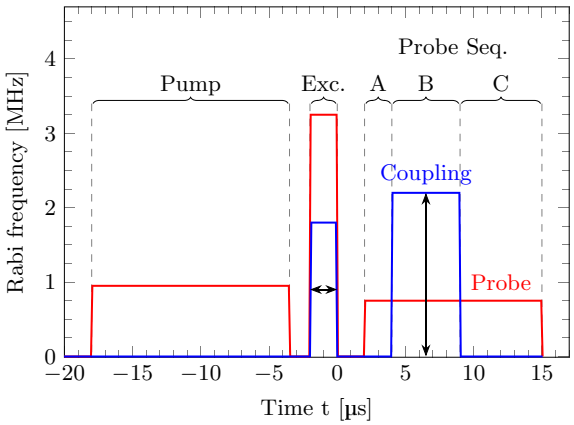

FIG. 2. (Color online) Pulse sequence for the coupling (blue) and probe (red) lasers. At $t = 0$ a fraction of the atomic population is prepared in the Rydberg state. In the simulations this fraction is an input value, while in the experiment it is determined by the length of the excitation pulse (Exc.). Before this, an optical pumping pulse (Pump) is used to pump the atoms to the correct polarization. The time evolution of the optical density is monitored after the excitation pulse with the probe laser (A, B, C). The coupling laser is added in time interval B (EIT pulse). The Rabi frequencies are taken from the experimental values in Sec. IV.

$$\alpha_\mathrm{rel}(t) = \frac{\alpha(t)}{\alpha_0}. \tag{9}$$

In Fig. 3 we show results for the cases where the entire population is initially (a) in the ground state [$\rho_0 \equiv \rho(t = 0) = |1\rangle\langle 1|$] or (b) in the selected Rydberg state ($\rho_0 = |3\rangle\langle 3|$). In (c) the population is split between the Rydberg state and the reservoir state ($\rho_0 = 0.7\,|3\rangle\langle 3| + 0.3\,|4\rangle\langle 4|$).

Following the pulse sequence, the time evolution of the system can be separated into three major parts. When the atoms are initially prepared in the ground state, only small changes in the populations are visible [see Fig. 3(a)]. However, the reasons for these changes are not the same in the different parts of the time evolution. In part A, when the atoms are only irradiated by the relatively weak probe laser ($\Omega_\mathrm{p} \ll \Gamma_{21}$), a small fraction of the population is transferred to the first excited state $|2\rangle$ by the absorbed light. In part B, the population transfer to state $|2\rangle$ is prevented by the strong coupling laser applied on the transition between states $|2\rangle$ and $|3\rangle$ and the absorption is reduced, which is the well-known effect of EIT. The time scale for the transparency to build up is defined by the Rabi frequency Ω_c of the coupling laser. If the requirement $\Omega_\mathrm{p} \ll \Omega_\mathrm{c}$ is not fulfilled, the transparency is only partial. In this case, the two laser fields cause two-photon transitions to state $|3\rangle$, and the absorption of the probe pulse is nonzero. This absorption level (in the case of $\delta_\mathrm{p} = \delta_\mathrm{c} = 0$) depends on $\Omega_\mathrm{p}/\Omega_\mathrm{c}$ and the decoherences γ_p and γ_c. A consequence of this effect is that different initial populations of Rydberg states cause a different absorption level in the equilibrium of part B

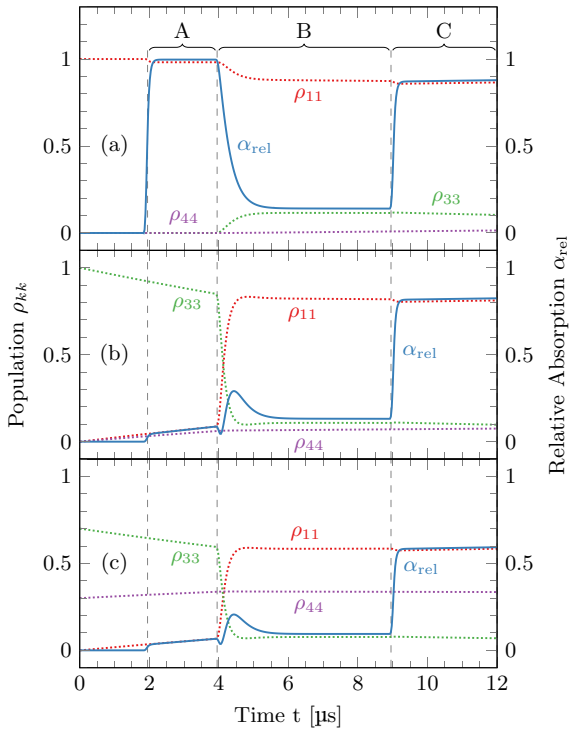

FIG. 3. (Color online) Dynamics of the populations $\rho_{kk}(t)$ of the atomic states (dotted lines) and the relative absorption $\alpha_{\rm rel}(t)$ (solid lines) of the probe laser induced by the pulse sequence A, B, C (see Fig. 2) for atoms initially prepared in the ground state (a), the selected Rydberg state (b), and the reservoir state (c). Since the population ρ_{22} is almost zero at all times, except for a transient population in the first 100 ns of B, it is not shown here.

due to the dependence of $\gamma_{\rm c}$ on ρ_{44}. In part C, where the atom cloud is again only irradiated by the weak probe laser, the process is very similar to what happens in part A with the exception that there is a small fraction of population in state $|3\rangle$. Consequently, the absorption level of the probe laser is smaller, because atoms are missing from the ground state.

In the case of initial population in the selected Rydberg state $|3\rangle$, the dynamics of the system only differ in parts A and B, provided B is long enough to reach steady state EIT. In part A, the absorption of the probe laser is close to zero, and slowly increases while a small fraction of the population decays from the Rydberg state $|3\rangle$. Since the lifetime of the Rydberg states is much longer than 10 μs, the amount of population transferred by spontaneous decay is small although not negligible on the microsecond time scale of the pulse sequence. At the beginning of part B the population in the selected Rydberg state is transferred to the ground state $|1\rangle$ through a resonant transfer from state $|3\rangle$ to $|2\rangle$ induced by the coupling laser with Rabi frequency $\Omega_{\rm c}$ and the consecutive spontaneous emission from $|2\rangle$ to $|1\rangle$. For $\Omega_{\rm c} < \Gamma_{21}$, this process results in only a small increase in ρ_{22}, because a half Rabi cycle induced by $\Omega_{\rm c}$ between states $|2\rangle$ and $|3\rangle$ would take longer than the lifetime of state $|2\rangle$ [see Fig. 3(b)]. Hence, assuming the initial population is either in the ground state $|1\rangle$ or the selected Rydberg state $|3\rangle$, we can determine the fractions by monitoring the absorption of the probe laser in part A of the time evolution. If there is a way to ensure that all the population missing from the ground state $|1\rangle$ is in the selected Rydberg state $|3\rangle$, then this is indeed sufficient. However, if the probability that a fraction of the population is in another state (for example, the interaction scheme to be realized contains more than one Rydberg state), the absorption level in part A of the time evolution is not enough in itself to give information about the population of the selected Rydberg state $|3\rangle$.

As illustrated in Figs. 3(b) and 3(c), the absorption of the probe laser in part A is the same for different initial states of the atoms as long as the population in the ground state is the same. In contrast, the dynamics and the equilibrium become significantly different in part B. Since only the population in the selected Rydberg state is transferred back to the ground state by the coupling field, the absorption level in part C also changes with the initial population in $|3\rangle$.

Another result of the simulations is the possibility to obtain information on the initial coherence of the system. The time evolution of the relative absorption in the beginning of part B for three different initial preparations of the atoms is shown in Fig. 4. These initial preparations consist of the same fraction of population in the ground state $|1\rangle$ and the selected Rydberg state $|3\rangle$, but the coherence between these two states is different. One of the initial preparations is the mixed state $\rho_{\rm m}(t=0) = \frac{1}{2}(|1\rangle\langle 1| + |3\rangle\langle 3|)$, while the other two preparations are $\rho_{\pm}(t=0) = \frac{1}{4}(|1\rangle \pm |3\rangle)(\langle 1| \pm \langle 3|)$. Comparing numerical calculations for these three cases, we find significant changes in the beginning of part B, where the EIT did not yet reach equilibrium. The absorption level during the rest of the pulse sequence is not sensitive to the initial coherence. If the Rabi frequency $\Omega_{\rm c}$ of the coupling laser is on the order of Γ_{23} or higher, oscillations of the absorption signal can be observed.

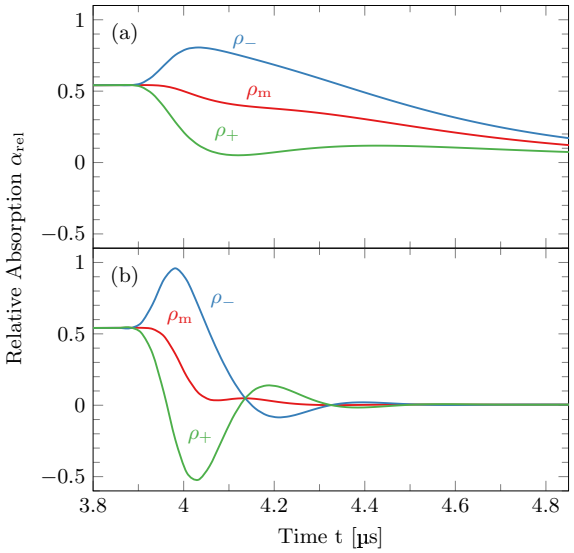

FIG. 4. (Color online) Numerically calculated relative absorption $\alpha_{\rm rel}$ of the probe laser in the beginning of part B for atoms prepared in states $\rho_{\rm m}(t=0) = \frac{1}{2}(|1\rangle\langle 1| + |3\rangle\langle 3|)$ and $\rho_{\pm}(t=0) = \frac{1}{4}(|1\rangle \pm |3\rangle)(\langle 1| \pm \langle 3|)$. The parameters used for the calculation are the same as for Fig. 3 with $\Omega_{\rm c} < \Gamma_{21}$ in (a) and $\Omega_{\rm c} \approx \Gamma_{21}$ in (b). This distinct signature of coherent states is expected to be experimentally observable and even more pronounced if $\Omega_{\rm c}$ is larger.

IV. EXPERIMENTAL SETUP

For demonstrating the detection of Rydberg population with time-resolved EIT, we have conducted an experiment on a cloud of $\approx 2 \times 10^7$ ^{87}Rb atoms at a temperature of ≈ 150 μK. In this experiment the atoms are trapped in a magneto-optical trap, loaded to a magnetic quadrupole trap and then released. The time-resolved measurements are started after 3 ms of time of flight, in order to ensure that all magnetic fields have fully decayed while the effects of atomic motion are still negligible. The measurements are performed within 30 μs (excitation pulse and probe sequence, cf. Fig. 2). The density and optical density at the center of the cloud, measured by absorption imaging, are 5×10^9 cm^{-3} and 1.7, respectively.

The transitions from the ground state $|5S_{1/2}, F = 2\rangle$ to the first excited state $|5P_{3/2}, F = 3\rangle$ and from there to the selected Rydberg state $|35S_{1/2}\rangle$ are driven by two lasers with wavelengths of $\approx$780 nm (red, probe) and $\approx$480 nm (blue, coupling), respectively (see Fig. 1). Additionally, we use a repumper to pump atoms from $|5S_{1/2}, F = 1\rangle$ back to $|5S_{1/2}, F = 2\rangle$ via $|5P_{3/2}, F = 2\rangle$ during the whole pulse sequence. The frequencies of both lasers used in the experiment are referenced to a frequency comb and controlled with slow servo loops (<100 Hz bandwidth). The linewidths of both lasers are narrowed to less than $2\pi \times 20$ kHz with fast locks (>1 MHz bandwidth) to scanning Fabry-Pérot interferometers. As the Fabry-Pérot cavities are sensitive to acoustic noise, the effective linewidth for the experiment can be larger. The red and the blue lasers are aligned in a counterpropagating configuration (see Fig. 5). We use an acousto-optic modulator (AOM) in each beam to create the intensity envelopes of the pulses. The switching time of the AOMs is 50 ns (20%–80% light intensity). The time-dependent intensity of the red laser (probe signal) is measured with an avalanche photodetector (Thorlabs APD120A/M) and recorded with a digital oscilloscope. The time resolution of the setup is 20 ns.

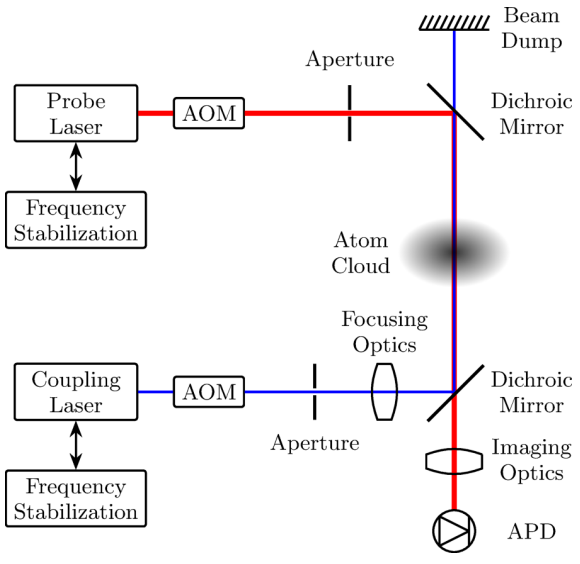

FIG. 5. (Color online) Experimental setup for time-resolved EIT measurements. The counterpropagating coupling (blue) and probe (red) beams are superimposed on the atom cloud and separated with dichroic mirrors. The transmission of the probe laser is detected by an avalanche photo diode (APD). The intensities of the lasers are controlled with acousto-optic modulators (AOM). Both laser frequencies are stabilized using a frequency comb.

As shown in Fig. 2, our measurement consists of three main parts. First we put all the atomic population into the Zeeman-sublevel of the ground state matching the polarization of the red laser by optically pumping for 14.5 μs. This pulse is also long enough that any transient effects due to the switching of the AOM wear off before the next pulse. Next, we prepare the initial state of the atomic cloud with an excitation pulse. We always apply the red laser for 2 μs with a Rabi frequency of $2\pi \times 3.3$ MHz. If we want no population to be transferred to the Rydberg state, the blue laser remains switched off and due to the very short lifetime of the first excited state, practically the entire population remains in the ground state. Applying the blue laser with a Rabi frequency of $2\pi \times 1.8$ MHz for up to 2 μs causes a fraction of the population to be transferred to the Rydberg state, with the most atoms being excited in the case of the full 2 μs pulse. Due to the high Rabi frequency of the red laser there is no coherent excitation of Rydberg atoms. In the third part (probe sequence in Fig. 2), we use the red laser at a low intensity as the probe laser during time intervals A, B, and C together with the blue laser as the coupling laser during time interval B (EIT pulse).

As a reference, we always add one experimental cycle without atoms in order to measure the intensity $I_{\mathrm{ref}}(t)$ of the red laser with the photodetector and another one with atoms but no excitation pulse and no coupling pulse to normalize the data later on. The parameters are then varied from cycle to cycle and the transmitted intensity $I_{\mathrm{T}}(t)$ of the probe light after passing through the cloud is measured. The experiment is repeated several times for each set of parameters to reduce photodiode noise. The optical density (OD) is calculated as follows:

$$\mathrm{OD}(t) = -\ln\left(\frac{I_{\mathrm{T}}(t)}{I_{\mathrm{ref}}(t)}\right). \tag{10}$$

The resulting OD datasets are then normalized by dividing them by the OD dataset that had no excitation pulse and no EIT pulse [$\mathrm{OD}_0(t)$]:

$$\mathrm{OD}_{\mathrm{rel}}(t) = \frac{\mathrm{OD}(t)}{\mathrm{OD}_0(t)} \hat{=} \frac{\alpha(t)}{\alpha_0}. \tag{11}$$

This relative optical density $\mathrm{OD}_{\mathrm{rel}}$ is comparable to the relative absorption $\alpha(t)/\alpha_0$ that is calculated in the numerical simulation. To reduce the effect of the acoustic noise on our Fabry-Pérot cavities, we selected the 30 datasets where the mean transparency in the EIT pulse between 7 and 9 μs was maximal. We observe that in all measurements the relative optical density eventually returns to the level before the excitation pulse, ensuring that ionization effects are negligible.

In general this scheme is applicable in situations where the optical density can be precisely measured. The resolution is limited by technical noise from the photodiode and the digital resolution of the subsequent data acquisition system. For low optical densities it is necessary to detect not only the absorption of the atoms, but to resolve the EIT signal as well. At high optical densities the constant resolution of the intensity measurement additionally leads to a lower

resolution of the optical density due to the logarithmic scaling in Eq. (10). For sufficient averaging, we estimate the presented scheme to be applicable in the range of optical densities between ≈0.1 and ≈4. In principal, the optical density can be lowered by detuning the probe laser while maintaining the two-photon resonance for the EIT condition, which on the other hand decreases the contrast for the EIT signal and therefore only allows for a limited extension of the range.

V. DETECTION OF THE INITIAL POPULATION: EXPERIMENTAL RESULTS

We demonstrate the optical detection of population for three different initial Rydberg excitation pulses. The experimental results for the optical density are shown in Fig. 6. In order to compare these results to the model we calculate values for the decay rates matching the chosen combination of states in our experiment (see Fig. 1). We calculate the spontaneous emission rates using the wave functions calculated in [19]. Γ_{32} is approximated by summing the spontaneous decay rates from $|35S_{1/2}\rangle$ to all nP_j states, which results in

$$\Gamma_{32} = \sum_{n>5} \Gamma_{\mathrm{sp},35S\to n\mathrm{P}} = 2\pi \times 3.9\ \mathrm{kHz}. \tag{12}$$

The main contribution comes from $|5P_{3/2}\rangle$ ($\Gamma_{\mathrm{sp},35S\to 5P} = 2\pi \times 1.2$ kHz) and other low-lying, fast-decaying states. The spontaneous decay rate $\Gamma_{34,\mathrm{sp}}$ is given by the rate $\Gamma_{\mathrm{sp},35S\to 34P} = 2\pi \times 16.8$ Hz. Here we take only the strongest superradiant transition into account. The transition rate $\Gamma_{34,\mathrm{bb}}$ is approximated by a sum over all transition rates induced by blackbody radiation from $|35S_{1/2}\rangle$ to all nP_j states

$$\Gamma_{34,\mathrm{bb}} = \sum_{n>5} \Gamma_{\mathrm{bb},35S\to nP} = 2\pi \times 2.7\ \mathrm{kHz}, \tag{13}$$

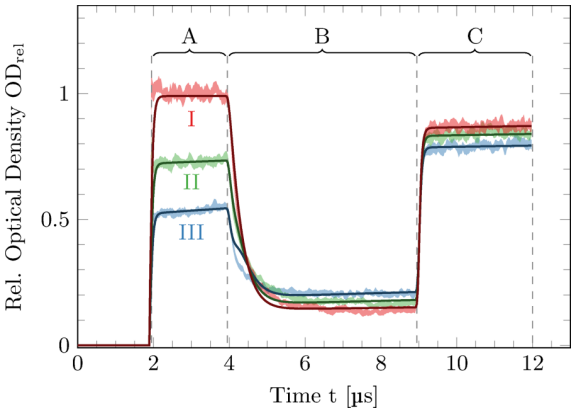

FIG. 6. (Color online) Measured optical density for the dynamics during the probe sequence. The shaded areas are 95% confidence intervals for the relative optical densities $\mathrm{OD}_{\mathrm{rel}}(t)$ obtained from the measurements by applying Eqs. (10) and (11) for three durations of the excitation pulse (0 μs for I, 0.5 μs for II, and 2 μs for III). Solid lines represent fit results for the simulated relative absorption $\alpha(t)/\alpha_0$. The reversed order of the absorption signals in part B can be explained by dipole-dipole interactions.

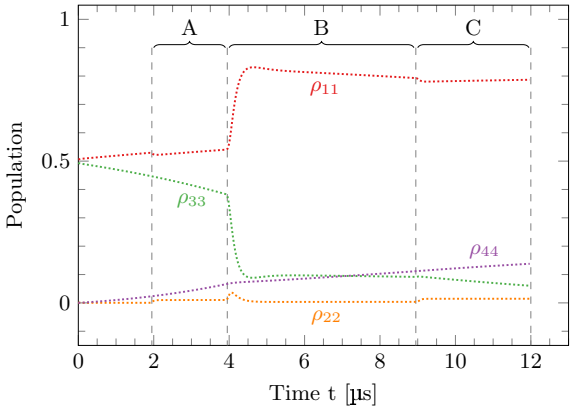

FIG. 7. (Color online) Dynamics of the population of the four states ($\rho_{11} \mathrel{\hat{=}} 5S_{1/2}$, $\rho_{22} \mathrel{\hat{=}} 5P_{3/2}$, $\rho_{33} \mathrel{\hat{=}} 35S_{1/2}$, $\rho_{44} \mathrel{\hat{=}}$ Reservoir) retrieved from the fit to the dataset with high excitation (see Fig. 6). The colors match those of the states in Fig. 3. The population of the Rydberg state ($35S_{1/2}$) starts to decay immediately after excitation at $t = 0$.

in which the rates $\Gamma_{\mathrm{bb},35S\to nP}$ are calculated as in [22,23]. The main contribution to $\Gamma_{34,\mathrm{bb}}$ comes from neighboring Rydberg states. For the transitions induced by blackbody radiation a temperature of 300 K is assumed. The preceding approximations for the decay rates ensure that the total decay out of the state $|35S_{1/2}\rangle$ is modeled correctly. Similar to the calculation of Γ_{32} we obtain

$$\Gamma_{41} = \sum_{n>5} \Gamma_{\mathrm{sp},34P\to nS} = 2\pi \times 0.8\ \mathrm{kHz}. \tag{14}$$

The Rabi frequencies of the two lasers $\Omega_{\mathrm{p}} = 2\pi \times 0.83$ MHz and $\Omega_{\mathrm{c}} = 2\pi \times 2.10$ MHz and the coherence decay $\gamma_{\mathrm{c}} = 2\pi \times 112$ kHz are fitted to the dataset without Rydberg excitation (see curve "I" in Fig. 6). The Rabi frequencies are consistent with estimates based on beam power and geometry. The noise γ_{c} is mainly caused by the acoustic noise on the Fabry-Pérot cavities. As the fit is only sensitive to $\gamma_{\mathrm{p}} + \gamma_{\mathrm{c}}$ and not to the single values, we choose $\gamma_{\mathrm{p}} = 2\pi \times 20$ kHz.

An analysis of the datasets with the same conditions, but with Rydberg excitation, allows us to fit the fraction of atoms excited to a Rydberg state [0.494(8) and 0.284(10)] within interval A, where only the red laser is on. The superradiance parameter $p_{\mathrm{sup}} = 7.9(8) \times 10^3$ is fitted to parts B and C and the dipole-dipole interaction parameter $\gamma_{3,\mathrm{dd}}$ is adjusted in part B. The former scales with the absolute atom number, while the latter scales with the atomic density. From the model one can now derive the time-resolved populations of the participating states as can be seen in Fig. 7. The accuracy of these populations is within ±0.01 compared with values calculated using a variation method.

VI. CONCLUSION

We have demonstrated the all-optical detection of Rydberg population in a dilute gas, which is an alternative to the methods based on field ionization. Our results show that Rydberg population fractions can be measured with an accuracy of 0.01. By comparing the dynamics of the measured optical densities to our numerical simulations we have quantified the

decoherence effects occurring in the system, namely, blackbody radiation induced transitions, superradiant decay, and inhomogeneous broadening due to dipole-dipole interactions.

From our simulations we conclude that the detection scheme can also be used to obtain information on the coherence between the ground state and the Rydberg state. The numerical results predict that future studies using a coherent excitation method and experimental parameters similar to our experiment will be able to detect the initial and time-dependent coherence.

ACKNOWLEDGMENTS

The authors thank Daniel Cano and Florian Jessen for the design and setup of the experimental chamber and Claus Zimmermann for valuable discussions. This work was financially supported by the FET-Open Xtrack Project HAIRS and the Carl Zeiss Stiftung. N.S. acknowledges financial support from the framework of TÁMOP-4.2.4.A/2-11/1-2012-0001 "National Excellence Program."

[1] M. Saffman, T. G. Walker, and K. Mølmer, Quantum information with Rydberg atoms, Rev. Mod. Phys. **82**, 2313 (2010).

[2] H. Weimer, M. Muller, I. Lesanovsky, P. Zoller, and H. P. Büchler, A Rydberg quantum simulator, Nat. Phys. **6**, 382 (2010).

[3] R. Löw, H. Weimer, J. Nipper, J. B. Balewski, B. Butscher, H. P. Büchler, and T. Pfau, An experimental and theoretical guide to strongly interacting Rydberg gases, J. Phys. B **45**, 113001 (2012).

[4] D. A. Tate, Comment on "measurement of the lifetimes of s and d states below $n = 31$ using cold Rydberg gas", Phys. Rev. A **75**, 066502 (2007).

[5] L. L. Caliri and L. G. Marcassa, Reply to "comment on 'measurement of the lifetimes of s and d states below $n = 31$ using cold Rydberg gas"', Phys. Rev. A **75**, 066503 (2007).

[6] A. L. de Oliveira, M. W. Mancini, V. S. Bagnato, and L. G. Marcassa, Measurement of Rydberg-state lifetimes using cold trapped atoms, Phys. Rev. A **65**, 031401 (2002).

[7] V. A. Nascimento, L. L. Caliri, A. L. de Oliveira, V. S. Bagnato, and L. G. Marcassa, Measurement of the lifetimes of s and d states below $n = 31$ using cold Rydberg gas, Phys. Rev. A **74**, 054501 (2006).

[8] D. B. Branden, T. Juhasz, T. Mahlokozera, C. Vesa, R. O. Wilson, M. Zheng, A. Kortyna, and D. A. Tate, Radiative lifetime measurements of rubidium Rydberg states, J. Phys. B **43**, 015002 (2010).

[9] D. Cano and J. Fortágh, Multiatom entanglement in cold Rydberg mixtures, Phys. Rev. A **89**, 043413 (2014).

[10] H. Labuhn, S. Ravets, D. Barredo, L. Béguin, F. Nogrette, T. Lahaye, and A. Browaeys, Single-atom addressing in microtraps for quantum-state engineering using Rydberg atoms, Phys. Rev. A **90**, 023415 (2014).

[11] M. Fleischhauer, A. Imamoglu, and J. P. Marangos, Electromagnetically induced transparency: Optics in coherent media, Rev. Mod. Phys. **77**, 633 (2005).

[12] A. K. Mohapatra, T. R. Jackson, and C. S. Adams, Coherent optical detection of highly excited Rydberg states using electromagnetically induced transparency, Phys. Rev. Lett. **98**, 113003 (2007).

[13] M. Mack, F. Karlewski, H. Hattermann, S. Höckh, F. Jessen, D. Cano, and J. Fortágh, Measurement of absolute transition frequencies of ^{87}Rb to nS and nD Rydberg states by means of electromagnetically induced transparency, Phys. Rev. A **83**, 052515 (2011).

[14] K. J. Weatherill, J. D. Pritchard, R. P. Abel, M. G. Bason, A. K. Mohapatra, and C. S. Adams, Electromagnetically induced transparency of an interacting cold Rydberg ensemble, J. Phys. B **41**, 201002 (2008).

[15] A. Tauschinsky, R. M. T. Thijssen, S. Whitlock, H. B. van Linden van den Heuvell, and R. J. C. Spreeuw, Spatially resolved excitation of Rydberg atoms and surface effects on an atom chip, Phys. Rev. A **81**, 063411 (2010).

[16] M. G. Bason, M. Tanasittikosol, A. Sargsyan, A. K. Mohapatra, D. Sarkisyan, R. M. Potvliege, and C. S. Adams, Enhanced electric field sensitivity of rf-dressed Rydberg dark states, New J. Phys. **12**, 065015 (2010).

[17] H. Hattermann, M. Mack, F. Karlewski, F. Jessen, D. Cano, and J. Fortágh, Detrimental adsorbate fields in experiments with cold Rydberg gases near surfaces, Phys. Rev. A **86**, 022511 (2012).

[18] A. Tauschinsky, R. Newell, H. B. van Linden van den Heuvell, and R. J. C. Spreeuw, Measurement of ^{87}Rb Rydberg-state hyperfine splitting in a room-temperature vapor cell, Phys. Rev. A **87**, 042522 (2013).

[19] J. Grimmel, M. Mack, F. Karlewski, F. Jessen, M. Reinschmidt, N. Sándor, and J. Fortágh, Measurement and numerical calculation of rubidium Rydberg stark spectra [New J. Phys. (to be published)], arXiv:1503.08953.

[20] G. Günter, M. Robert-de-Saint-Vincent, H. Schempp, C. S. Hofmann, S. Whitlock, and M. Weidemüller, Interaction enhanced imaging of individual Rydberg atoms in dense gases, Phys. Rev. Lett. **108**, 013002 (2012).

[21] G. Günter, H. Schempp, M. Robert-de-Saint-Vincent, V. Gavryusev, S. Helmrich, C. S. Hofmann, S. Whitlock, and M. Weidemüller, Observing the dynamics of dipole-mediated energy transport by interactionenhanced imaging, Science **342**, 954 (2013).

[22] I. I. Beterov, I. I. Ryabtsev, D. B. Tretyakov, and V. M. Entin, Quasiclassical calculations of blackbodyradiation-induced depopulation rates and effective lifetimes of Rydberg ns, np, and nd alkali-metal atoms with $n \leqslant 80$, Phys. Rev. A **79**, 052504 (2009).

[23] I. I. Beterov, I. I. Ryabtsev, D. B. Tretyakov, and V. M. Entin, Erratum: Quasiclassical calculations of blackbody-radiation-induced depopulation rates and effective lifetimes of Rydberg ns, np, and nd alkali-metal atoms with $n \leqslant 80$ [Phys. Rev. A **79**, 052504 (2009)], Phys. Rev. A **80**, 059902(E) (2009).

[24] T. Wang, S. F. Yelin, R. Côté, E. E. Eyler, S. M. Farooqi, P. L. Gould, M. Koštrun, D. Tong, and D. Vrinceanu, Superradiance in ultracold Rydberg gases, Phys. Rev. A **75**, 033802 (2007).

[25] W. R. Anderson, M. P. Robinson, J. D. D. Martin, and T. F. Gallagher, Dephasing of resonant energy transfer in a cold Rydberg gas, Phys. Rev. A **65**, 063404 (2002).

[26] J. O. Day, E. Brekke, and T. G. Walker, Dynamics of low-density ultracold Rydberg gases, Phys. Rev. A **77**, 052712 (2008).